Forest Attributes from Multi-Angle Multi-Date Remotely Sensed Data

by

Andrew Dyk
B.E.S., University of Waterloo, 1989

A Thesis Submitted in Partial Fulfillment
of the Requirements for the Degree of

MASTERS OF SCIENCE

in the Department of Geography

Supervisory Committee

Forest Attributes from Multi-Angle Multi-Date Remotely Sensed Data

by

Andrew Dyk
B.E.S., University of Waterloo, 1989

Supervisory Committee

Dr. K. Olaf Niemann (Department of Geography)
Supervisor

Dr. Mark S. Flaherty (Department of Geography)
Departmental Member

Dr. David G. Goodenough (Department of Computer Science)
Outside Member

Supervisory Committee
Dr. K. Olaf Niemann (Department of Geography)
Supervisor
Dr. Mark S. Flaherty (Department of Geography)
Departmental Member
Dr. David G. Goodenough (Department of Computer Science)
Outside Member

Abstract

Multi-Angle, Multi-Date, Hyperspectral imagery of forests have been used to provide accurate estimates of the canopy characteristics. This thesis investigated the influence of various forest attributes on the spectral reflectance over time and view direction. The Compact High Resolution Imaging Spectrometer (CHRIS) is aboard the ESA PROBA satellite. The revisits of the CHRIS multi-angle images have been used to improve the accuracies of forest species recognition and stand densities compared to a nadir view only. Multi-angle data for CHRIS analysis of forest species produced higher accuracy and were easier to obtain than multi-date date. 5-Scale, a radiative transfer model, and CHRIS data have been compared as inputs into Partial Least Squares (PLS), a full-spectrum analytical method that offers relations between forest stand parameters and the resulting spectra. The resulting coefficients highlight where (view angle and spectral regions) within the multi-angle spectra contributed to estimating the various forest parameters. Methodology of collecting spectral calibration data in the field and the unique pre-processing challenges have been described.

Table of Contents

List of Tables

List of Figures

List of Acronyms

ADEOS – Advanced Earth Observing Satellite

ASCII – American Standard Code for Information Interchange

ASD – Analytical Spectrum Device

ATCOR – Atmospheric/Topographic CORrection

UVICS – The British Columbia Centre for Applied Remote Sensing Modelling and Simulation

BEAM – Brockman Consultant's Earth Observation Toolbox and Development Platform

BNSC – British National Space Centre

CCF – Canopy Closure Fraction

CFS – Canadian Forest Service

CHRIS – Compact High Resolution Imaging Spectrometer

CRD – Capital Regional District (Victoria BC)

DART – Discrete Anisotropic Radiative Transfer

DEM - Digital Elevation Model

DN – Digital Numbers

ENVI – Software Product of ITT Visual Information Solutions

ESA – European Space Agency

EVC – Evaluation and Validation of CHRIS for National Forests Project

EVEOSD – Evaluation and Validation of Earth Observation for Sustainable Development of forests.

FLAASH – Fast Line-of-sight Atmospheric Analysis of Spectral Hypercubes

fPAR – Fraction of Photosynthetically Active Radiation

FWHM – Full Width Half Maximum

FZA – Fly-by Zenith Angle

GCP – Ground Control Points

GMT – Greenwich Mean Time

GORT – Geometric Optical-Radiative Transfer

GPS – Global Positioning System

GSD – Ground Sampling Distance

GVWD – Greater Victoria Watershed District

HDF – Hierarchical Data Format

IFOV – Instantaneous Field of View

KML – Keyhole Mark-up Language

LAI – Leaf Area Index

LIBERTY – Leaf Incorporating Biochemistry Exhibiting Reflectance and Transmittance Yields

LIDAR – LIght Detection And Ranging

MLR – Multiple Linear Regression

MNF – Minimum Noise Fraction

MODTRAN4 – MODerate resolution atmospheric TRANsmission

MZA – Minimum Zenith Angle

NASA –National Aeronautics and Space Administration

OAA – Orbital Azimuth Angle

OZA – Orbital Zenith Angle

PCI – Software Company based in Richmond Hill, ON, Canada

PLS – Partial Least Squares

POLDER – POLarization and Directionality of the Earth's Reflectances

PROBA – Project for On-Board Autonomy

PROSPECT – A Model of Leaf Optical Properties Spectra

RAMI – RAdiation transfer Model Intercomparison

RFM – Rational Function Model

RMS – Root Mean Square

RSSI –Relative Structural Scattering Index

RTM – Radiative Transfer Model

SD – Stem Density

SPRINT – Spreading of Photons for Radiation INTerception

SSI – Structural Scattering Index

SSMA – Sub-Satellite position at Maximum Approach

SR – Spectral Adjustment Ratio

TLE – Two-Line orbital Elements

TRIM – Terrain Resource Inventory Mapping

U of T – University of Toronto

UVic – University of Victoria

VNIR – Visible Near Infra-Red

Acknowledgments

The author would like to thank ESA for the data that has been provided using the ESA PROBA platform and the SIRA Technology Ltd. CHRIS instrument, developed with support from BNSC. Thank you to Dr. David Goodenough for supporting and providing me this opportunity; through you I have learned so much. Jeff Dechka also provided support while I tackled a new position and continued to research this thesis. I also thank Dr. Olaf Niemann for his guidance and support while working on this thesis. Randy Enkins of the Geological Survey of Canada has been most valuable in solving spherical geometry equations. I thank Joel Ussery of the Capital Regional District Water Department for supplying forest cover and digital aerial photography of the Greater Victoria Watershed District. Thanks to Dale and Teresa Erb for allowing scientists to walk on their "grassy field" to make spectral measurements during satellite overpasses. Repeated access to their property has provided invaluable ground calibration data. Olaf Neiman and his team including Fabio and Rafael thank you for gathering field data related to the forest plots used in this study and UVIC for the loan of the ASD. Thank you goes to Anita Simic for her ideas on CHRIS processing and insight into multi-angle imagery and Jing Chen of the University of Toronto for processing the LAI data and offering his program 5-Scale. Thank you to the team at DIELMO 3D (Garcia and J.Moreno) for developing and applying noise correction to our CHRIS data long before anyone else could do it. The development and implementation of the automated PLS process in the AFT lab at the CFS is credited to Dr. David Goodenough's team, Sarah MacDonald, Tian Han, Geordie Hobart and Ash Richardson. Without this process, the exploration of PLS would not have been possible in this thesis. Most of all, thank you to

my wife Joanne and my daughters Kassidy and Tianna, for putting up with me during my years of distraction and letting me place second priority on way too many things.

Dedication

I'd like to dedicate this work to my parents, Dick and Ekka Dyk who believed in me and allowed me to pursue my goal of education. Both my parents lost their battle with cancer during my process of doing my thesis.

Chapter 1. Forest Attributes from Multi-Date Spectrodirectional Hyperspectral Remotely Sensed Data

1.1. Introduction

1.1.1. Importance of Forestry in Canada

Canada has an important and diverse forested area. With 10% of the global forest (4.02 million km²) it is home to over two thirds of Canada's 140,000 species of plants, animals and micro-organisms. The economic importance of forestry in Canada is shown in the annual sales of $80 billion of forest products; from 300 forest dependent communities, where more than 339,900 individuals find employment in the forest industry (CFS 2006).

Hyperspectral imagery of forest contributes to providing information related to better and more accurate inventory, as well as new measurements of forest biomass. All of these can contribute to Canada's reporting commitments on the Kyoto Protocol (Government of Canada 2005). Forest biomass information is important for many aspects of forest management, including quantifying forest yield, growth and productivity, and assessing changes in forest structure. Since the adoption of the Kyoto Protocol by many countries, reliable biomass estimation becomes even more important for its direct relationship with above-ground carbon.

Remote-sensing technologies are commonly used for mapping physical and structural features of forests (Treitz and Howarth 1999; Wulder 1998). Methods are needed to improve and automate these estimates. Nadir looking airborne and satellite hyperspectral sensing have provided accurate maps of forest species (Goodenough 2003; Martin et al. 1998), foliar chemistry (Curran 1989; Gastellu-Etchegorry and Bruniquel-Pinel 2001; Coops et al. 2003; Goodenough 2003; Smith et al. 2003), leaf area index (Schlerf et al.

2004) and above ground biomass (Goodenough et al. 2005a; Skole and Qi 2001). Multi-angle imagery has added another dimension of observation upon which forest canopies can be observed, and therefore produce images with increased information content (Barnsley et al. 1997; Asner et al. 1998). The use of multi-angle imagery has been shown to improve estimation of species recognition (Goodenough et al. 2005b; Kayitakire and Defourny 2004) and LAI retrieval over single angle measurements using model inversions (Diner et al. 1999). LAI and clumping index have been estimated using multi-angle imagery (Chen et al. 2003). By combining hyperspectral and multi-angle measurements, also known as spectrodirectional, it may be possible to further improve the estimation of forest attributes.

Forest information products such as species recognition and biomass can be estimated from multi-angle hyperspectral imagery. In order to perform this analysis reliable species and biomass base maps are needed for training purposes. These base maps can be generated from a combination of LIDAR, hyperspectral and field data. LIDAR data has been used to estimate biomass (Lim and Treitz 2004; Naesset 2004) and can provide estimates of forest parameters (Riaño et al. 2003). These forest parameters can then be used as inputs into yield prediction models (Johnson 2005) or allometric equations to calculate above-ground forest biomass.

1.2. Research Objectives

The intention of this thesis is to investigate the influence of forest attributes on the spectral reflectance when acquired over various view directions and time. Multi-angle, multi-date hyperspectral imagery has been used to investigate the influence of forest stand spectral and structural properties on spectral reflectance. The research question

addressed in this study is: What influence do forest species and structural parameters have on the reflected spectrum of sunlight as measured by multi-angle and multi-date hyperspectral imagery?

The following objectives have been established in response to the research question:

- Compare forest species classification results using various angles and dates of hyperspectral data to determine optimum image combinations (see Chapter 2);
- Establish a field calibration methodology to provide suitable ground target reflectance for various multi-angle hyperspectral imagery (see Chapter 3);
- Establish a method pre-processing multi-angle and multi-date hyperspectral data in order to perform spectral analysis (see Chapter 4);
- Create a means to estimate ground calibration plots measuring a range of forest parameters suitable for analysis (see Chapter 5).
- Perform a spectral analysis to determine where spectrally areas of reflectance vary when estimating forest parameters (see Chapter 5).

1.3. Study Area

Greater Victoria Watershed District (GVWD) is located on Southern Vancouver Island (Figure 1). Forest canopy consists predominately of Coastal Douglas-fir (*Pseudotsuga menziesii*), Western Redcedar (*Thuja plicata*) and Western Hemlock (*Tsuga heterophylla*). The understory cover is dominated by salal (*Gaultheria shallon*) (Niemann 1995). The GVWD has experienced a variety of logging activities in the last 100 years, but now it is a protected watershed for drinking water supply.

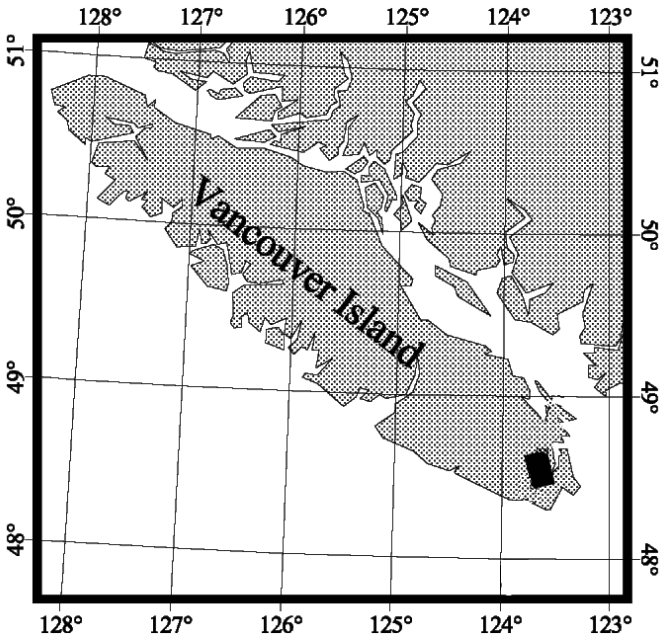

Figure 1. Location of the GVWD study area on Vancouver Island.

The GVWD watershed area has been the focus site of research for costal forestry for many years. Studies included research on thinning and fertilization affects on growth of Douglas-fir (Brix 1993; Beddows 2002; Getzin et al. 2006), LIDAR (Niemann et al. 2005), radar (Bhogal et al. 1998) and hyperspectral (Goodenough et al. 1995; Martin et al. 1998; Goodenough 2003).

1.4. Remote Sensing Methods

One must consider the concepts of bidirectional reflectance distribution function (BRDF), spectrodirectional remote sensing, radiative transfer models and Partial Least Squares (PLS) in order to understand the process of extracting forest biophysical and biochemical properties. The following sections gives an overview of these concepts related to the methodological approach used in this study.

1.5. Bidirectional Reflectance Distribution Function (BRDF)

Solar radiation reflected from the Earth's surfaces, and measured by satellites, has depended strongly on the angles of the sun and the satellite in relation to the surface. This bidirectional behaviour is quantified using the Bidirectional Reflectance Distribution Function (BRDF). Objects on the earth's surface reflect light in an anisotropic way, meaning the amount of reflected light varies with the viewing angle. Anisotropic behaviour is considered a noise for some to get rid of, and to others it can be considered a valuable source of information on vegetation structure (Kayitakire and Defourny 2004). For example, wide field of view sensors acquire imagery of the same ground from two view points, where the reflectance of this overlapping area will vary due to its anisotropic nature. A BRDF correction for NOAA AVHRR data has been developed to normalize the imagery to appear as if it was acquired directly overhead (Chen and Cihlar 1997). Corrected AVHRR data can then be used to create seamless weekly composites.

Forest canopy structural information can be derived from images by measuring the anisotropic properties of multi-angle imagery, namely the BRDF (Settle 2004). Gerstl (1996) considers BRDF to be a generalized form of the 'angular signature'. The angular signature of a single pixel depends on the anisotropic scattering properties of the material in that pixel and their 3D arrangement (Nolin 2004). The angular effects can be separated

into two components, one that is a function of wavelength, and the other a function of viewing angle (Settle 2004).

The angular signature varies with the spectral wavelength (Chen et al. 1999), but according to Settle (2004), the ratio of reflectance in any two directions is independent of wavelength. This constraint has been used to drive atmospheric correction or in methods for the retrieval of aerosol optical depth (Guanter et al. 2005). Angular signatures have been found to discriminate vegetation type structure by measuring the hotspot, where the view zenith and solar zenith angles coincide (Lacaze et al. 2002).

1.5.1. Spectrodirectional Remote Sensing of Vegetation

Hyperspectral technology measures continuous and narrow spectral bands that are related to the amount of change in vegetation (Treitz and Howarth 1999). Hyperspectral imagery has the potential to become a unique and useful tool for monitoring ecosystem processes, nutrient cycles, and biochemical information, both at local and regional scales (Gastellu-Etchegorry and Bruniquel-Pinel 2001).

High resolution spectrodirectional remote sensing is an emerging form of remote sensing that offers more information for vegetation discrimination (Schaepman et al. 2004). This type of data offers the opportunity to analyze vegetation for both the biochemical and structural information simultaneously. For forestry applications it is feasible that this technology will offer improvements in species discrimination. For example, nadir based hyperspectral data alone, was found to discriminate temperate forest types, but inclusion of multi-angle data allowed for the additional discrimination of two deciduous forest type densities (Kayitakire and Defourny 2004).

An assessment of the relative contribution of both the directional and spectral component taken from overlapping aerial images of an agricultural area was performed by Barnsley et al. (1997). It was found that the spectral component was dominant and the directional component explained 21% of the red and 3% of the near-infrared's statistical variance. Vegetation structure can be distinguished from multi-angle imagery due to the forest's anisotropic properties. Gao et al. (2003) describes different anisotropic behaviour of forest canopy between the red and near infrared portions of the spectra due to geometric and volumetric scatterings respectively. In the infrared there is high leaf transmittance resulting in multiple scattering within the canopy, which in turn decreases the anisotropic effects in these wavelengths. In the red region, chlorophyll absorption reduces transmittance which results in high anisotropy. The result of this was two indices that are related to vegetation structure, a Structural Scattering Index (SSI) and a Relative Structural Scattering Index (RSSI) (Gao et al. 2003).

Settle (2004) found that the intrinsic dimensionality of full spectrodirectional data collected in a controlled experiment was mostly explained by the spectral component, followed by a smaller directional component. Due to the redundancy in the shape of the spectra viewed at all possible view and zenith angles, the directional data could be reduced to only three dimensions that explained 99.95% of the variance.

1.5.2. Radiative Transfer Models

A radiative transfer model (RTM) simulates radiation transfer processes in certain media, such as vegetation and atmosphere. For vegetation, it computes the interaction between solar radiation and plants. An RTM can model the reflected light of a forest for various view and lighting angles, but also for various forest types and structures.

Structural information that can be derived from multi-view angle remote sensing includes vegetation cover, gap fraction, plant dimensions, leaf orientation and Leaf Area Index (LAI) (Asner 2000). The usefulness of these models is the ability to invert them to create the forest structure parameters based on the reflectance of spectrodirectional imagery.

There are three basic kinds of radiative transfer models, ones that simulate reflectance at the leaf level, canopy level and hybrid models that combine the two.

1.5.3. Leaf Level Models

It is the biochemical concentrations of a leaf, along with their shape and structure that determine the shape of the absorption features of remotely sensed reflectance spectra (Dawson et al. 1998). Laboratory-based spectrometry uses standard methodologies to accurately estimate biochemical components in dried leaf sample (Curran et al. 2001). Curran (2001) suggests that biochemical concentrations can be estimated using lab-spectroscopy for the following in decreasing order of accuracy: total chlorophyll, nitrogen, sugar, chlorophyll a, cellulose, chlorophyll b, lignin, water, phosphorous, protein, amino acids to starch.

A leaf level model models how light interacts with the chemical structure and shape of a leaf. For example, the model PROSPECT (Jacquemoud and Baret 1990) has been based on a broad leaf and the model LIBERTY (Dawson et al. 1998) has been based on needles. To give a better idea on how a leaf level model works a detailed explanation on the LIBERTY model follows.

The LIBERTY radiative transfer model has been developed by Dawson et al. (1998) to construct the reflectance of a leaf based on the leaf's biophysical properties and biochemical concentrations. Biochemicals are localized in the hydrated cells that are

separated by air, and act as multiple refractive index discontinuities. LIBERTY models the radiative components of a needle as spherical shaped hydrated cells that have air gaps in-between. The model has been adapted from Melamed's theory of light interaction with suspended powders (Melamed 1963) and inters leaf optical parameters in the laboratory. The amount of light reflected at each encounter with a cell to air is calculated where the reflected light can either exit the leaf or encounter more cells internally at infinitum.

Light absorbed by the cells is transmitted with different energy, which is determined by the biochemical content of the cell; therefore a light with different spectral properties is produced. For example, infrared (1000 – 2400 nm) light is shaped by the bending and stretching of biochemical bonds (hydrogen–carbon and nitrogen–oxygen atoms) (Kemp 1991). Chlorophyll and carotenoid pigments strongly influence the visible region of the spectrum (Mackinney 1941). These pigments have strong energy due to electron energy transfer.

The leaf's structural properties are described by the following parameters within LIBERTY: Average internal cell diameter (m^{-6}), intercellular air space determinant, leaf thickness, linear (baseline) absorption and Albino leaf absorption. Cell diameter can be used to specify needles of a particular species and moisture content (dried vs. fresh needles). The intercellular air space determinant is the scattering efficiency where a higher value produces higher reflectance due to increased radiation scattering from the lower to upper layers. The leaf thickness determines what ratio of light is transmitted instead of reflected. The linear baseline and albino parameters are used to define the baseline spectra in which the absorption coefficients are added.

The four input parameters used to identify the biochemical content are leaf chlorophyll (mg/m^2), leaf water (g/m^2), Lignin/cellulose (g/m^2) and nitrogen (g/m^2). These parameters are incorporated into the LIBERTY model by specific absorption coefficients of pure components.

1.5.4. Canopy Level Models

Canopy models simulate reflectance of a forest canopy based on a modeled tree's shape, size and distribution by consider the distribution of radiation among leaves (White et al. 2001). The canopy modelled approach estimates total canopy reflectance that varies with changes in the foliage clumping index and effective Leaf Area Index (LAI) (Chen et al. 2003). Crop fields have been simulated by using radiative transfer models such as the SPRINT and DART (Lewis 1999) models.

The GORT model is based on the geometric shapes of trees rendered using ray tracing 3-D canopy model (Li et al. 1995). The models SPRINT and DART use ray tracing and a Monte Carlo simulations (Goel and Thompson 2000). These models are considered turbid-media radiative transfer models as each tree is considered a solid. These models are suitable for dense forests (Leblanc et al. 1999).

The geometric optical model such as "4-Scale" incorporates the canopy architecture. Leaf, shoots and branches are used to model the transmission of solar light through the canopy (Chen and Leblanc 1997). This physically based model are suitable for sparse forests as they take into account the sunlit and shadowed structure of the open canopies.

1.5.5. Combined Models

Studies have combined leaf level model PROSPECT linked to the canopy model SPRINT to model the effects of LAI, water thickness, cellulose and lignin, and protein

from MODIS (Zarco-Tejada and Ustin 2001). PROSPECT and DART were linked by Gastellu-Etchegorry and Bruniquel-Pinel (2001) to assess the robustness of spectrometric equations that predict forest chemistry. They concluded that these equations work better if there is less understory exposed, i.e., when the LAI and tree cover increase, and if the view direction become more oblique, unless in the hotspot and specular direction.

Combined models such as the geometric-optical forest canopy model named 5-Scale (Leblanc et al. 2002) were developed for LAI and fPAR algorithms refinement. 5-Scale is a combination of the canopy level model "4-Scale" (Chen and Leblanc 1997) and leaf level model LIBERTY (Dawson et al. 1999) models. This adds the ability to also account for forest bio-chemical values in the canopy. Although 5-Scale was utilized in this thesis, this research was based on field spectra, so the LIBERTY aspect was not utilized.

1.5.6. Model Benchmark

There is an international benchmarking exercise that has provided comparisons between various radiative transfer models giving an opportunity for model developers to test their code in controlled simulated experiments. The European Commission website RAMI have set up competition approximately every three years for anyone to use a radiative transfer model on standard data sets. The number of participating models has increased since 1999 by five new models for every competition showing the increased interest in the development of radiative transfer models. Results of the first competition can be found in Pinty et al. (2001) and the second competition in Pinty et al. (2004). The third competition is closed but the results were still in press at the time of this writing. Results from the second competition showed that despite the various approaches to the radiative transfer canopy models, the results are surprising similar.

1.5.7. Model inversion

The inversion of vegetation reflectance can be used to retrieve information related to the vegetation structure based on the input reflectance found in multi-view angle imagery. 5-Scale, for example, has been used to study the influence of different canopy parameters on the retrieval of biophysical properties with remotely sensed data (Leblanc et al. 1999). Inversions using 5-Scale based look-up tables to estimate chlorophyll content was performed by (Simic et al. 2010).

1.6. PLS

Hyperspectral data has allowed for a full-spectrum analytical method that offers relations between forest stand parameters and the resulting spectra. Two methods offered are Multiple Linear Regression (MLR) and Partial Least Squares (PLS).

MLR is an empirical method that has been used for example, to develop relationships between vegetation spectral reflectance and forest canopy biochemistry. Regression methods treat each spectral band as the independent variable and forest parameters or biochemical concentrations as the dependent variable. Multicollinearity occurs as the highly correlated hyperspectral bands cause the MLR matrix inversion to fail (Tobias 1995). This error can be overcome if there are a significant number of samples compared to the number of bands. The analysis selects only the wavelengths that have the highest correlations and throws out the rest.

An alternative approach has been to use the partial least squares (PLS) regression methods that reduces full-spectrum data to a smaller set of independent latent variables, with the dependent variable (constituent concentration or forest parameter data) used directly during the spectral-decomposition process (Shenk and Westerhaus 1991). PLS

has been applied using eigen analysis in which the full spectrum is reduced and then represented by a series of latent factors that has been extracted from the matrix of spectra and biochemical concentrations (Smith and Martin 2001) or forest stand parameters. The predictor coefficients extracted from the PLS analysis can be then multiplied by a spectrum of which the sum of the products will return the estimated dependent variable for that spectra. Therefore the predictor coefficients for each wavelength are directly related to the biochemical concentration or forest stand parameter of interest while at the same time it describes the spectral variation in the dependent variable (Smith and Martin 2001; Coops et al. 2003).

The input reflectance spectra extracted from the hyperspectral sensor can be transformed into either absorbance and/or the 1st or 2nd derivative from which the PLS is calculated. To convert to absorbance Equation 1 is applied to the plot level reflectance spectra where ρ is reflectance and ρ: A is the absorbance reflectance.

Equation 1. Conversion of reflectance to absorbance.

$$\rho: A = log10(1/\rho)$$

The concentration of an absorber (biochemical) in a leaf is directly proportional to the product of molecular spectral absorption, the concentration of absorbers and the path length of irradiating energy (Smith et al. 2002). This implies the spectra transformed into absorbance are more highly correlated to the depths of the absorption dips caused by the concentrations of foliar chemicals.

The second transformation is the derivative which normalizes remote sensing data by converting absorption features dips and peaks to inflection points. The derivative removes the base line offsets and low-frequency variations such as those caused by varying sun-sensor-target geometry (Smith et al. 2002). The first or second derivative of

a spectrum can be applied either to the original reflectance or the absorbance spectrum, and used as input into the PLS. Derivatives of a spectrum can be calculated a number of ways (see Figure 2). One way is to simply calculate the slope between two adjacent points resulting in slope calculation with a new band center (the mean distance between the two points). If one chooses the points on either side of current waveband, then the slope has been calculated for the current position based on the adjacent wavebands. This result often has produced identical slope calculated if one fitted a quadratic curve to three points and calculated the slope at the tangent of the current waveband centre. Using different methods of slope calculation can result in different results from PLS (Goodenough et al. 2005c).

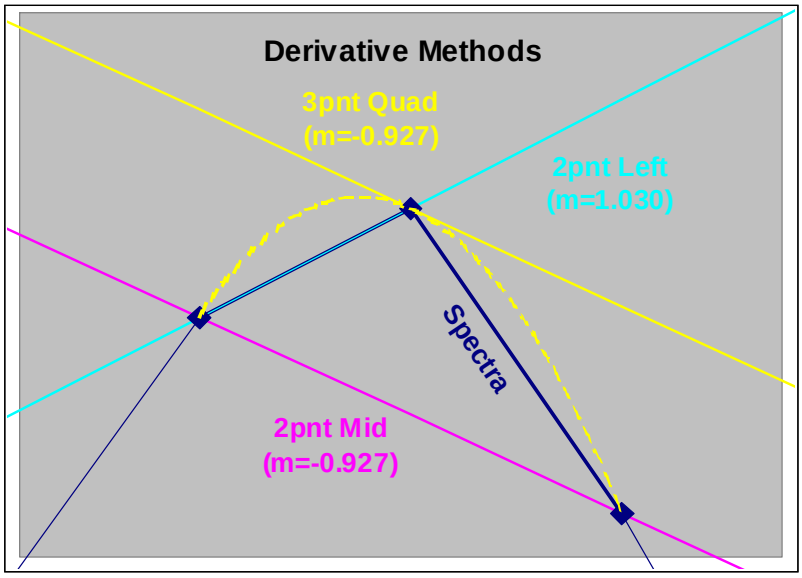

Figure 2. Example of Derivative Methods: **Two-Point Middle:** Slope of two neighbouring points, **Three-Point Quadratic:** Fit a polynomial through the three points and calculate slope of the tangent at the middle point**, and Two-Point Left:** Calculate slope of the point and its neighbour to the left.

Transforming the spectra also decreases the number bands input into the PLS and the wavelength assigned to coefficients are dependent on which transformation has been

applied. The reflectance or absorbance spectra input into PLS would produce the same number of coefficients as bands (n); therefore, the coefficients would be related 1:1 to the wavelength of the bands. A first derivative transformation that uses a neighbouring band to calculate the slope (2 points left) would lose a band (n-1), so the coefficient would be assigned to a point between the two wavelengths. If the slope has been calculated by looking at neighbouring bands using either the two points middle or quadratic, the result would be two less coefficients than bands (n-2). The first coefficient would be influenced by the first three bands and assigned a wavelength of the second band. A second derivative is equivalent to having the first derivative applied twice. Therefore the 2nd derivative 2 points left can be calculated using the first three bands and the wavelength assigned starting at the second band. A 2nd derivative using the middle or quadratic transformation requires five bands to calculate, resulting in four less coefficients than input bands (n-4). The wavelength assigned to the first coefficient is band 3.

Table 1. Transformation type and the resulting number of coefficients compared to the number of bands (n). Width is the number of bands used to calculate the transformation and Label Start is the band name used to label the first coefficient.

Transformation Types	#coefficients	Width	Label Start
Reflectance	n	1	1
1st derivative (2 points left)	n-1	2	1
1st derivative (middle/quadratic)	n-2	3	2
2nd derivative (2 points left)	n-2	3	2
2nd derivative (middle/quadratic)	n-4	5	3

By transforming the spectra before input into PLS, results can be improved. Both Coops et al. (2003) and Smith et al. (2003) found better relationships with canopy nitrogen concentrations with derivatives of the absorbance spectra than with only reflectance spectra. To get an independent error analysis, one would do a cross validation.

PLS regression coefficients from a training subset of the input spectra would be compared to the estimated concentration from the testing data. The independent test can be repeated using random selection of the training and testing data from the plot data to determine an error margin on the coefficient of determination. This PLS method was used in estimating biomass from forest spectra by Goodenough et al. (2005c) and foliar nitrogen concentration by Coops et al. (2003).

The independent tests can be repeated for all possible transformations of the spectra. The results are a series of R^2 coefficient; that show the best results for the forest parameter and transformation combination. An error estimate can be made by looking at the range of all the standard deviations (Goodenough et al. 2005c).

Shenk and Westerhaus (1991) first showed the use of PLS using near infra-red spectra for agricultural products hay, haylage, corn, wheat and barley. Smith et al. (2002) utilized PLS to determine forest productivity with AVIRIS data collected over a diverse forest located in White Mountain National Forest, New Hampshire, USA. Plots were measured over two time periods to get an estimate of forest productivity. Foliar samples were acquired from plots to determine the foliar concentrations of Nitrogen using laboratory methods. Smith reported an $R^2 = 0.82$ that measured whole-canopy N concentration and transformed AVIRIS absorbance spectra. Coops et al. (2003) used PLS and MLR to estimate Nitrogen concentrations in the foliage of Eucalyptus trees using the spaceborne hyperspectral sensor Hyperion. The authors found a high level of correspondence between the MLR wavelengths selected and the PLS regions with high loadings, especially in the chlorophyll absorption region of the spectrum.

1.7. BRDF Satellites

Monitoring and modeling terrestrial carbon cycle has been a driver for space missions (Chen et al. 2003). Multi-angle satellites have been developed with global coverage in mind such as the joint French and Japanese venture known as POLDER and POLDER-2 and NASA's MISR (Diner et al. 2002) are examples of such satellites.

The POLDER sensor onboard the Japanese satellite platform ADEOS measured the reflectance of the entire land–atmosphere terrestrial system. The swath width was 2400 km wide, repeated every four days and during a given overpass, 14 image angles were recorded of a 6 km pixel on the ground. The first POLDER satellite operated in the period between November 1996 and June 1997 (Lacaze et al. 2002). POLDER 2 on ADEOS 2 operated under nominal conditions from April 2nd, 2003 to October 24th, 2003, producing around 7 complete months of measurements. These short lived flights have produced valuable multi-angle remote sensing data sets (Wenge et al. 1999; Lacaze et al. 2002; Chen et al. 2003; Bacour and Bron 2005).

MISR operates aboard NASA's Terra spacecraft, producing images with 9 view angles during a single overpass. The pixel size is 275 m and 1.1 km and the swath width is 380 km (Diner et al. 2002). MISR continues to provide multi-angle remote sensing data (Asner 2000; Bruegge et al. 2002; Diner et al. 2002; Nolin 2004).

Although these global coverage multi-view spacecrafts are essential in the development of estimating global vegetation parameters related to Carbon (Chen et al. 2003), they lack the fine pixel resolution required for multi-view hyperspectral analysis of forests at the stand level.

1.7.1. ESA CHRIS/PROBA

In 2001, ESA launched PROBA, a small satellite as a technology demonstrator. One of the instruments on board is CHRIS, which acquires imagery from 415 nm to 1050 nm. It can acquire data in 5 modes that allow CHRIS to acquire from 18 programmable wavelengths to 62 continuous bands at the full spatial resolution of 18 m or 36m respectively. CHRIS acquires 5 hyperspectral images over an angular range of ±55 degrees along track during a single overpass (Cutter 2005).

1.8. Chapter Conclusion

It is with high spectral, spatial and directional resolution imagery from CHRIS that forest structural parameters will be addressed over the Greater Victoria Watershed District. This analysis will require an understanding of the anisotropic nature of forest canopies as measured by spacebourne hyperspectral sensors and modeled by radiative transfer models.

Chapter 2. Multi-Temporal, Multi-Angle Evaluation with CHRIS of Forests

2.1. Abstract

The Compact High Resolution Imaging Spectrometer (CHRIS) is aboard the ESA PROBA satellite. CHRIS acquires imagery from 415 nm to 1050 nm in five pre-programmed modes. In mode 4, CHRIS acquires 18 bands with emphasis on the red-edge at the full spatial resolution of 18 m. CHRIS acquires 5 hyperspectral images over an angular range of 55 degrees along track. One image set was acquired within one day of a Hyperion acquisition. In 2004, five clear CHRIS image sets were acquired throughout the summer over the Greater Victoria Watershed District (GVWD). These CHRIS acquisitions were undertaken for the Evaluation and Validation of CHRIS for National Forests Project (EVC) (Goodenough et al. 2006) The Principal Investigator for the EVC Project was Dr. David Goodenough. The many new challenges of working with multi-angle and multi-temporal imagery such as orthorectification and atmospheric correction related to producing forest products are discussed in this chapter. This chapter reports on the analysis of these CHRIS data for creating forest data products for species recognition for sustainable forest management. Emphasis has been given to the utilization of the multi-angle multi-date characteristics of these data takes.

The multi-angles of CHRIS improve the accuracies of forest species recognition and stand densities compared to a nadir view only. Testing on five dates saw an average overall accuracy improvement of 14.3% for non-aggregated results and 8% improvement in the aggregated results. Combining multi-date nadir imagery also provided an improvement in classification accuracy by 14.3% and the non-aggregated accuracy by 10% (Dyk et al. 2006).

2.2. Introduction

The PROBA platform's versatility allows for multi-angle hyperspectral CHRIS images to be collected over a target at five angles in a single pass. These data provide many challenges in pre-processing, but have the potential to provide accurate forest information products. A series of these acquisitions over a season provides the opportunity to evaluate the potential to provide accurate forest information products with multi-date, multi-temporal imagery.

Five overpasses during 2004 provided clear scenes from CHRIS approximately every two months starting in April until the end of October. These CHRIS acquisitions were undertaken for the Evaluation and Validation of CHRIS for National Forests (EVC) Project (Goodenough et al. 2006). The multi-date imagery over the growing season is another valuable data set that can be used to see if the changes in spectral characteristics of forested areas can improve classification accuracies.

2.3. GVWD Site

The Greater Victoria Watershed District (GVWD) is located northwest of Victoria on Vancouver Island, British Columbia, Canada. The forest cover is comprised predominately of Coastal Douglas-fir (*Pseudostuga menziesii*) and Western Redcedar (*Thuja plicata*), in the forest canopy and salal (*Gaultheria shallon*) as the dominant understory. The watershed contains some of the oldest unmanaged stands of Douglas-fir in the southern half of Vancouver Island (Goodenough 2003). The relief of the study area is approximately 600 meters with an average elevation at 400 m above sea level. The slopes vary but may attain gradients as great as 45 degrees.

2.4. Data Sets

ESA launched the Project for On-Board Autonomy (PROBA) small satellite as a technology demonstrator in 2001. One of the instruments on board was the Compact High Resolution Imaging Spectrometer (CHRIS), which acquires imagery in the visible and near-infrared bands from 415 nm to 1050 nm. CHRIS acquires 5 hyperspectral images over an angular range of ±55 degrees along track.

Data acquired of the GVWD test site during the summer of 2004 includes five dates of CHRIS multi-angle imagery, a Hyperion image and ground spectrometer data. For each date there are five images (see Table 2), each taken at a different angle. The satellite position is described terms of two angles: the fly-by zenith (FZA) and minimum zenith (MZA) angles (Cutter 2005). The position of the satellite during each acquisition date and angle are illustrated in Figure 3.

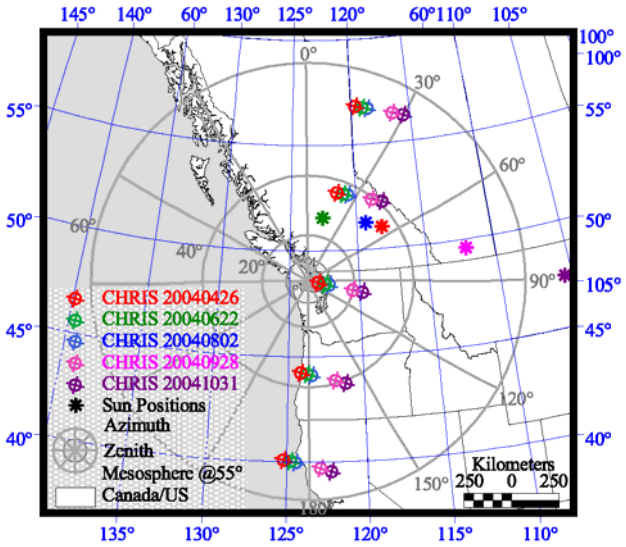

Figure 3. Polar type plot of CHRIS acquisition over the GVWD showing the approximate satellite location for each FZA and sun position of each of the five dates (during the summer of 2004).

Table 2. CHRIS image data collects over the GVWD.

Date	Time (GMT)	MZA	PROBA Altitude	Ground Collection Data	Images
26-Apr-04	19:29	5°	561	No	4
22-Jun-04	19:32	8°	652	No	5
2-Aug-04	19:32	10°	551	No	5
28-Sep-04	19:25	21°	666	Yes	5
31-Oct-04	19:24	24°	585	No	5

The MZA is defined as the minimum angle between the target zenith and the platform. The point on the ground track when the MZA occurs is called the sub-satellite position at maximum approach (SSMA). Negative MZA values correspond to target locations east of the ground track.

The FZA is defined as the angle between the SSMA zenith and the platform. The five images are taken when the FZA is equal to approximately ±55°, ±36° and 0°. Positive angles are north of the target for GVWD.

It was necessary to manually calculate the azimuth and zenith angles as our data did not include that information. Using a spherical geometric method produced results that were within 1° of the orbital propagation method as described by Alonso and Moreno (2004).

CHRIS has five modes of operation (see Figure 4). Mode 1 covers the full swath of 13.4 km, with 62 bands ranging from 411 nm – 997 nm. It has a variable FWHM (6 nm-20 nm) and a 34 m ground sampling distance (GSD) at nadir. Mode 2 has 12 water bands acquired at 18m. Mode 3 and mode 5 are called land channels. Mode 5 has 36 channels and half the swath width instead of 18 bands and full swath width of Mode 3. Mode 4 has18 bands, ranging from approximately 485 nm to 800 nm and was also used for the EVC project. The emphasis was on sampling the chlorophyll bands along the red-edge,

where 15 of the 18 bands are in the range of 650nm to 800 nm at a FWHM of 6-8nm. The wavelengths for each band vary depending on the satellite temperature (Cutter 2005). This change is only a small fraction of a nanometer. The data for each band, including the band minimum wavelength, maximum wavelength, middle wavelength and full-with half-maximum is included in the image header.

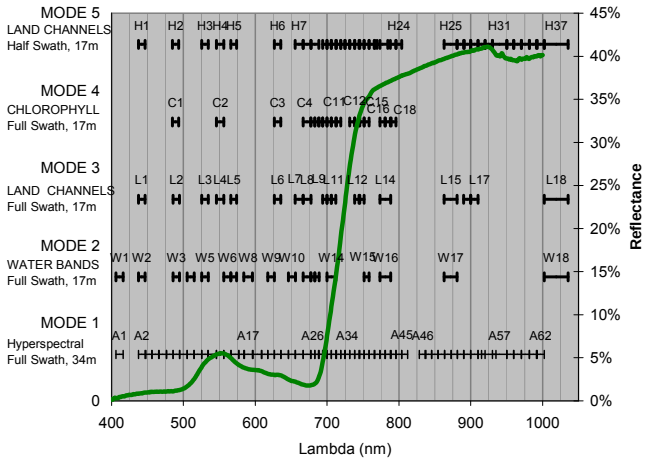

Figure 4. The five modes of CHRIS data acquisition overlaid with a typical vegetation curve. (Data from Cutter (2005).)

In 2004, CHRIS data from the European Space Agency (ESA) were delivered to the EVC project with level 1A processing in the CHRIS HDF version 3.1 format. The data were stored in 32-bit integer format, which allowed storage without gains or offsets. The raw DN values were in radiance units of μW/(m² • nm • sr). In December 2004, the CHRIS data format was updated to version 4.1 (Cutter 2005). CHRIS files had the same file properties, but included additional satellite geometry such as the satellite zenith and azimuth viewing angles.

The spatial resolution of the Mode 4 images varies from 18m (0° FZA, 0° MZA) to 30m (55° FZA, 21° MZA) in the along track direction (see Figure 5). The images are 766

x 748 pixels in size, covering an area ranging from around 13.8 x 13.5 km to 22.4 x 13.5 km.

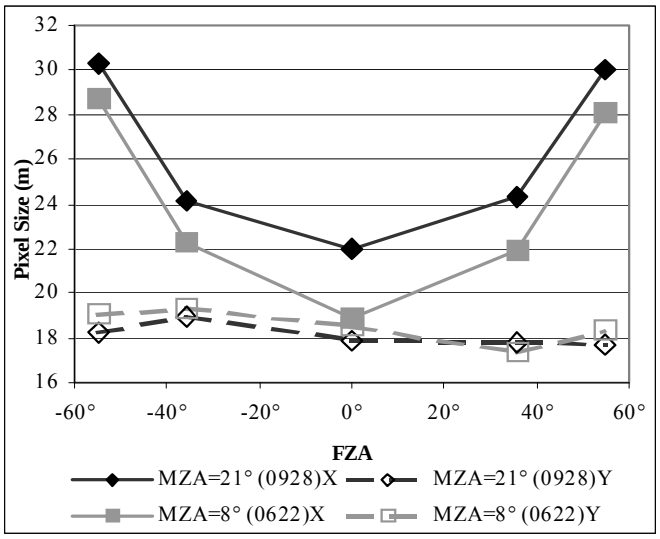

Figure 5. Pixel size varies in cross-track direction with FZA and MZA.

Noise reduction of CHRIS data has been implemented by Garcia and J.Moreno (2004). Atmospheric correction was done using Fast Line-of-sight Atmospheric Analysis of Spectral Hypercubes (FLAASH). FLAASH is an ENVI extension, built on the MODTRAN4 atmospheric modeling program. MODTRAN4 is designed to handle off-nadir satellite geometry, making it applicable to CHRIS data.

The area requiring a homogenous atmosphere around a target increases with off nadir viewing. Atmospheric effects occur below the top of the mesosphere, which extends to approximately 80 km above Earth's surface. If the mesosphere is projected onto the ground from the maximum angle at which CHRIS/PROBA can look at a target, 55°, a region is formed as shown in Figure 3. This is the region where we have to consider the influence of atmospheric variance.

Orthorectification was performed using PCI's orthoengine software. Approximately 50 GCPs and 15 checkpoints were collected over each image date and each angle and then applied using a rational function model (RFM). RFM allows for the correction of imagery in higher topographic relief areas using only GCPs and a digital elevation model (DEM). The high amount of relief in the GVWD study areas requires orthorectification, especially for the multi-angle imagery.

To analyze all five dates of imagery, a common area bitmap was defined in which all dates and all angles are free of clouds and any image artifacts. This can be seen as the central white area in the image count map (see Figure 6)

It was decided to not include any of the images with an FZA of -55° as only one image from this angle was suitable (see Figure 7). The April 26, 2004 data set didn't include this angle, both the October 31, 2004 and the June 22, 2004 image with FZA of -55° had significant clouds, the August 2, 2004 FZA -55° image pointed too far north and would cut off a significant portion of the study area. Only the September 28, 2004 FZA of -55° image was clear. A five angle classification was performed by Goodenough et al. (2005b). For this analysis only the four FZA angles of +55°, +36°, 0° and -36° will be included to make a comparison that is common to all dates.

Composite images at 20 m were created from the four FZA angles for each of the five dates as well as all the nadir images of all five dates. The four FZA composite image consisted of 72 bands; 18 bands for each of the four angles. The five-date nadir image contained 90 bands, 18 bands from each of the five dates (see Figure 8). Analysis was also performed on each of the 18 bands representing the nadir angles for each image date.

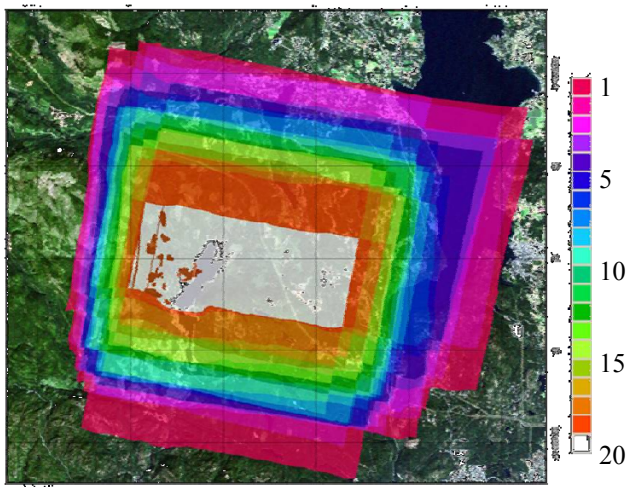

Figure 6. Image count map, each colour represents the number of scenes covering an area of ground. White area represents the common area for all images acquired in 2004.

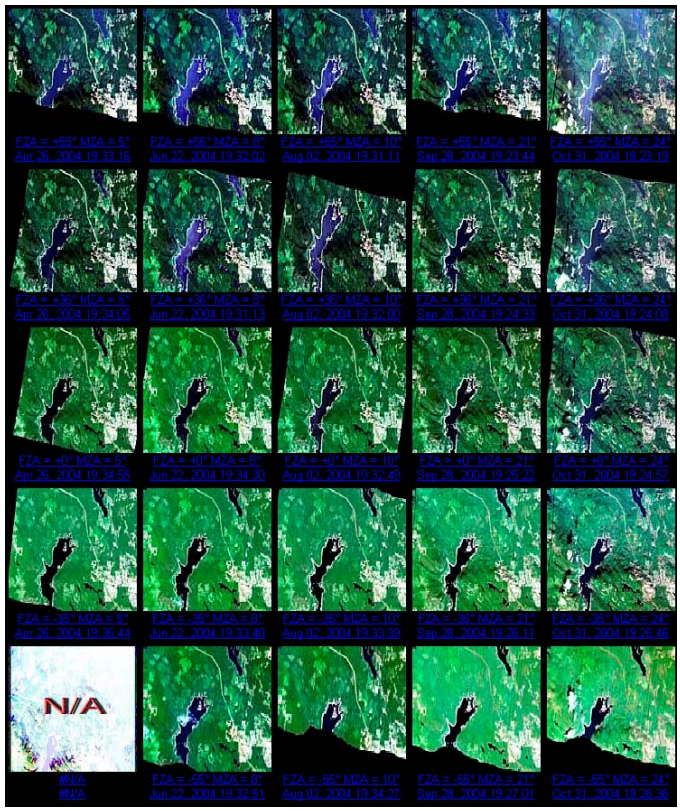

Figure 7. Combined each date (each column) (angles +55° to -36° top row to fourth row) as a 72 band image stack. Processed combined 5-date nadir data stack (90 bands, centre row) , Process individually nadir images (18 bands each). Lack of quality data in -55°.

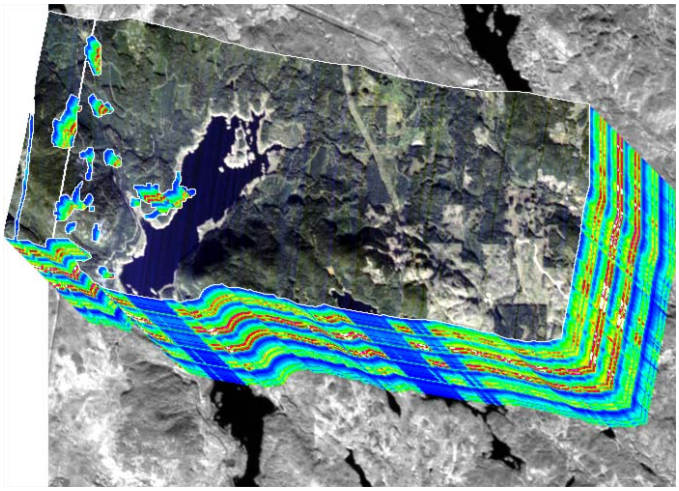

Figure 8. Nadir stack; 5 dates, 18 bands each = 90 bands

MNF transforms were performed on the 90-band composite images of the nadir stack, as well as the 72 band composites of each date and individual 18-band nadir images, with estimated noise statistics derived from the imagery under the common area mask. The MNF transforms were used to reduce the dimensionality of the data and only the first noise-free eigen channels were used as input into a supervised classification.

Ground validation polygons were selected in the common area to support a supervised classification. These areas were selected from forest polygons and verified using high resolution aerial photography and visual inspection of the imagery. The classification methodology adopted is described in Goodenough (2003). Fourteen classes were used in training the supervised signatures. A maximum likelihood classification was performed with these training classes. These classes were then aggregated to 9 classes, consisting of 4 forest species (see Table II). A random bitmap expanded to 3×3 pixels was used to separate approximately one fifth of the validation pixels to give an independent check of the results.

2.5. Results

The striping of the Level 1 CHRIS data was dramatically reduced as a result of the noise corrections. Figure 9 shows part of a CHRIS image before and after noise removal.

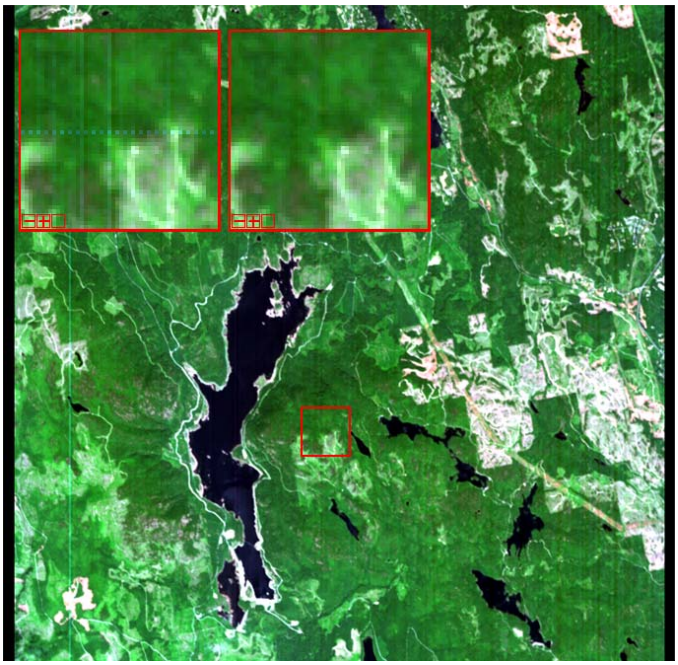

Figure 9. Horizontal and vertical noise removal of CHRIS imagery can be compared in the insets of this September 28, 2005, -36° FZA image (RGB Bands 4,2,1)

Evaluating the horizontal noise found in the five dates of the Mode 4 imagery showed that the noise is not evenly distributed. Bands 13-18 (742nm - 792nm) contained 78% of the 795 bad lines, and 69% were found in the two backward looking FZAs (-36° and –55°). There was no horizontal noise found in the first three FZAs of the September 28th and October 31st images.

Atmospheric correction of the nadir view compared reasonably well with both the Hyperion image acquired the previous day and the ASD ground spectrometer data of our calibration site, the “Farmer’s Field” (see Figure 10). This field is a large, flat, relatively homogeneous target suitable for calibration measurements. The farmer’s field represents a ground target that could be measured both from the satellite sensor and by ground based

instruments in order to provide reflectance calibration coefficients that could be applied to each image. Negative values were encountered when atmospheric corrections using FLAASH were made of the off nadir scenes. A constant was added to all non-nadir spectra to tie the spectra to the first band of the nadir angle image. Subsequent analysis was limited to analysis that required relative spectra, such as MNF and classification.

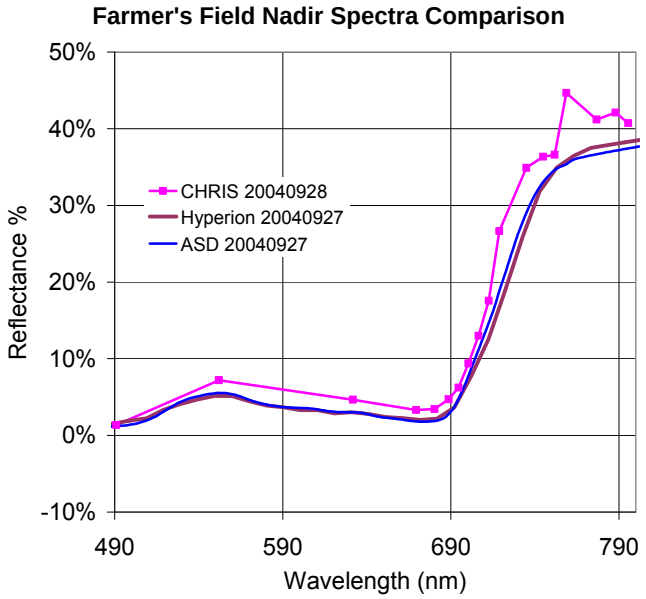

Figure 10. Spectral comparison of Nadir CHRIS, Hyperion and ASD over the Farmer's field collected September 27 and 28, 2004.

CHRIS imagery had constant vertical striping that was due to errors in the sensor alignment that was removed (Garcia and J.Moreno 2004). A more subtle vertical noise caused by thermal fluctuations remained. There also remained a strong vertical band near the left hand side of the images that proved too wide to remove. This banding has been noted in all CHRIS imagery (Cutter 2002).

For the September 28th image the average RMS positional errors reported for all dates and FZA angles were 0.95 pixels. The greater the FZA angles, the higher the RMS. For example, for ±55° the average RMS was 1.1 pixels, ± 36° was 0.95 and Nadir was 0.72.

The RMS in the Y direction is the main contributor to this increase in error. Pixels are elongated in the X direction as the sensor attempts to keep the Y size constant during acquisition. Imagery acquired at the larger FZA angles, had pixels elongated by an additional 2/3, creating an image that appeared smeared in the across track direction. The calculated pixel size in the X and Y dimensions for two of the image dates are shown in Figure 5.

An MNF transform was performed on each of the 72-layer stack of the four FZAs for each date, each 18 band nadir image and the 90 band nadir stack. Inspection of the eigen bands showed that the first 8 eigen bands derived from the 72 layer and 90 layer stacks and the first 5 eigen channels of the nadir images could be used as input into the supervised classification; vertical striping dominated the remaining eigen channels. An example of an aggregated classification map is shown in Figure 11.

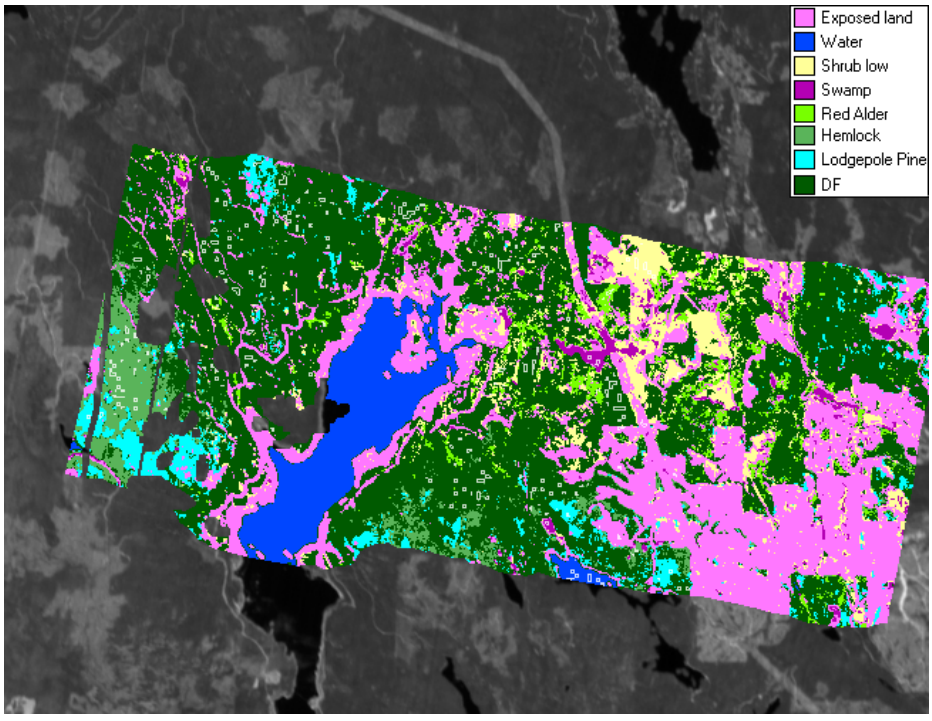

Figure 11. Aggregated classification results by combining Nadir images from all dates. Areas outlined in white indicate classification check areas (Dyk et al. 2006).

A similar improvement is also found by combining multi-date imagery. The aggregated accuracy of the single-date nadir only images was on average 80.3%. A fused data stack of all these nadir images produced an accuracy of 90.2%, an improvement of approximately 10% demonstrating the importance of multi-temporal data for forest classification.

The nadir only, single-date images performed poorly before the classes were aggregated; this can be expected as there were only 18 bands, all of which were in the VNIR. Multi-angle combination provided an improvement in the classification results before aggregation was performed. For the individual classes (not aggregated) nadir only images averaged an overall accuracy of 51.7% (cyan line in Figure 12) and the multi-angle images produced an average of 65.2% (light orange line in Figure 12). Combining all the nadir images produced an overall accuracy of 69.3% for the non-aggregated results, an improvement of 17.6% from the average nadir only accuracy.

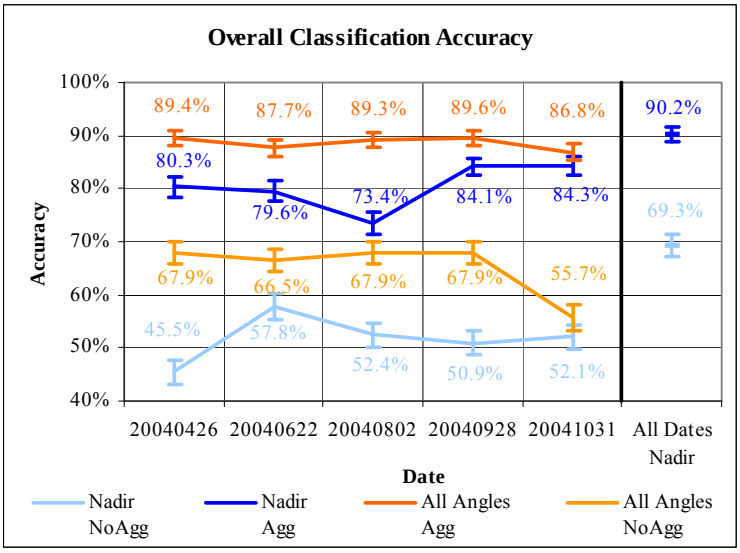

Figure 12. Classification accuracy comparison. Orange lines show results by combining all angles. Blue lines are only nadir for each date and combined all nadir (Dyk et al. 2006).

The October nadir only non-aggregated results performed significantly poorer (55.7%) than the other dates. There was confusion within the larger Douglas-fir class, which improved after aggregation. The October image had a much lower sun angle and therefore more shadows were cast in areas of higher elevation.

The April non-aggregated nadir only image also performed poorly (45.5%), again mainly due to confusion within the larger training area of Douglas-fir. After aggregation the nadir classification for April was consistent with the other dates.

The August nadir only image classification accuracy of the aggregated results also seemed to be significantly lower than the other dates (73.4%). The Douglas-fir class was confused with Hemlock.

2.6. Chapter Conclusions

CHRIS imagery offers new potential in forest product creation. There are many new challenges in dealing with the multi-angular imagery. We have looked at an improvement in classification of forest species by using all the angles provided in a single overpass and all the nadir images over a growing season.

There remains residual striping, even after removing random horizontal noise and constant vertical striping, as was evident in the later MNF channels. By using all FZA angles provided in a single date image, the inherent noise seems to be reduced as can be seen in the patterns of the classification results.

The 18 bands provided in Mode 4 are concentrated along the red-edge. Atmospheric correction results can be improved by determining the column water vapor amount for each pixel in the image. This requires the band set to include bands at a spectral

resolution of 15 nm or better that span at least one of the following ranges: 770-870 nm or 870-1020 nm for the 820 or 940 nm water feature respectively (RSI 2004).

Our study site has a wide range of topographic relief and with the early version of imagery there is no satellite orbital model available for CHRIS imagery. Geometric correction is then best done by orthorecitifying with a rational function model where the model is derived from the GCPs and a DEM.

The multi-angles of CHRIS improve the accuracies of forest species recognition and stand densities compared to a nadir view only. Multiple views of the target area improved the discrimination of stands with different densities. Testing this over five dates we saw an average overall accuracy improvement of 14.3% for non-aggregated results and significant 8% improvement in the aggregated results.

Combining multi-date nadir imagery also provided an improvement in classification accuracy. On average, combining the nadir images over five dates during the growing season improved an aggregated average overall accuracy by 14.3% and the non-aggregated accuracy by 10%.

Multi-angle data for CHRIS analysis of forest species can provide higher accuracy and easier to obtain than multi-date.

Chapter 3. CHRIS Acquisition Field Calibration Method

3.1. Introduction

The purpose of this chapter is to summarize the methodology of collecting spectral calibration data in the field with the intent of calibrating multi-angle CHRIS data to nadir normalized reflectance. During a single over pass, the CHRIS sensor collects imagery of a target at five Fly-by Zenith Angles (FZAs) at approximately ±55°, ±36° and 0°. Multiple overpasses also will provide these angles at various Minimum Zenith Angles (MZAs) as the orbit changes on consecutive days. Calibration of these imagers requires the collection of spectra from a relatively homogeneous target that can be measured on the ground at the same angle. The ground spectra are then used to calibrate reflectance spectra made by an atmospheric modeling program such as FLAASH or ATCOR-3 as suggested by Kneubühler et al. (2005).

Previous attempts to atmospherically correct off-nadir images from CHRIS acquired in 2004 where not successful due to the atmospheric correction model's inability to handle off-nadir imagery, the lack of water features in the Mode 4 CHRIS imagery, and no off-nadir ground spectra (see previous chapter or (Dyk et al. 2006)). Acquisitions of CHRIS imagery over the GVWD (Figure 13) in 2006 can be used to solve some of these issues. The data acquisition during the summer of 2006 are in MODE 1, the full hyperspectral mode, 36 m resolution in the along track direction and approximately 36 m to 50 m resolution in the across track direction depending on the FZA. Acquisitions in a continuous hyperspectral mode (400-1000 nm) capture the water vapour features at 800 nm.

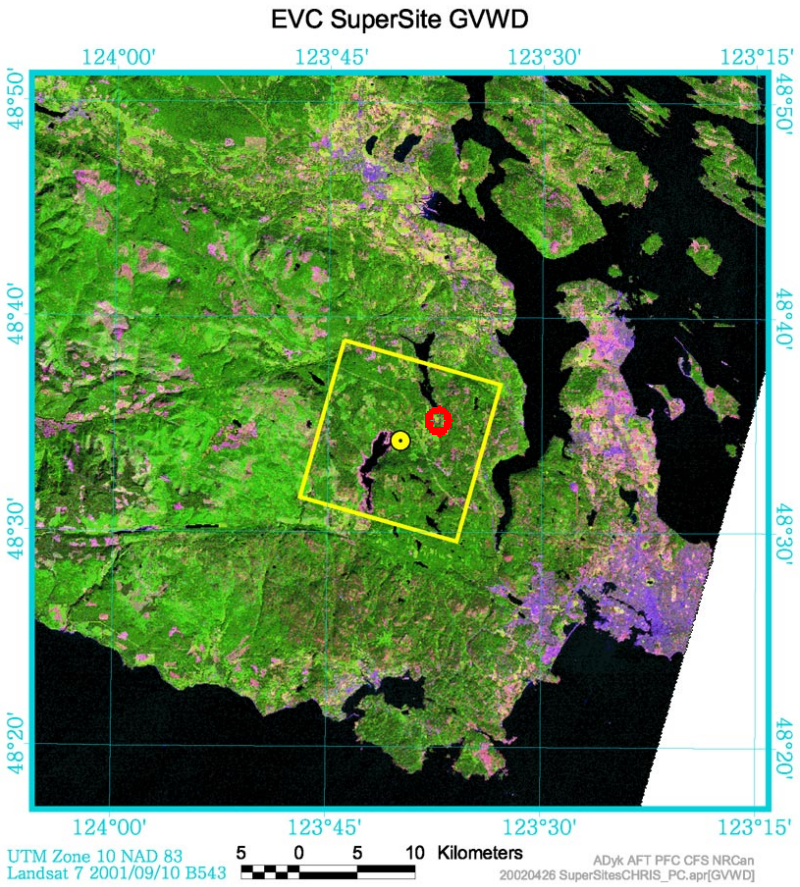

Figure 13. Location of EVC center target in GVWD (yellow point) and the farmer's field (red circle).

Near the GVWD is a farmer's field just south of Shawnigan Lake. This chapter will outline a methodology used to collect field spectra at various angles that coincide with the CHRIS acquisitions and allow for calibration of imagery at all FZAs and MZAs. The objective of acquiring multi-angle field spectra is to develop a function between off-nadir spectra to nadir spectra. This function can then be applied to the spectral walks to provide the equivalent off-nadir ground calibration over an area large enough to be used to calibrate the satellite imagery.

3.2. GVWD Opportunities

During the summer of 2004 five relatively clear CHRIS images were acquired, but only one image coincidently had some spectral ground calibration. The September 29, 2004 image was acquired the day after a Hyperion image was acquired. Spectral measurements were made at nadir only.

On September 2nd to 4th 2006, a triplet acquisition provided 15 look angles in three consecutive days with MZAs of 20°, -2° and -23° (see Figure 14 and Table 3). The CHRIS overpass schedules are updated weekly and projected only six weeks out.

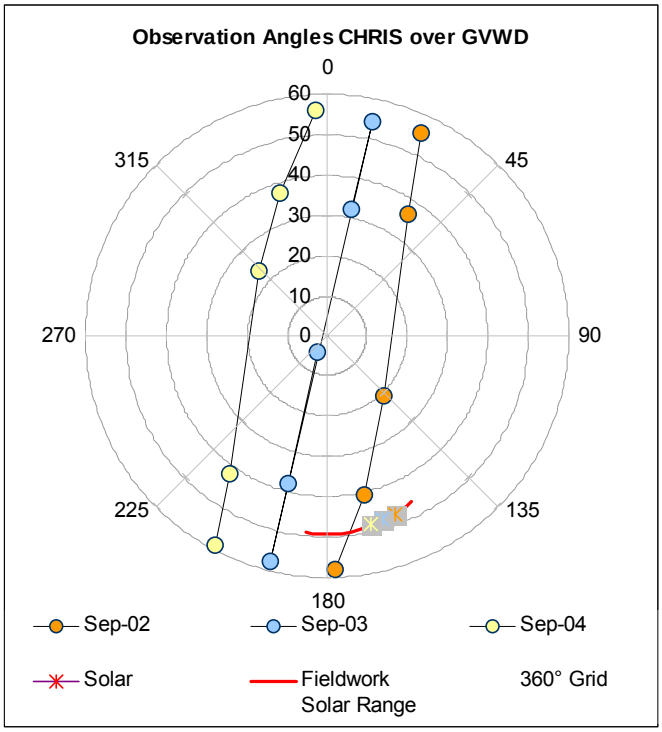

Figure 14. Polar plot of CHRIS acquisition over the GVWD showing the satellite location from the meta data for each FZA and sun position of each of the triplet dates in Sept. 2006.

Table 3. GVWD Triplet acquisition

GVWD	Time (UTC)	SatZen	Solar Zen	Altitudes
9/2/2006	1917	20°	43°	551km
9/3/2006	1928	-2°	42°	551km
9/4/2006	1939	-23°	42°	551km

3.3. Calibration Site

The farmer's field is located at the southern tip of Shawnigan Lake in Southern Vancouver Island at 48°38'21"N, 123°37'25"W (red circle in Figure 13). The owners Dale and Teresa Erb have permitted access to this field as long as the hay crop isn't planted (April till June).

A detailed ortho-photo of the field can be seen in Figure 15. The field is divided by ditches into various sections. A visit to the field during a potential acquisition of 2006 revealed that the center west section of the field (section A) had a relatively homogenous grass cover. The grass cover in section B had many clumps of darker shaded grass. The tree located a point "T" is a dominant landmark. It was decided that section "A" would be used for calibration. This area is approximately 10 ha or approximately 175 m by 60 m.

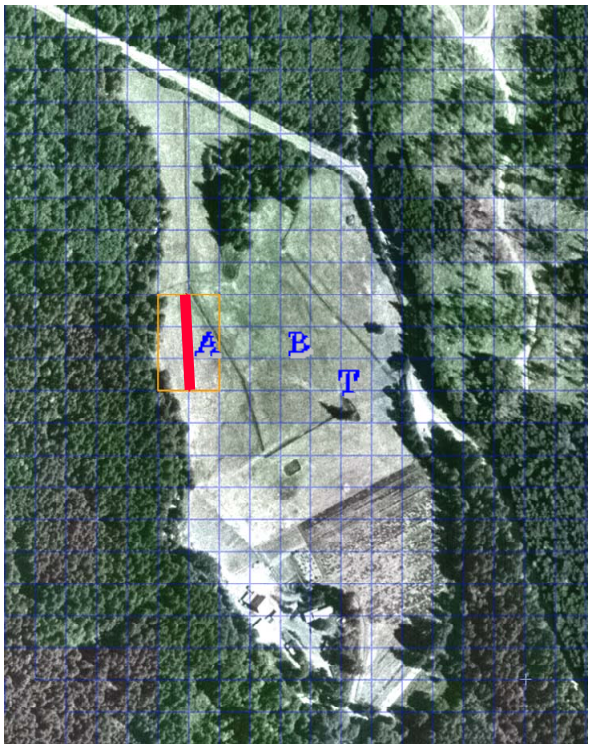

Figure 15. Example of spectral walks used to calibrate hyperspectral data on a 36m grid.

3.4. Calibration Process

3.4.1. Nadir Walks

For nadir only hyperspectral imagery, such as AVIRIS and Hyperion, calibration spectra has been created by acquiring nadir spectra during "walks" with an ASD along various lines in the farmer's field (Goodenough 2003). A relatively large area is covered by taking long straight walks whose endpoints are measured with a GPS unit (see red line in Figure 15). The geographic location of each spectrum taken during the walk was estimated from these endpoints. All spectra that fall within a set of pixels were selected and the average spectrum represented those pixels.

This nadir type of approach was required for the calibration of CHRIS data in order to cover an adequate spatial area. In addition, there needed to be an added dimension by creating a multi-angle estimate of each spectrum in a walk. With the use of a simple goniometric system, the relationship between a nadir spectra and the other five CHRIS angles (±55°, ±33° and +00°) for various MZAs were established. As this process was time consuming compared to spectral walks, spectral walks ought to be acquired before an overpass, and then the time during the overpass had to be dedicated to the goniometric measurements. The nadir measurements of the walks were less sensitive to anisotropy caused by only the small change in the sun angle, and could be performed before and/or after the actual data of acquisition.

3.5. A Simple Goniometric System

The simplified Goniometric System was geared to develop three relationships between the CHRIS nadir view and the off-nadir views of ±55° and ±36°. It was based on the assumption that the farmer's field represents a ground target that could be measured both from the satellite sensor and by ground based instruments in order to provide reflectance

calibration coefficients that could be applied to each image. The CHRIS instrument observes the ground target from various angles, each of which needed an independent ground calibration due to the anisotropic nature of the field. Field measurements were made during similar observation conditions to that of the satellite to minimize the effects of changes in sun angle.

A reference line in the direction the principle plane of the orbit was staked in the grass using dark dyed string with black ribbons marking positions every meter (Figure 16). A GPS position of the start and end of the line was recorded. The direction of the principle plane was approximately 171° magnetic north. This measurement was equivalent to 189.38° grid north minus the 18.22° magnetic declination.

Figure 16. Laying out a reference line along the orbital plane.

The reference line aided in the positioning of the tripod. The tripod holds a Manfrotto 303SPH head (Figure 17) with one sliding plate removed. The ASD pistol grip is attached to the tripod head giving it the ability to pivot to any angle toward the ground (Figure 18). To account for the MZA of the satellite, the tripod is tilted back with an angle locator so the pistol grip points outward from the tripod to match the viewing angle of CHRIS (see Figure 19).

Figure 17. The 303SPH is a multi-row panoramic photography head.

Figure 18. Adjusting for an MZA of -9°.

Figure 19. Setting up the simple goniometric system. FZA emulated by rotating the ASD along the flight path.

The whole tripod assembly was setup over the reference line, and five spectral measurements were made at each meter along the line. By having the pivot point of the tripod set up at a height of 1.49 m, all the five angles viewed the same patch of grass every 1m along the reference line (see Figure 20). The foot print increased in size with the greater angles. The ASD fibre had an 8° IFOV attached that provided an approximate footprint of ellipsoids: ±53.8°, 0.37×0.64m, ±33°, 0.26×0.32m, nadir, 0.21× 0.21m.

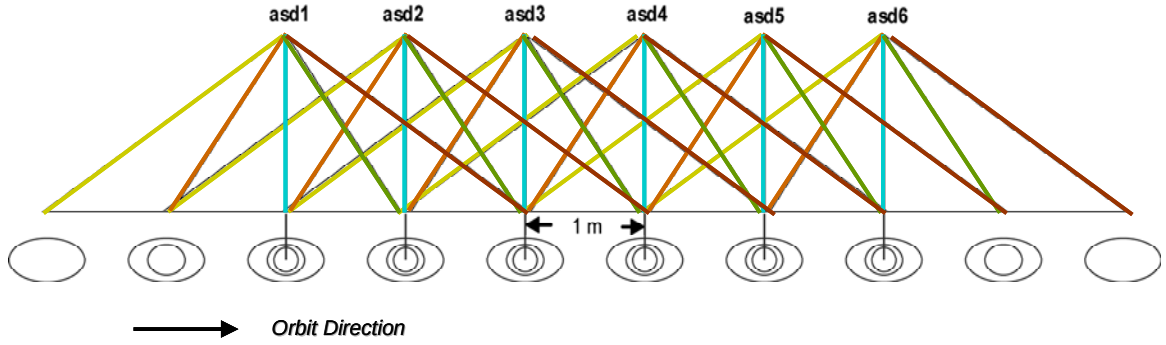

Figure 20. A simple goniometric system with movement along orbit reference line. Distance between points is 1m, the ASD height is 1.49m, ASD IFOV is 8°, view angles ±55°, ±33° and +00° approximate footprint ellipsoids shown to scale.

The targets over the patches of grass are shown in Figure 20 with the approximate ellipsoids overlaid for each ASD position. In this configuration, as acquired during the September 2-4 overpasses, one can see a variability of green and dry grass. For each ASD position spectra, from five angles where acquired for two of the MZAs 20° and -2° during the orbital overpass. The third MZA (-23°) was not measured due to time constraints which would have resulted in significant variation in the sun's position compared to its position during the satellite overpass. An average reflectance was calculated from all common angles of all ASD positions.

The distance of the target measured outward from tripod depended on the MZA. CHRIS acquisitions range ±27°. Negative MZA values correspond to target locations east of the ground track (Guanter et al. 2005). For example, in 2004, all the GWVD acquisitions had MZA values ranging from 5° to 24°. The target was always located west of the orbital ground track. The 2006 triplets were acquired in relatively symmetrical orbits above the target with MZA angles of 20°, -2° and -23°.

3.6. Data Collection

Spectral samples were collected in the field between local time of 12:00 PM to 1:30 PM. This time period was chosen to minimize the change in solar azimuth and zenith angles compared to the sun angles during CHRIS acquisitions. This field work was broken down into three phases: 1) multiple angles were measured for September 2nd acquisition with an MZA of +20° during the first 45 minutes of field work (12:00PM to 12:45PM), 2) spectral walks were made to 1:00 PM and 3) spectral angles with an MZA of -2, equivalent to the September 3rd over flight were made from 1:00 PM to 1:30 PM. No multi angle measurements were made for the equivalent of the September 4th acquisition with an MZA of -23°.

Figure 21 shows that the change in solar azimuth during field collection ranged from 151° to 186° and the sun altitude started at 46° and reached its maximum of 49.2° near the end of the field work. Also plotted in Figure 21 are the solar angles during each of the acquisitions of the triplet at their day time equivalents.

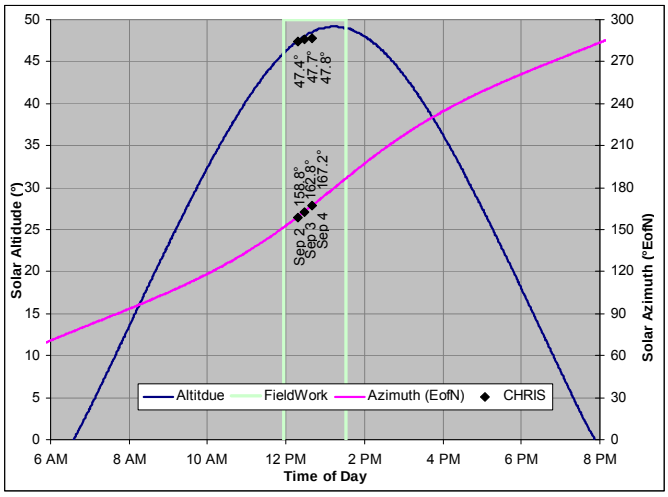

Figure 21. Solar altitude and azimuth (U.S. Naval Observatory 2006) at Farmer's Field (48° 35N, 123°38W) during field work Sept 2, 2006 and day time equivalents for the CHRIS triplet over passes.

The change in solar altitude for each scene during the triplet is minimal (all within 1°). It was during the first phase of field measurements that the satellite passed over the target (12:17 PM). On September 3 the satellite overpass was at 12:28 PM and the solar altitude during that time was 47.7°. During the field work day, the equivalent solar altitude occurred at 12:21 PM. On September 4, satellite overpass was at 12:39 PM. The solar altitude was 47.8° an equivalent altitude was reached during the field day at 12:24 PM.

The solar azimuth had a change of 35° during the field work. During satellite acquisition, the mean solar azimuths varied by 8.4° (158.8°, 162.8° and 167.2° for each of the three dates, respectively). The azimuth changed 1.4° during 3 minutes 16 seconds it took for each overpass to complete.

There was potential for shadows from the simple goniometric system to be cast over the target. For example, depending on the time of year, a relatively high positive MZA during early summer (April to June) and a FZA of -36° the sun could be aligned with the

satellite. Using the ASD's viewer on the pistol grip, notes were taken when there was shadowing on the target. There was more of a problem in attempting to get a white target reading as can be seen in Figure 22. To avoid this problem, the white target reading from the previous angle was used.

Figure 22. Potential shadowing issues.

3.6.1. ASD Instrument

Ground spectral data are collected using an ASD SRT-99-050, calibrated October 13, 2004. This instrument had been provided through the courtesy of the UVic.

3.6.2. GPS Instrument

Hand held Garmin GPS units were used to record the start and end points of the spectral walk, as well as the location of the tripod during ASD angular measurements. These points helped determine which pixels in the orthorectified CHRIS imagery correspond to spectral measurements. The positional accuracy of these instruments was within 10m, sufficient to determine which CHRIS pixels (~36 m) were within the spectral walks (See Figure 15).

3.7. Spectral Collection

Calibrated spectralon panels were measured frequently with the ASD during the field spectral collection to provide the equivalent of 100 percent reflectance. All spectra in the field are collected in radiance ($W/m^2/st/nm$). Reflectance spectra were created by dividing all radiance spectra by the most recently measured white target measurement (also in radiance). These white targets represent the ground reflectance for atmospheric conditions during data collection. During the field measurement taken on September 2nd, white target measurements were made at nadir before and after each spectral walk and during each ASD station measurement. A time stamp was also recorded with each measurement, so it was possible to determine which white target should be used with each spectrum.

Nadir readings were made at each ASD station along the reference line, first simply by holding the ASD vertically above each ASD point in sequence. This was followed by setting up the tripod as a goniometer. The first series of readings were to measure the grass target at the same angle as the CHRIS overpass, with an MZA of 20° and each of the five FZA's. This was repeated six times, moving one metre along the orbital track, providing five measurements at each of the six ASD stations. White target readings were made at the beginning of each five angles at the nadir position, and then the tripod was tilted back to the appropriate MZA position. The ground content of each target reading is approximated in Figure 23.

Figure 23. Approximate footprints of spectral readings of grass along the orbital reference line or principle plane.

It took 25 minutes to make spectral measurements over the 6 ASD stations. The ASD unit was set to take five readings per measurement to minimize the time in the field, while getting enough measurements to calculate an average reading and the variance. Five measurements were recorded per angle. Five angles were recorded at each ASD station and six stations were measured per MZA angle. Two of the three MZA were recorded.

A spectral walk of over 100 m was made holding the spectrometer in the nadir position. The beginning and end positions were recorded with the GPS to allow for the linking of the spectral walk to the orthorectified imagery. This walk was completed in less than 10 minutes.

The second set of angular measurements was taken to simulate subsequent days of CHRIS over pass with an MZA of -2°. White target, nadir and five angular spectral measurements at six ASD stations along the orbit track were all made within a 25 minute period.

3.8. Spectral Processing

The purpose of field spectral processing was to generate representative ground spectra of the calibration target at the same angles the satellite sensor viewed the same target. These spectra were then used in the calibration processes to convert the CHRIS imagery to ground reflectance.

Individual field spectra measurements were rejected if they were not consistent with what was expected. For example, a shadow from a passing colleague may pass over the target or the ASD fibre optic could slide inside the pistol grip and render the readings to be unusable. It was necessary, therefore, to validate each spectrum collected before aggregating and averaging multiple readings to create the representative spectra.

Each spectrum was converted to radiance using the ASD software and exported to ASCII files. The collection of spectra made from each angle for each target was averaged together calculating the mean, standard deviation and number of readings for each wavelength over the full range of the ASD.

Spectral plots were made of each spectral set which showed the mean radiance ± one standard deviation and the minimum and maximum value for each wavelength (see Figure 24). The secondary ordinate axis displays in gray the percent coefficient of variation of the mean to show how much variation there was from all the spectra relative to the mean. The spectral angle of each reading relative to the mean spectra of the five readings was also computed in the hopes of identifying outliers (Figure 25). The spectral angle is a measure of the spectral similarity of two spectra; an "angle" in space with dimensionality equal to the number of bands. If the maximum spectral angle is above 1 degree, then potentially one or two spectra have been corrupted. Since each of these readings were usually taken from a tripod consecutively during a short time interval, it was expected that these five spectra would be nearly identical expect for variation due to the instrument itself. Most of these combined spectra from each ASD station had less than 0.25% variation of the mean, spectral angles of < 0.15 degrees and were therefore suitable for merging. Compromised spectra were rejected from some of the samples.

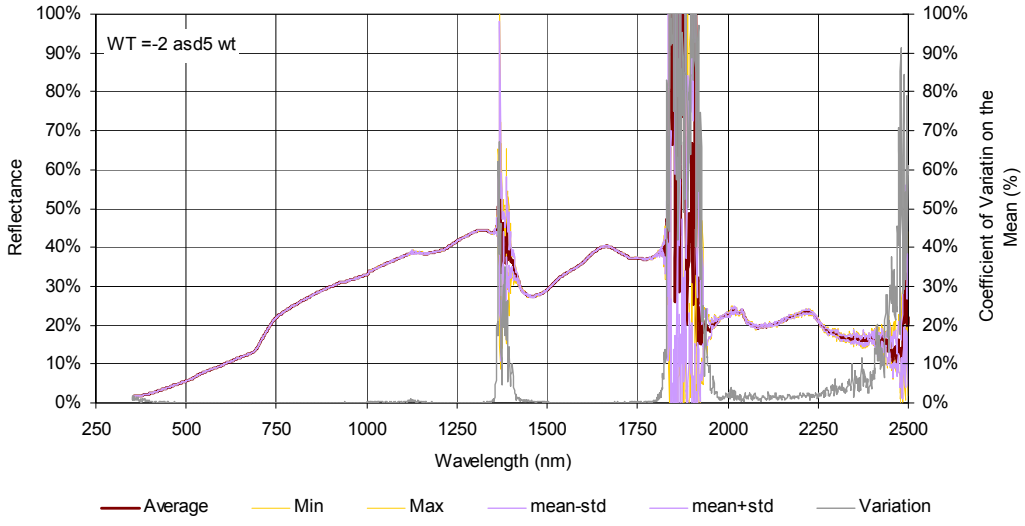

Figure 24. Example spectral plot showing full range of ASD measurements at ASD position 5 with MZA of -2 and FZA of +33.

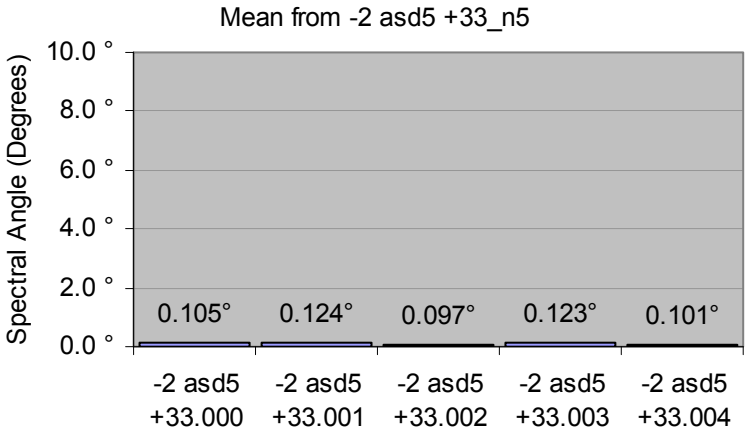

Figure 25. Example spectral angles of each sample to the mean at position ASD 5 with MZA of -2 and FZA of +33. Compromised spectra would be over 8 degrees.

The creation of the aggregate spectra for each angle included the mean spectra, the standard deviation at each wavelength and also the number of samples. As spectra were combined several times to build up the representative spectrum for the target, it was important to calculate how much variance there was in the final product. A method was developed to allow for the combination of aggregated spectra while preserving the count, mean and standard deviation of each wavelength (see Figure 26).

Given two samples taken from the same population, with counts (n_1 and n_2), means (x_1 and x_2) and standard deviations (σ_1 and σ_2), it was possible to calculate the combined count (n_{all}) (Equation 2), mean (x_{all}) (Equation 3) and standard deviation (σ_{all}) (Equation 4) (Magnussen 2006) as if they were sampled at the same time.

Equation 2. Count of samples from both populations

$$n_{all} = n_1 + n_2$$

Equation 3. Weighted Mean

$$x_{all} = (x_1 \times n_1 + x_2 \times n_2)/(n_1 + n_2)$$

Equation 4. Combined standard deviation using from both populations only *n*, *x* and *σ*.

$$\sigma_{all} = \sqrt{\frac{\left(\sigma_1^2 \times (n_1 - 1) + n_1 \times x_1^2\right) + \left(\sigma_2^2 \times (n_2 - 1) + n_2 \times x_2^2\right) - (n_1 + n_2) \times \left(\frac{(x_1 \times n_1 + x_2 \times n_2)}{(n_1 + n_2)}\right)^2}{(n_1 + n_2 - 1)}}$$

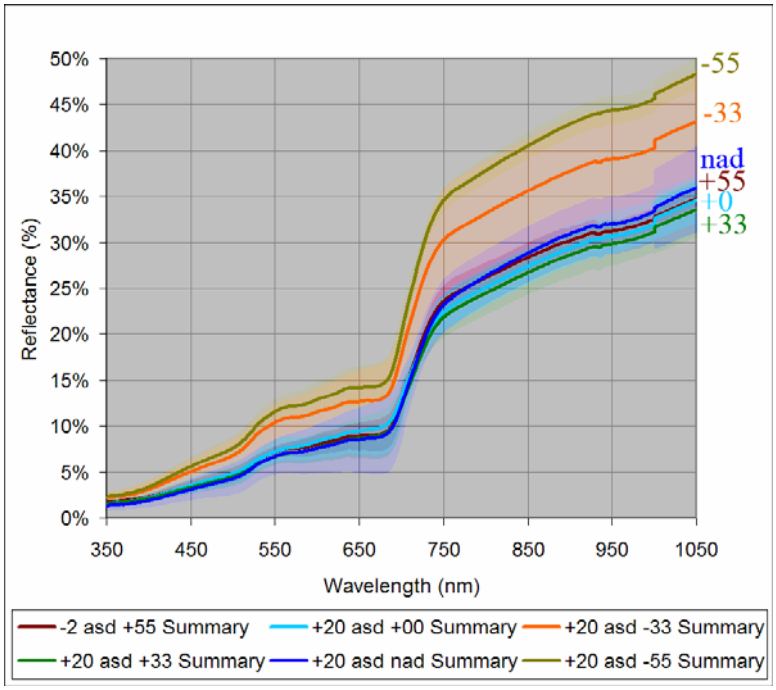

Figure 26. Mean spectra of each FZA at +20º with 1 standard deviation shown in light colour.

The spectral angle was also calculated for the mean spectra of each FZA compared to the nadir spectra (Table 4). This table shows that MZA -33º has the greatest spectral angle from nadir (3.3º), and -33º and -55º are most similar (0.32º) to each other. This can be seen by the similarity of the shapes of these lines in Figure 26.

Table 4. MZA +20º ASD VNIR Spectral Angle comparisons

	+55	+33	+00	nad	-33
+33	0.668				
+00	1.228	0.860			
nad	1.352	1.265	2.083		
-33	2.052	2.182	1.576	3.307	
-55	1.865	2.059	1.542	3.132	0.320

Spectra collected on the goniometric system were both nadir and off-nadir because of the constant MZA acquired by the CHRIS sensor. All the walk data collected were assumed to be nadir (assuming the ASD is held vertical during the spectral walks). The walk spectra can be adjusted by a Spectral Adjustment Ratio (or Simple Ratio – SR) to provide spectral ground truth for each angle collected by the CHRIS sensor. The SR is calculated by dividing the mean spectra for that angle by the mean nadir measurement. A ratio of each angle measured on the ground is found in Figure 27. These ratios are then applied to the spectral walk to provide the estimated mean ground spectra as expected from each satellite view angle.

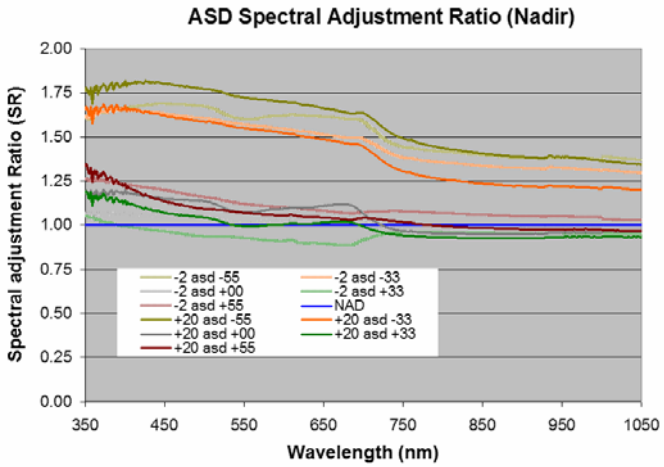

Figure 27. Dividing the mean spectra for each angle by the nadir spectra of all the targets, a Spectral Adjustment Ratio (SR) has been calculated.

3.8.1. Spectral Walks

The spectral walk consisted of over 100 m of nadir measurements of the grassy farmer's field (Red line in Figure 15). As was expected with the nature of a grassy field consisting of dried and green grass, there was variation of the spectra over the 100 m walk as can be seen in Figure 28. This walk captured a representative ground truth of nadir spectra over an area that can be identified in the imagery.

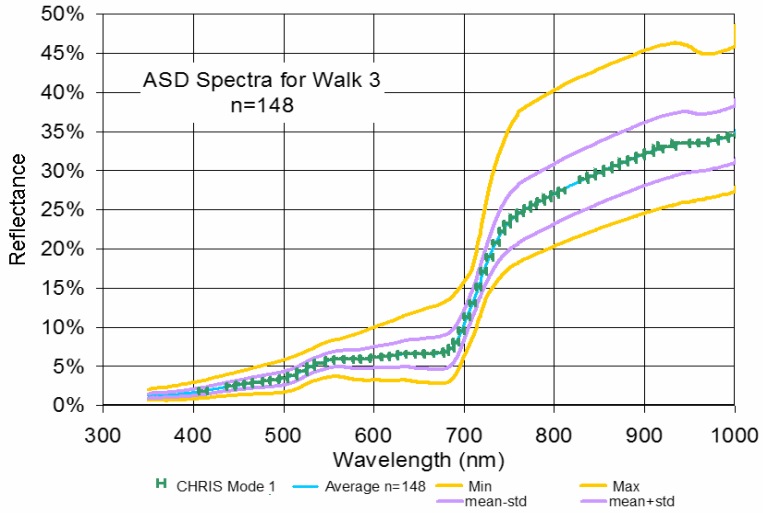

Figure 28. Mean reflectance of farmer's field taken at nadir with min, max and standard deviation. Extents of the CHRIS Mode 1 band widths are overlaid on the mean spectra.

The ground spectra collected for the spectral walk had been multiplied by the various SR. The resulting calculated spectra represent ground signatures of the farmer' field for each angle as they would be viewed from the satellite for the first two days of the over-flight. These spectra are shown in Figure 29.

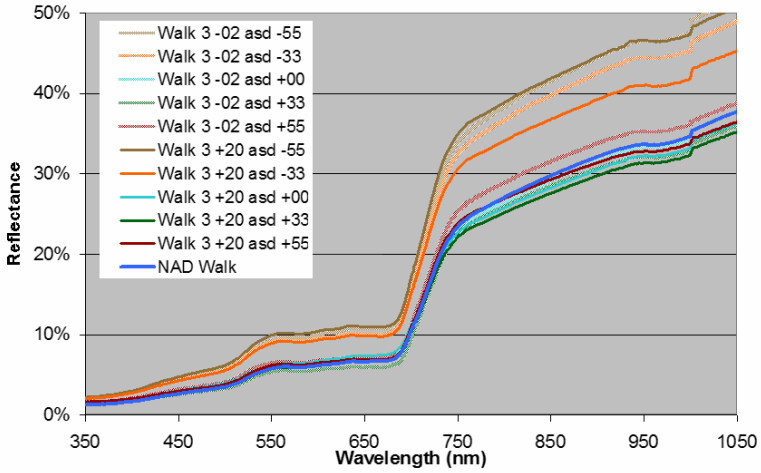

Figure 29. Multiply the Spectral Walk by the SR will provide calibration spectra for each atmospherically corrected CHRIS image containing the target area.

The next step was to process the imagery to the point of atmospheric correction and compare the spectra from the imagery over the spectral walk to the ground spectra at all viewing angles. Theoretically they should be similar to the final spectra found in Figure 29, any differences would have be due to characteristics of the atmosphere that were not completely modelled by an atmospheric correction package. These differences were then corrected by calculating a force-fit function and applied to the whole of each image.

Chapter 4. Image Processing Methods

4.1. Introduction

Launched by ESA as a technology demonstrator in 2001, the PROBA platform's versatility allowed for spectraldirectional CHRIS images to be collected over a target at five angles in a single pass. A triplet acquisition made during a three-day period in September 2006, over the Greater Victoria Watershed District (GVWD), provided the opportunity to evaluate the potential to obtain accurate forest information products with multi-angle hyperspectral imagery. Unique pre-processing challenges are discussed in this chapter. From September 2nd to 4th 2006, a triplet acquisition was acquired, providing 15 look angles in three consecutive days with MZAs of 20°, -2° and -23°.

4.2. Noise Reduction

Noise reduction of CHRIS data had already been implemented by Garcia and J.Moreno (2004). Theses corrections removed or reduced the horizontal and vertical striping. Due to the contrast of water bodies in the image, some over-correction was introduced in the vertical direction.

4.3. Geometric Correction

Ortho-rectification was required due to the high amount of relief in the GVWD study areas. 3D physical models should be the primary choice, when available, when performing ortho-rectification (Toutin and Carbonneau 1992). Previously CHRIS data was ortho-rectified using the empirical approach of Rational Function Model (RFM) with good results (Dyk et al. 2006). The CHRIS data was not provided with an orbital model that can be ingested directly by PCI's OrthoEngine, but the generic satellite import panel allowed for the specification of orbital parameters of new sensors. According to

Kneubühler et al. (2005) the use of generic orbital models in high relief areas (Swiss Alps) could provide an acceptable ortho-rectification with CHRIS data.

4.4. Viewing Geometry

Difficulties in ortho-rectifying the CHRIS data over the GVWD led to a detailed analysis of the CHRIS geometry. It was discovered that information provided in the CHRIS HDF v4.1 metadata was not totally reliable. Although not critical to ortho-rectification, the center time stamps for two images were found to be incorrect. The image acquired September 3, 2006 (7369) with an MZA of -2° and FZA of 0° had a time stamp 180 seconds too early. The image acquired on September 4, 2006 (737B) with an MZA of -23° and FZA of +55° had a time stamp 49 seconds too late, making it the same as the next image with an FZA of +36°.

Google Earth® is a useful tool to visualize and verify the 3D orbit models of CHRIS acquisitions. A tool was developed to convert the given orbital information provided by the HDF files to Google Earth KML format. This process involved converting the target position, OZA and OAA, to Tilt and Heading, and also calculating the ground position in latitude and longitude of each acquisition point. The end result allowed the user to visualize the orbital positions of CHRIS in a 3D viewing environment (see Figure 30).

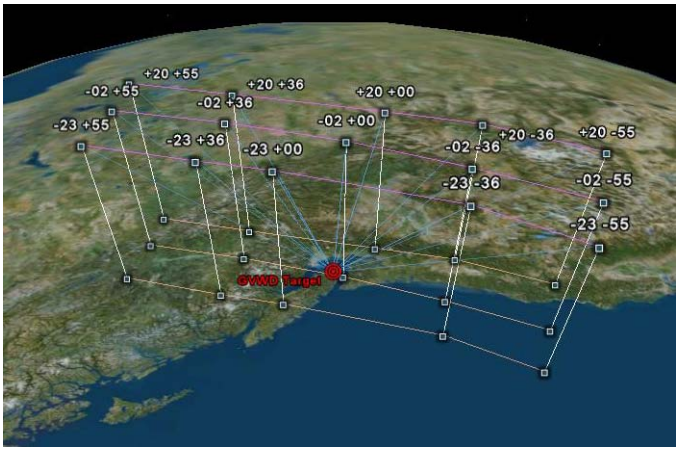

Figure 30. 3D View of the CHRIS geometry during triplet overpass of GVWD looking east using Google Earth®. Overlay image used by permission ©2007 Worldsat International Inc.

The calculated Orbital Zenith and Azimuth Angles (OZA and OAA) appeared to be incorrect in the HDF 4.1 metadata for orbits when FZA is 0° and the MZA are not near 0°. One can see in Figure 34 that the positions of the satellite at the middle FZA are not evenly distributed on the outside orbits. This can also be seen in the 3D representation of the MZA +20° orbit in Figure 31. The red lines show how FZA and MZA are calculated. If the time interval of each acquisition was 49 seconds, as defined by the meta-data, then the position of FZA of 0° should have been over-top of the SSMA. There was a ground track difference of 100 km between the SSMA and the satellite position for FZA of 0° and MZA of +20°.

Also based on the meta-data satellite position, the orbits did not appear to line up (see Figure 34). The last satellite position (FZA of -55°) in MZA +20° seemed to veer to the west and the first satellite position (FZA of -55°) in MZA of -23° was too far east.

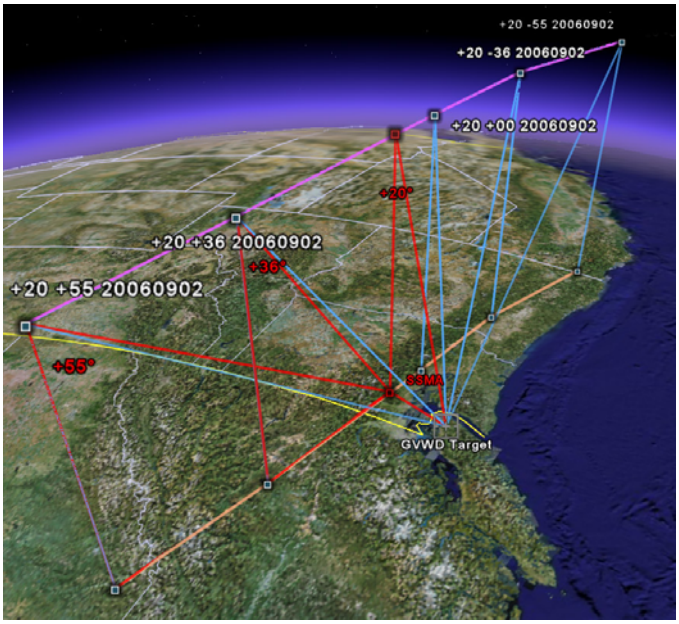

Figure 31. Sample view of CHRIS geometry during overpass of GVWD, looking southeast. Red lines show geometry of FZA (+55° and +36°) and MZA (+20°) relative to SSMA and target. Blue lines show the satellite's view to the target. Satellite positions in orbit are based on geometry extracted from HDF 4.1 files (Note position of +20 +00 is too far along track). Overlay image used by permission ©2007 Worldsat International Inc.

4.5. Ortho-rectification

GCPs were carefully selected using ortho-rectified Landsat image, water body vectors and a 25 m DEM using a method developed for Dyk et al. (2002). This DEM was within the grid spacing for extreme off-nadir angles as suggested by Toutin (2004). An output pixel size of 36 m was selected to represent the finest spatial resolution from CHRIS mode 1 data. Within PCI's OrthoEngine, orbital segments, GCPs, tie points and bundle adjustments were used to ensure a good fit between all the images in a single overpass.

A physical satellite model mathematically describes the distortions of the platform (position, attitude, and velocity), the sensor (IFOV, panoramic distortions), the Earth (rotation, curvature and topographic relief) and the map projection (geoid approximation and projection). The required inputs to the model were orbital and sensor information,

and ground control points (GCPs), with elevations which were used to compute and refine the parameters of the model (Toutin 2004).

PCI's generic orbital model required the following input information: sensor altitude, orbital period, eccentricity, actual inclination, sensor across-track and along-track angle and IFOV. The across-track and along-track angles were not critical (Cheng 2007), as these parameters could be estimated from the GCPs. Scene related inputs were: pixel spacing at nadir, the approximate scene center, as well as the underlying ellipsoid and a digital elevation or surface model. These inputs were extracted from the HDF header. The two-line orbital elements (TLE) formatted meta-data is summarized in the Table 5.

Table 5. Input parameters into orthoengine's generic image panel

Sensor Name: "*New-Sensor*" Satellite: "*CHRIS/Proba*"
Across track angle: ***0*** Along track angle: ***0*** (Estimated from GCPs) IFOV: *0.0000597* (Calculated from Barnsley et al. (2004)) Altitude: *550000* m (From .hdf "Platform Altitude" x 1000) Period: *96.69* min (From TLE: (24*60)/14.89346273 mean motion)
Actual Eccentricity: *0.0082774* (From TLE) Orbit Inclination: *97.7426* (From TLE)
Pixel(X): *34* m (Nominal for mode 1 at perigee (Kneubühler et al. 2005)) Line (Y): *34* m Longitude: *-123.67* (as from .hdf "Target Longitude") Latitude: *48.59* (as from .hdf "Target Latitude") Ellipsoid: *E012* (WGS-84 from Sira's CHRIS FORMAT Handbook (Cutter 2005))

The resulting correction had an RMS error of over two pixels, so further correction was required to reduce the misalignment. Overlaying each of the view angles with the lakes vector confirmed that the RMS error was valid. To align the images further required that the GCPs on the ortho-rectified images be redefined and an additional tie point over each of the sample plots was added. The empirical thin-plate spline model was applied to the ortho-rectified images to provide a sub-pixel aligned image set. More research is required

to explain why the generic orbital model failed to provide a sub-pixel accuracy image set in one step.

Due to the pointing errors of the PROBA sensor, only a small subset of the study area was imaged at all angles, two of the fifteen images did not include the calibration target, a farmer's field. Analysis was limited to images that had the ground calibration target included.

Chapter 5. Spectral Processing Methods

5.1. Introduction

High spectral, spatial and directional resolution imagery from CHRIS, were used to retrieve forest structural parameters over the GVWD. This required an understanding of the anisotropic nature of forest canopies as measured by space borne hyperspectral sensors, and modeled by radiative transfer models, such as 5-Scale (Leblanc et al. 1999). The imagery was required to be atmospherically corrected to ground reflectance, in order to be directly comparable to modeled reflectance from 5-Scale.

5.2. CHRIS Atmospheric Correction

This section describes the next step of processing CHRIS data to the point of atmospheric correction, and compares the spectra from the imagery over the spectral walk to the ground spectra at all viewing angles. An atmospheric correction of optical space borne imagery is the extraction of earth surface reflectance by modeling the influence of the atmosphere, solar illumination, sensor viewing geometry, and terrain information.

The final spectra derived from the ground spectral field collection, as found in Figure 32, should match that measured in the imagery. Any differences would be due to characteristics of the atmosphere that were not completely modelled by an atmospheric correction package. The differences between the modeled and ground validation spectra were then corrected by calculating a force-fit function and applied to the whole of each image (Goodenough 2003).

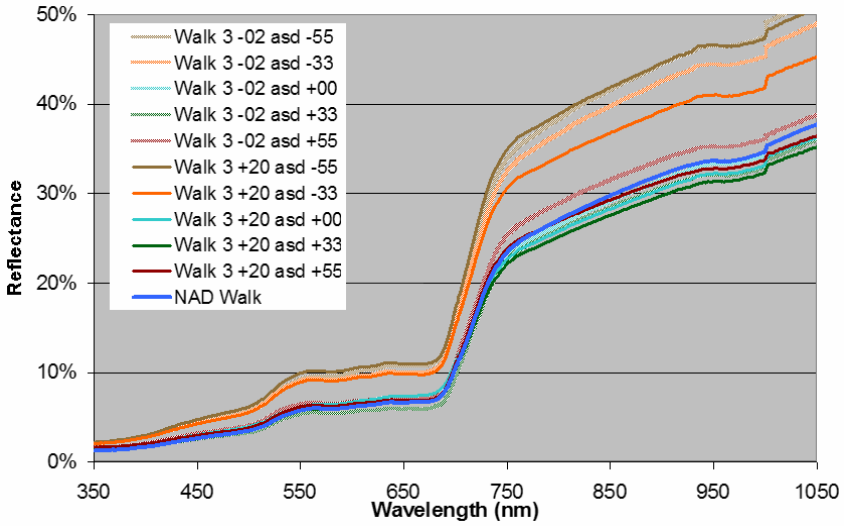

Figure 32. Multiply the Spectral Walk by the simple ratio (SR) will provide calibration spectra for each atmospherically corrected CHRIS image containing the grassy target area.

The atmospheric correction package ATCOR was selected to perform the atmospheric and topographic correction of the 2006 CHRIS data set. The satellite modules of ATCOR (ATCOR-2/3) supported small to moderate FOV sensors and consists of separate codes for flat and rugged terrain (Richter 2007). It utilized an atmospheric correction look-up-table computed with the MODTRAN 4 radiative transfer code, covering a wide range of weather conditions, sun angles, sensor angles and ground elevations. ATCOR had built into its design the ability to process CHRIS's off nadir imagery and to account for topography.

The methodology of collecting spectral calibration data in the field, with the intent of calibrating multi-angle CHRIS data to nadir normalized reflectance follows. Since there are 15 images at various angles, the calibration of these images required the spectral collection of a homogeneous target on the ground, at the same angles as CHRIS. Two overpass angles with MZAs of +20° and -2° were collected in the field during the first overpass. Ground spectra measured at the third angle (MZA of -23°) was unavailable.

The ground spectra for the first two overpasses were then used to calibrate reflectance spectra made from an atmospheric modeling program (ATCOR-3) as suggested by Kneubühler et al. (2005) in which CHRIS imagery was atmospherically corrected in rugged terrain.

Previous attempts to atmospherically correct off-nadir images from CHRIS were not successful. This failure can be accounted for because another atmospheric correction package (FLAASH (Research Systems Inc 2004)) was used. This atmospheric model was unable to properly handle off-nadir imagery and account for topographic relief. The MODE 4 CHRIS imagery also lacked water features, and no off-nadir ground spectra were collected (Dyk et al. 2006).

The data acquired for the GVWD in 2006 by CHRIS were in MODE 1, the full hyperspectral mode, at a 34 m resolution in the along-track direction and at an approximately 36 m to 55 m resolution in the across-track direction (depending on the FZA). Acquisitions in a continuous hyperspectral mode (400-1000 nm) captured the water vapour features at 940 nm. A large, flat, relatively homogeneous grass target suitable for calibration measurements was used to collect sample ground spectra. The objective of acquiring multi-angle ground spectra was to develop a function between off-nadir spectra to nadir spectra. This function was then applied to the spectral walks to provide the equivalent off-nadir ground calibration over a large area.

5.3. ATCOR-3 Processing Steps

In order to prepare the CHRIS data for atmospheric correction, the following processing steps were performed. A DEM was used to create topographic inputs required for ATCOR-3. A DEM file is required to match to the size of each input image. From the

DEM, slope and aspect are derived. A “skyview” and “cast shadows” data sets were created as the study area contains extremely steep terrain. These files were generated for the whole study region using ATCOR-3’s built-in functionality, and then clipped out to give the same extents of each view angle. The elevation file contains the height of land at each pixel stored as 16 byte integer in one meter increments. The range of the DEM for this area is 32-845 m. Aspect is stored in one degree increments from 0 to 360 as a 16 bit integer. Slope values are stored in a single byte with a range of 0 to 45° in 1° increments.

The initial input DEM was a 25 m DEM gridded from BC’s Terrain Resource Inventory Mapping (TRIM) data cropped to the extents of the common area of all CHRIS images used in the study (see Figure 33). This data set was resampled to 36 m to represent the finest spatial resolution from CHRIS mode 1 data. The origin of the 36 m UTM grid was kept to be a mode of the pixel size to ensure the DEM lines up with the orthorectified CHRIS imagery. Both slope and aspect were calculated using 108 m (3×3 pixels) area around each pixel. The sky view factor image is calculated with ray tracing to indicate a percentage of a full hemispherical view coded as a byte. A zenith or illumination image was generated with the sun simulated at the same angle as that during acquisition, zenith of 48° and azimuth of 163°. This image simulated shadows on the terrain to aid in the inspection of DEM artifacts.

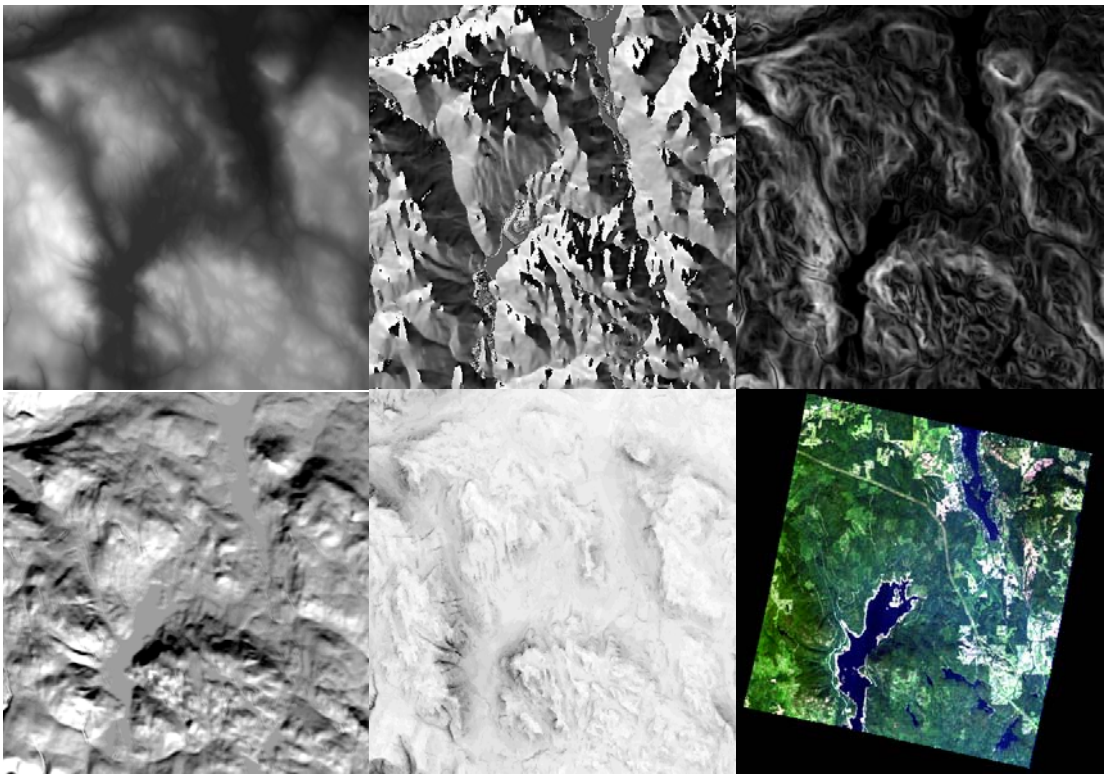

Figure 33. Input representations of the DEM for 0903_A+00. Upper left - elevation ranging from 32 to 845m, upper centre - Aspect 0-360°, upper right - Slope 0-90°, lower left - Illumination from same sun angle as Sept 3rd imagery, lower centre - Sky View 62-100% and the input CHRIS image acquired Sept. 03, 2006 at nadir (A+00) true colour.

The input image used was the output from the ortho-rectification process in radiance ($W/m^2/sr/\mu m$). The image acquisition date was required. The scale factor outputs the results as percentage * 10 and was stored in a 2-byte format with 1 decimal of significance. Sensor viewing geometry includes the tilt and view azimuth angles relative to north. These angles have been calculated from the meta-data. The sensor type is CHRIS MODE 1, in which the spectral definitions are stored in a calibration file called "chris_mode1.cal" as provided by ATCOR. Pixel size is set to 36 m, as output from the orthorectification. The atmospheric file used is called "`h99000_wv10_rural.atm`" which represents a file with the symbolic altitude of 99,000 m, water vapour column 1.0 cm,

and the rural aerosol. There are MODTRAN lookup tables pre-generated to simulate an atmosphere up to a satellite altitude, water vapour column of 2.0 g/cm² with a rural aerosol type. The adjacency range is 1 km. Visibility is very clear at 30 km. The solar Zenith angle was calculated to be 47.4° and 47.7° and an azimuth of 158.8° and 163.0° at time of the September 2nd and 3nd, 2006 acquisition, respectively (see sun position in Figure 34).

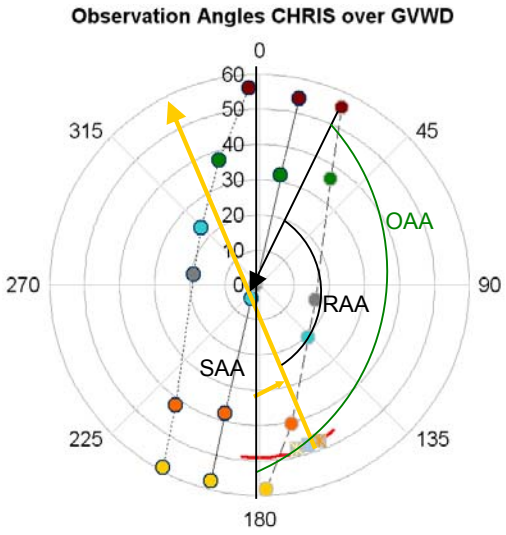

Figure 34. Polar plot of satellite and sun position during acquisitions as acquired from meta data in header HDF v 4.1. Colours relate to FZA, grey dots represent estimation of minimum approach angle. Viewing Zenith Angle = (OZA) Relative Azimuth Angle RAA = SAA-OAA, Solar Zenith Angle = (SZA); haze visible in some images.

ATCOR's water vapour algorithm used the 940 nm region available in the CHRIS Mode 1 data set. To estimate the 940 nm water vapour region, ATCOR used two bands (882.4 - channel 51) and 995 (1003.7 - Channel 62) surrounding 940 nm (943.7 – Band 57). The water vapour images created for September 2nd and 3rd, 2006 images are seen in Figure 35. The distribution pattern of water vapour appears to be consistent between all the image angles. Areas of higher water vapour appear to correspond to areas of lower elevation such as valleys.

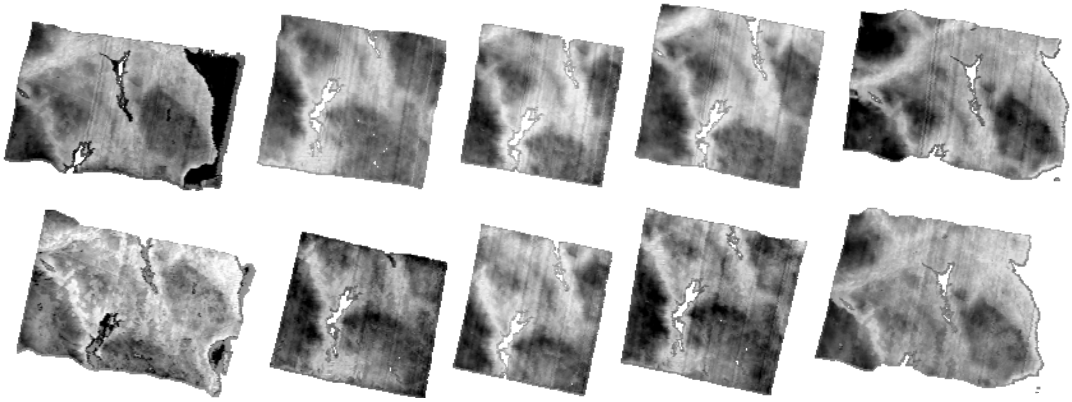

Figure 35. Water vapour images generated by ATCOR-3 for top row September 2, 2006 images and September 3, 2006 bottom row. Images from left to right are +55°, +36°,+0°,-36°,-55°. Gray scale levels range represents a water vapour column of ~7.4 to 1.1 cm. Continuous areas are masked out as they contain water bodies or no-data.

5.4. Atmospheric Correction Results

The resulting atmospherically corrected images produced by ATCOR-3 rugged terrain module contained a high number of erroneous values (outside the realm of reflectance). It was necessary to run the model in smooth terrain mode in order to get acceptable results.

5.5. Radiative Transfer Model

A radiative transfer model simulates radiation transfer processes in certain media, such as vegetation and atmosphere. For vegetation, it computes the interaction between solar radiation and plants. Structural information that can be derived from multi-angle remote sensing includes vegetation cover, gap fraction, plant dimensions, leaf orientation and LAI (Asner 2000). These models are useful when inverted to estimate the forest structural parameters based on the observed reflectance of multi-angle hyperspectral imagery. Forest sites representing various forest parameters were identified using a combination of forest cover maps, field data and LIDAR acquisitions.

5-scale is geometric-optical model, emphasizing the importance of canopy architecture and multiple-scattering scheme in simulations of canopy reflectance. Incorporating the

canopy architecture, leaf, shoots and branch distributions used to model the transmission of solar light through the canopy, 5 Scale is a combination of 4 Scale by Chen and Leblanc (1997) and LIBERTY by Dawson et al. (1998). Measured leaf and background spectra were used as an input to replace the LIBERTY component. The output files include probabilities (percentages/fractions) of viewing the four components (foliage and background sunlit, and foliage and background shaded areas) and their reflectance, as well as total canopy reflectance for each band.

Due to unavailability of the full foliage spectral data (reflectance and transmittance) from the GVWD, field data for the nearby region were provided by the University of Toronto. They encompassed ASD measurements of foliage spectra of old Douglas-fir forest within the same eco-region and it was assumed that they did not differ significantly in respect to Douglas-fir forest structure. Salal was used as the dominant under-story for the plots. Input Salal spectra were acquired using an ASD. The main forest stand parameters to run the model included: tree height (H), Stand Density (D), Crown Radius (r), and LAI. LIDAR acquisitions and ground field plots were provided by UVic to help estimate stem density, and tree height.

On July 27, 2006, airborne LIDAR data were collected by UVic's Department of Geography throughout the GVWD study area. UVic calculated tree top locations using a local maxima algorithm by processing the LIDAR data into a 1m canopy height model (Loos and Niemann 2006). They were then able to provide individual tree locations with heights over the study area. LIDAR based canopy attributes were extracted from each of the EVEOSD plots (Goodenough 2003) (see Table 6 and Figure 36).

Table 6. Plot parameters used for 5-scale.

Plot No	Stems per ha	$Height_{tt}$ (mean)	Crown Radius	LAI_{UofT} (m^2m^2)	Plot No	Stems per ha	$Height_{tt}$ (mean)	Crown Radius	LAI_{UofT} (m^2m^2)
4	169.8	25.4	2.6	5.03	20	254.6	13.7	2.7	5.19
6	300.9	16.4	2.5	6.53	22	200.6	29.1	3.9	7.28
7	416.7	26.6	2.1	6.58	25	192.9	27.1	3.5	5.94
8	177.5	41.2	4	7.92	26	293.2	19.8	3.7	6.06
14	393.5	15.1	1.7	7.09	28	169.8	24.4	4.3	6.23
15	115.7	45.5	4.1	5.66	29	185.2	30.5	3.7	1.85
16	293.2	26.7	2.6	10.04	30	177.5	21.4	4	3.76
17	108	37.6	3.7	6	53	192.9	43.5	4.5	6.18
18	285.5	26.8	2.2	6.88	54	216	26.3	3.4	3.01
19	393.5	12.4	1.9	1.27					

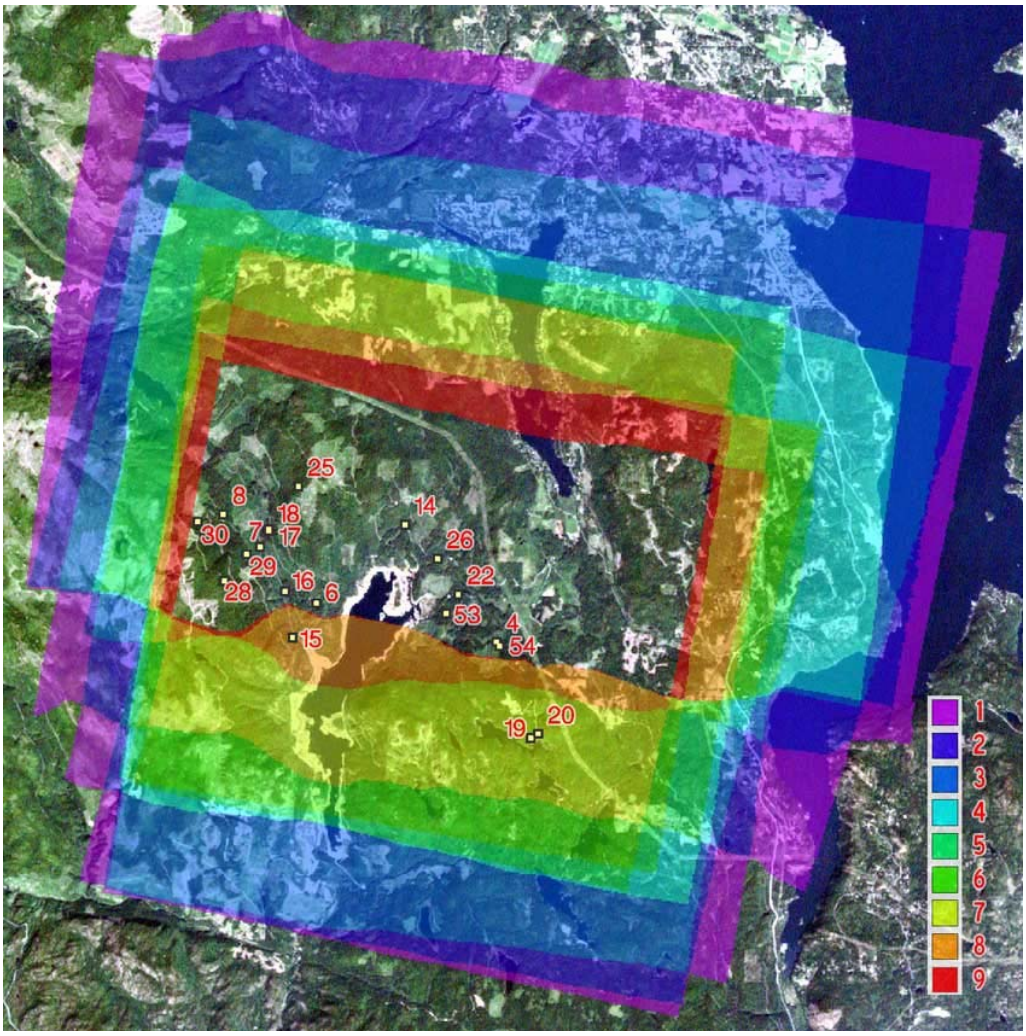

Figure 36. Common area of CHRIS images acquired September 2nd and 3rd, 2006 over the GVWD. Colors represent number of scenes overlapping: center clear image portion has 10 scenes that overlap, magenta area has 9 scenes, red has 8, orange has 7, etc…

The height required for 5-scale is composed of three parameters, the stick height (H_a), cylinder height (H_b) and apex height (H_c) (see Figure 37). In developing crown ratio models, Temesgen et al. (2005) surveyed Douglas-fir trees in southeastern British Columbia. The mean crown ratio found was 52% (+/-19%). This value was also within range from plot measurements made by CFS and UVic. Initially H_a was therefore set to 48% of the total tree height. H_c cannot be directly input into the model; however, it is a function of the Apex Angle (α) and the Crown Radius (r). H_b is the remainder of height measured with LIDAR minus the H_a and H_c.

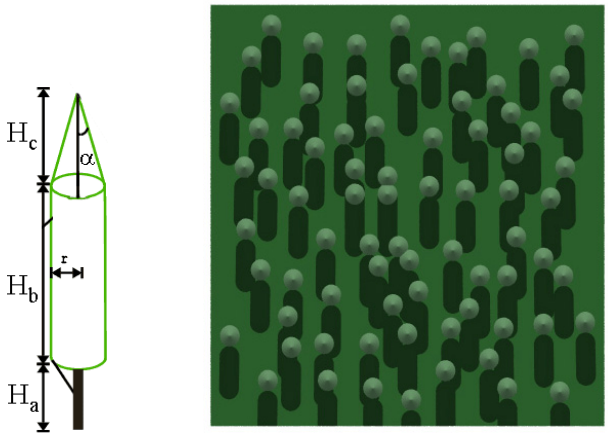

Figure 37. Tree height parameters used in 5-Scale (left), Nadir view of sparse forest using cones, cylinders and sticks. (images modified from Leblanc et al. (1999)). Note the large portion of ground visible from this position.

LAI measurements where made with the Li-COR 2000 during the summer of 2002 at many of the EVEOSD plots by UVic. These raw data were then processed by Jing Chen at the University of Toronto (U of T) with the intent of using these measurements with the 5-Scale RTM model.

Ancillary data sets included 20 cm ortho-photography and forest cover polygons that were provided by the Capital Regional District (CRD) of Victoria who manages the

watershed. The ortho-rectified 2007 scanned RGB images provided a clear source for visualizing the plots. It was noted that not all of the aerial photos were viewed from true nadir, and therefore the trees can appear to lean away from the principle point of the images used to generate the mosaic. Also extensive field data had been collected at various plots in the region by CFS and UVic that measured various tree parameters suitable for calibrating inputs for the 5-Scale model.

Crown radius was calculated by drawing circles around a sample of trees seen in the 20 cm ortho-photography for each plot (see Figure 38). The mean radius was then used for that plot. These radius values were compared to the sample of field data collected by UVic; they are in the correct range for the tree with similar heights.

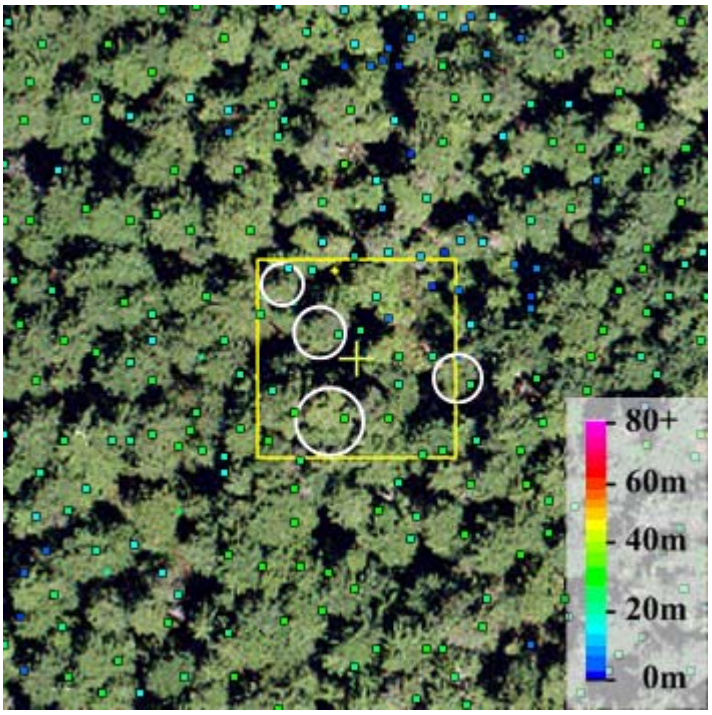

Figure 38. Crown Radius (r) was measured from 20 cm ortho-photos and averaged for each plot. LIDAR tree top overlaid to give average tree height per plot.

The stem density estimated by the LIDAR Tree Top method appeared to be low. A visual estimate of the tree tops from the 20 cm ortho-photos estimated there was 15% under estimation with the LIDAR method.

5.6. Initial Comparison of CHRIS with 5-Scale

The 5-scale model produced what appears to be an over estimation of the ground component, both shadowed and sunlit (see middle bar of charts in Figure 39). Plot 53 is a highly dense plot, the model suggest 30% ground cover is visible from nadir. Plot 20 is modeled at 40% and plot 6 is modeled to be 70% ground cover at nadir. Viewing the ortho-photos it appears that there is an over estimation of the ground portion for many of the plots. (This over estimation has also been quantified below in Figure 41). Having confidence in the input forest parameters, it was concluded that input parameters for the 5-Scale model needed to be calibrated to take into account the abundance of sub-dominant layers in the forest. The geometric model uses a Neyman distribution model to provide clumping of the stems, but assumes all trees have the same height and other forest parameters.

The spectra predicted from 5-scale were compared to the extracted spectra from two dates of CHRIS atmospherically corrected images for all the plots (see Figure 40). For the two dates of CHRIS imagery, Sept 2nd and 3rd, the extreme angled images +55° are significantly brighter than predicted by either 5-Scale or a measured in the field spectra (see Figure 26). These images are close to the dark spot. It appears the atmospheric correction process failed to correct for haze found in these images.

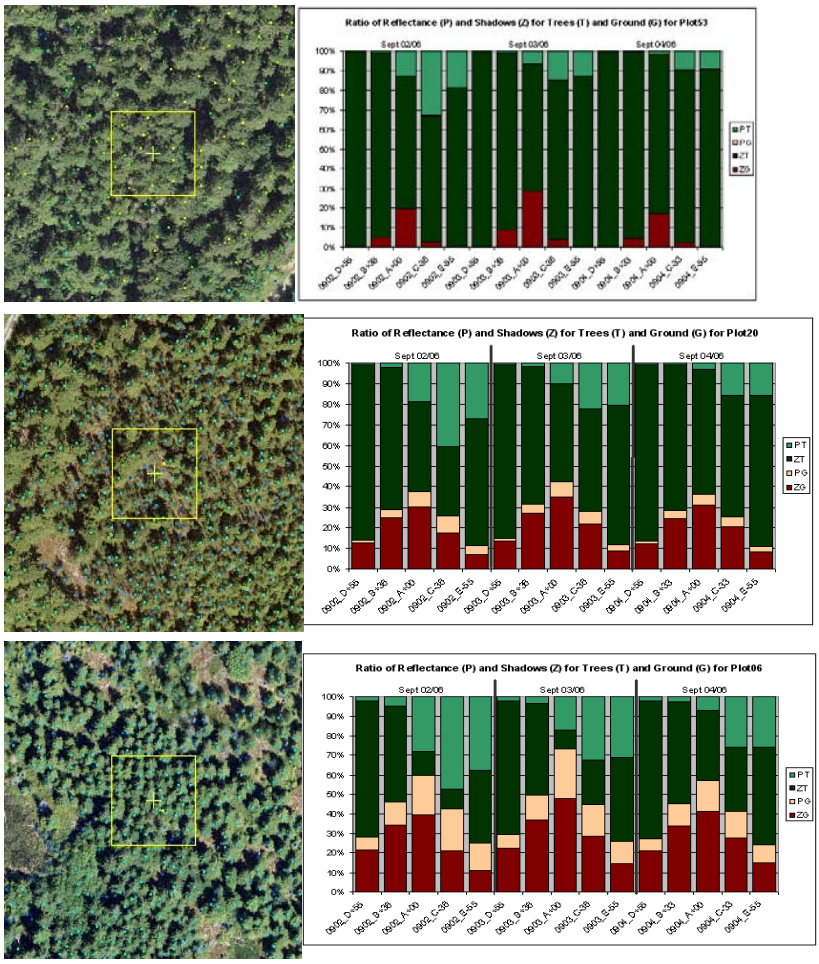

Figure 39. Sample plots showing range of forest type, top to bottom: Plot 53, 20 and 06. Left shows ortho photo of approximately nadir view with LIDAR tree tops coloured by height and yellow box showing a CHRIS pixel, right shows canopy (T) and ground (G), sunlit (P) and shadowed (Z) proportions of all 15 CHRIS angles as modelled by 5-Scale.

The remaining spectra for the plots show similar trends to 5-Scale's predicted spectra from multiple angles. The overall magnitude of the CHRIS spectra was slightly higher than that predicted. This may be due to two possible reasons: 1) the atmospheric residual in the CHRIS correction or 2) 5-scale not correctly modelling the multi-level canopy or its assumption of an isotropic background reflectance.

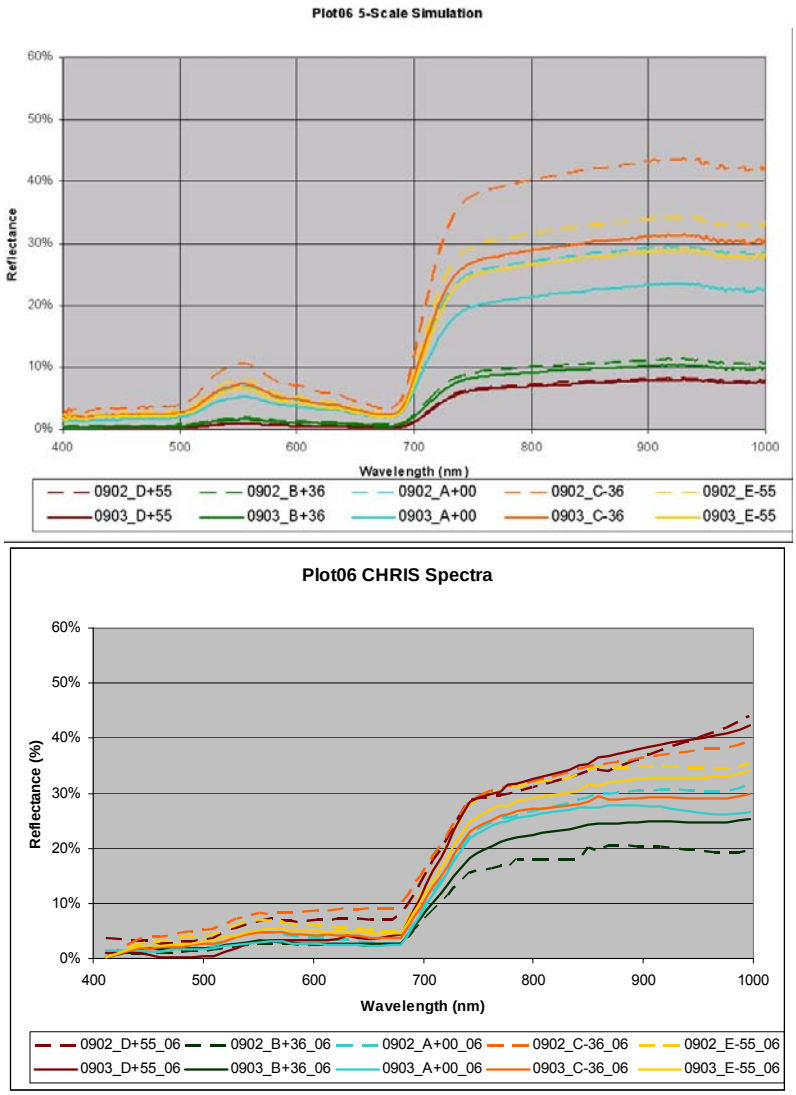

Figure 40. Sample spectra for 10 angles of CHRIS data as simulated by 5-Scale (left) and as extracted from CHRIS data for Plot 6. Note +55 degrees for either date should appear dark in the infrared (over 700 nm) according to 5-Scale, yet they appear as very bright in the CHRIS imagery.

5.7. Validating 5-Scale Parameters using LIDAR Biometrics

The relatively poor similarity of spectra produced by 5-Scale compared to the spectra extracted from CHRIS may be due to several factors, including background, atmospheric correction of the imagery, and the forest parameters used to drive the 5-Scale model.

Various LIDAR forest biometrics have been produced by UVic from a data set acquired over the watershed in the summer of 2006. Using the raw LIDAR points various biometrics are summarized at a 20m and 40m cell size. These biometrics include Rugosity, Mode, Gap, and Mean. They also included Co-Variance, Skewness, Kurtosis using four methods, Moments (M), quantile based on octiles (Q), L-Moments (L) and LQ-Moments LQ. Also two images with canopy height quantiles (LQH) and canopy density file (CCF) are also generated, providing for every percentile of LIDAR hits above 2m, the canopy height and canopy closure fraction respectively.

These data were utilized to improve the canopy structure estimates to be used as input into 5-Scale. These include gap fraction, height, height to live crown, and apex.

5.8. Compare Gap Fraction of LIDAR to 5-Scale Computation

5-Scale produced an estimate of the canopy gap fraction by simply summing up the ground shadow and sunlight components for the nadir situation of the model run. Nadir view occurs in the simulation on the September 3rd image with a FZA of 0 degrees or the column labelled 0903_A+00 found in the middle of the bar-graphs found in Figure 39.

LIDAR Biometrics have been produced by the University of Victoria from LIDAR data. The Biometric gap fraction is calculated as shown in Equation 5.

Equation 5. Calculation of biometric Gap from LIDAR point data

$$Gap_{LIDAR} = 1 - (num\ Points / All\ Points);$$

where “num Points” represents the number of points above the threshold set by the user (e.g. 2 m). A 40 m grid cell was used for the biometric calculations from the LIDAR point cloud. This information was also captured in the CCF file. Channel 1 represents the Canopy Closure fraction from 2 m above forest floor, so the gap fraction is the complement (see Equation 6).

Equation 6. The Biometric Gap is a complement of the Canopy Closure Fraction

$$Gap_{LIDAR} = 100 - CCF_1$$

The 40m grid cell of LIDAR most closely corresponding to each 36m CHRIS plot was used to compare the plot forest gap. The results are shown in Figure 41. There was no relationship between these two estimates. The range of gap fractions from LIDAR were within 3 to 33%, a reasonable range as can be observed visually from the aerial photos found in Figure 39. The 5-Scale range was very large from 25 to 77%. This evidence showed that 5-Scale did not capture the secondary forestry cover and overestimated the ground cover spectral components by at least a factor of 2.

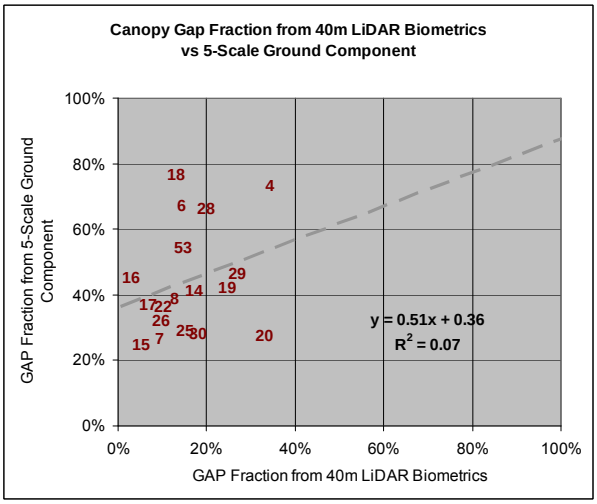

Figure 41. Canopy Gap Fraction as estimated from LIDAR at 40m cell and 5-Scale.

5-Scale would need the input parameters adjusted by either doubling the stem density or increasing the tree's diameter to double their area. A direct estimate of the shadow and sunlight components was made using the LIDAR information, but the 5-Scale model was not set up to allow for such inputs. The alternative approach was to redo the forest input parameters using the LIDAR biometrics.

5.8.1. Other revisions

5-Scale parameters that required adjustment from their defaults also included “pixel size” (1 ha) (B) and Number of Stems (D). The parameter B was set to 1 ha, but it was realized that with trees the size of the Douglas-fir in the watershed, that it wouldn’t be enough room to emulate 30 clumpings (n) within a 1 ha pixel. So the area was doubled to 2 ha (B = 20000) and the number of stems doubled to reflect the number of stems per 2 ha and the number of clumps further reduced to 15 from 30 to accommodate the simulation.

It was still necessary to reduce the amount of ground showing after the forest plot parameters had been validated/updated using the LIDAR biometrics. Since the model did not account for the secondary storey, it was necessary to increase the stem density and possibly the crown radius, until the 5-Scale gap fraction (ground portion of shade and sunlight) was within the range of LIDAR biometrics’ gap fraction.

An intensive study of trying to vary the measured inputs to 5-Scale to try to provide a realistic gap fraction did not provide adequate results. Simulations included of doubling the stem density, crown closure and both these parameters. The study failed to have 5-Scale provide gap fractions that approximated the field measurements.

This experiment is illustrated in Figure 42 showing the nadir simulation of plot 14 using a 2 ha area as simulated in 5-Scale. Simulation “A” used the measured forest parameters of stem density and crown radius as measured from the LIDAR Biometrics. This showed how the “pencil-like” modeled trees appear as circles with a “random” distribution. The random distribution does not account for the clumping that the 5-Scale model produced using the Neyman distribution, however it is an adequate simulation for this experiment. The gap fraction as modeled by 5 Scale was 67%, where as the LIDAR

biometrics had a gap fraction of only 18%. The LIDAR gap fraction appears more realistic as can be seen in the ortho and canopy hemispherical photos also in Figure 42. The gap estimate noted on the four simulations (A-D) in Figure 42 are the gap fraction remaining after summing the area of all the circles. Negative values are due to the overlap area being greater than the exposed ground area. As can be seen in simulations C and D of Plot 14, the negative gap show that the areas of all the circles were greater than the 2 ha input plot area. The area of all the crowns used in simulation D had two times more area than plot area, yet the gap fraction calculated in 5-Scale was 28%. This amount of discrepancy showed that even by adjusting the input parameters for 5-Scale, it was not possible to sufficiently reduce the predicted gap fraction to a real amount.

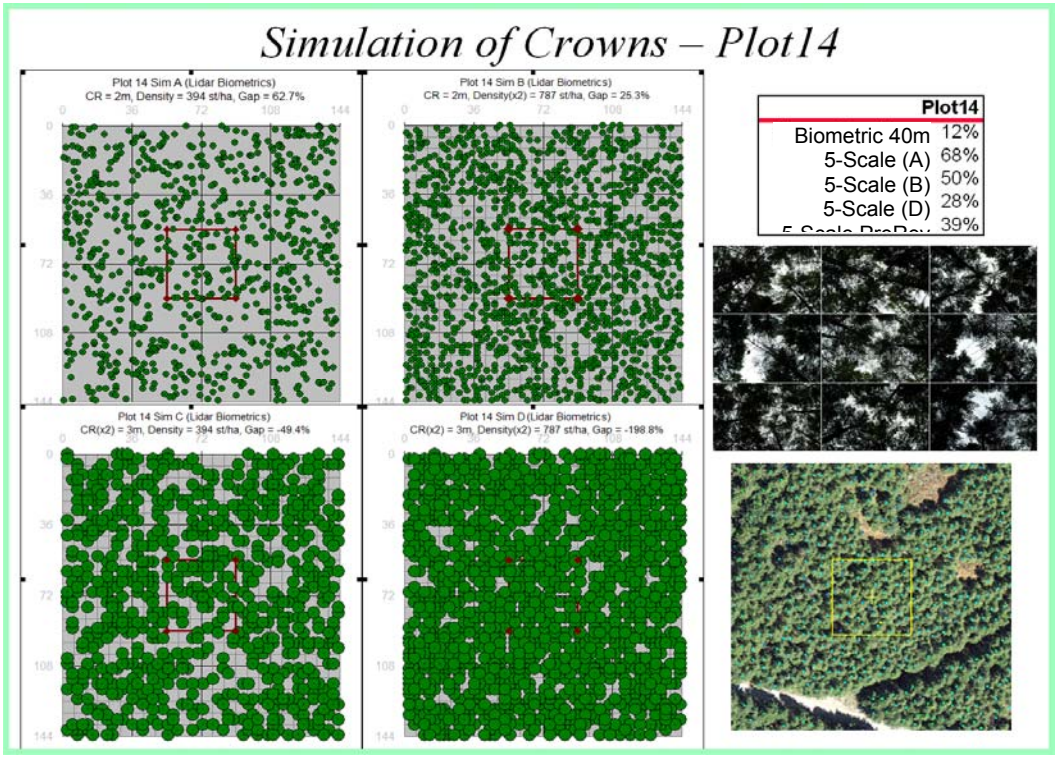

Figure 42. Simulation of plot 14 from nadir perspective. Simulation A, using original measured forest parameters, B – Doubling stem density, C – Doubling Crown Radius and D – Doubling both radius and density. Ortho photo view and under canopy views are also shown. Plots simulation are 2 ha, red box represents 36m CHRIS pixel.

Figure 43 show the result of doubling of the stem density, radius and doubling both. It was expected that the predicted ground portion would make a relationship with a slope closer to a value of one when compared to Figure 41. However this did not occur; meaning it was necessary to take an approach other than trying to modify the input parameters to improve the model's output.

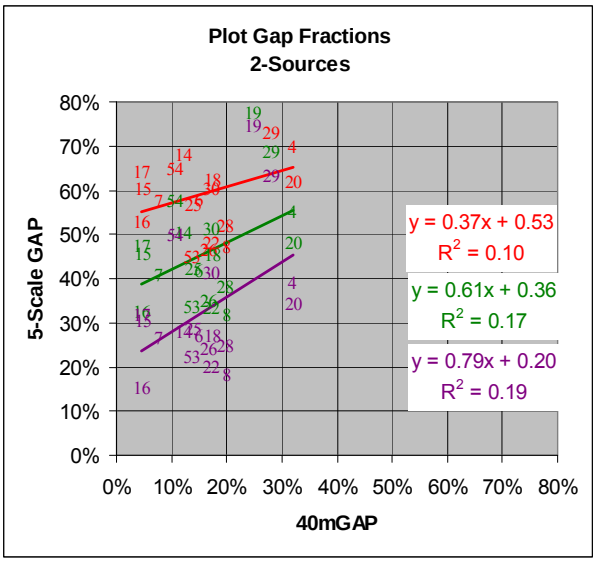

Figure 43. Canopy gap fraction changes as modeled by 5-Scale with changing density and radius compared to 40 m LIDAR Biometrics. Red - measured forest parameters, Green - Doubling Crown Radius and Purple - Doubling both radius and density

5.9. Spectral Background Adjustment

An alternative method to realistically adjust the gap fraction and represent the secondary story in the 5-Scale model was to replace the Salal spectra that represent the ground cover with a mix of Douglas-fir and Salal spectra. The understory's spectra contribution was based on the amount of gap fraction the model estimates, a sum of the sunlit and shadowed ground. The secondary story spectra can be mixed with the ground spectra so the gap fraction predicted by the model is reduced. By doing a 50% mix of Douglas-fir and Salal, the prediction of the model's gap fraction was reduced by that

amount. This was a realistic amount as the amount of 5-Scale gap fraction was approximately double that measured from the LIDAR (see in Figure 43). This approach allowed for the input of the measured forest parameters into 5-Scale and provided for an account of the secondary forest.

5.10. PLS Analysis

Forest parameters used to estimate the 5-Scale spectra were compared to the output spectra produced by the model using Partial Least Squares (PLS) method. By doing so, it was possible to assess how various forest parameters influence the spectra acquired from various angles by CHRIS.

The main forest parameters used in 5-Scale were stem density, height, crown radius and LAI (see Table 7) and the output from 5-Scale is gap fraction. Two additional derived forest parameters considered were biomass and the gap fraction measured from LIDAR. Biomass was calculated based on allometric equations (Equation 7) for Douglas-fir related to the tree height and stem density. (Ter-Mikaelian and Korzukhin 1997)

Equation 7. Biomass allometric using DBH and Stem Density.

$$B = 0.0808 \times (DBH)^{2.5282} \times SD$$

where B is biomass (kg/ha), and SD is the stem density (stems/ha). DBH is diameter at breast height (cm) and was calculated from the tree's height as in Equation 8:

Equation 8. DBH calculated using tree height.

$$DBH = ((LN(1-((H-1.3)/62.034)^{(1.5024)}))/-0.0108)$$

where H is the height (85% percentile from LIDAR) (m). This equation was based on a non-linear regression fit of height and DBH values of Douglas-fir trees sampled in the GVWD (Song 2005).

Table 7. Revised Plot Parameters from LIDAR Biometrics.

Plot No	Stems per ha	$Height_{tt}$ (mean)	Crown Radius	LAI_{UofT} (m^2m^2)
4	169.8	25.4	2.6	5.03
6	300.9	16.4	2.5	6.53
7	416.7	26.6	2.1	6.58
8	177.5	41.2	4.0	7.92
14	393.5	15.1	1.7	7.09
15	115.7	45.5	4.1	5.66
16	293.2	26.7	2.6	10.04
17	108.0	37.6	3.7	6.00
18	285.5	26.8	2.2	6.88
19	393.5	12.4	1.9	1.27
20	254.6	13.7	2.7	5.19
22	200.6	29.1	3.9	7.28
25	192.9	27.1	3.5	5.94
26	293.2	19.8	3.7	6.06
28	169.8	24.4	4.3	6.23
29	185.2	30.5	3.7	1.85
30	177.5	21.4	4.0	3.76
53	192.9	43.5	4.5	6.18
54	216.0	26.3	3.4	3.01

Using PLS each of these variables were associated with the resulting 5-Scale spectra resampled to the wavelength and FWHM of CHRIS MODE 1 data. All fifteen individual CHRIS angles and various combinations of dates, and angles were evaluated. These simulations helped evaluate how the potential of CHRIS spectra, at various angles relate to forest parameters.

5.10.1. PLS process

The spectra were combined as an exploratory exercise to investigate where there are higher correspondences from PLS. Inputs into PLS are normalized transformed spectra that represent values from the dependent variable (i.e. forest parameters). Outputs are predictive coefficients for each band, that when multiplied by a normalized spectra and summed produce an estimate of the dependent variable.

Input spectra consisted of the individual spectra from each plot with all 62 bands from each of the 15 satellite positions as modeled in 5-Scale and all 10 positions of the

corrected CHRIS data. Figure 45 showed the average and standard deviation of the spectra from all the plots to illustrate the average range and shape of spectra from the various angles.

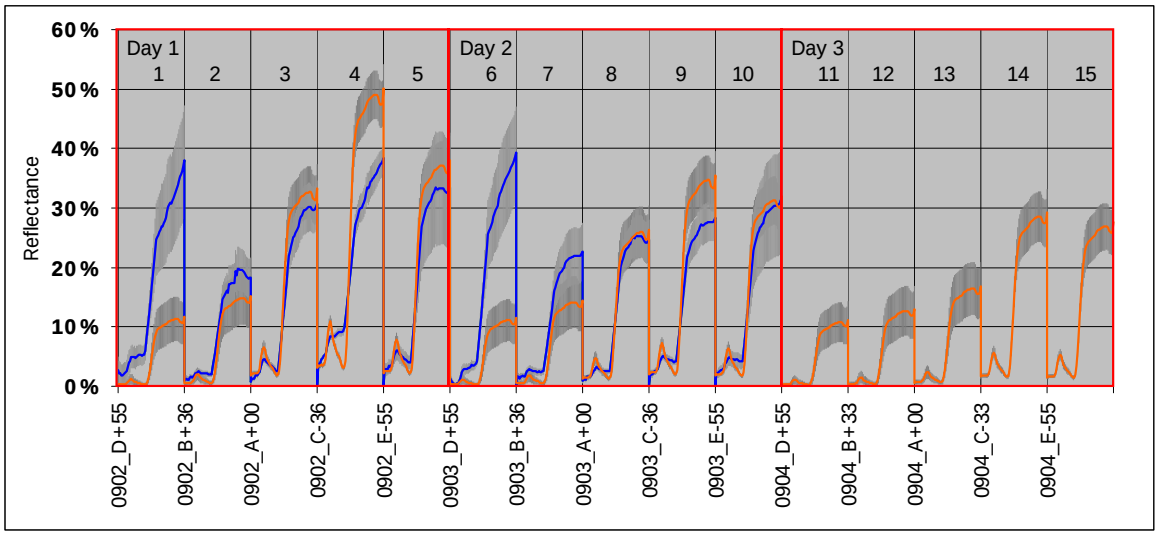

Figure 45. Average spectra for all plots for each angle from 5-Scale (Orange) and CHRIS (Blue) with 1 std dev error bars. Individual spectra from each plot were used as input into PLS. Day and spectral position (1-15) are labelled.

The exploratory exercise ran the PLS process with 28 different combinations of spectra as illustrated in Figure 46. The first 15 spectral combinations input were on an individual basis for the three dates and five angles. Spectra 16 to 18 were for all five angles combined for each of three days, where Day 1 corresponds to spectra 16 (September 2, 2006). Spectra 19 to 23 combined each angle from all three dates, starting with FZA +55 for spectra 19, FZA +36 for spectra 20 and so on until spectra 23 for FZA -55. Spectral position 4 corresponded to the bright spots (Day 1, FZA -36º) and spectra 12 was closest to the dark spot (Day 3, FZA +36º). This can be seen in polar plot of Figure 14. Spectral combination 24 was closest to sampling in a plane from the bright spot to the dark spot as possible with these CHRIS acquisitions. Combination 25 was a shorter sampling from the bright to the dark spot and 26 was a cross section to the bright to dark spot plane.

Spectra combination 27 was all 15 spectra combined (all three days and five angles) and combination 28 is equivalent to the CHRIS data processed to reflectance (Days 1 and 2).

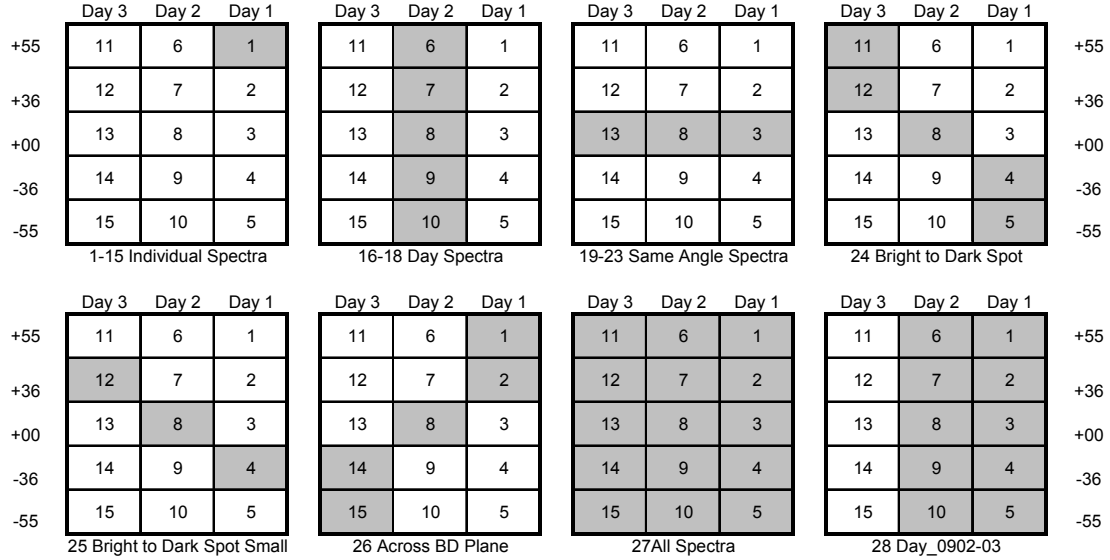

Figure 46. Combination of spectra investigated with PLS. Spectral days and positions (1-15) are labelled. Each cell represents one of 15 possible CHRIS images during triplet overpass. Gray cells are showing which cells are included in spectral stack as input to PLS.

Evaluation consisted of looking at the average R^2 of 10,000 runs of PLS for each combination of forest parameters, spectral combination and spectral transformation. The spectral transformation included using either reflectance or absorbance. For each of these there were three derivative levels of none, first or second. The following six spectral transformations were evaluated: 1. absorbance spectrum, 2. reflectance spectrum, 3. 1st derivative absorbance spectrum (3 points-quadratic fit), 4. 1st derivative reflectance spectrum (2 points-left), 5. 2nd derivative absorbance spectrum (2 points-middle) and 6. 2nd derivative reflectance spectrum (2 points-left).

PLS output the coefficients for each "band" in the normalized transformed spectra. The more extreme the value of any coefficient the more contribution to the final product is due to that spectral region. The values can be extreme in either a negative or positive

way. The spectra from "ALL" bands refers to all 62 CHRIS spectra for all five angles for all three days as run through the 5-Scale simulations. The coefficients were inspected to see which bands (411-1005 nm) within which angles (FZA) and days (MZA) had the highest contribution to each forest parameter.

Assuming that PLS produces coefficients located in consistent regions of the spectra, coefficients that have significant contributions from the "ALL" spectra should be related to the better performing spectra combinations. Evaluating both the coefficients and the performance of spectral combinations was a means of evaluating the consistency of the PLS output. PLS analysis was performed using "ALL" available spectra of both spectral outputs from 5-Scale and CHRIS.

5.11. PLS Results

The consistency of good results of all spectral transformations from the chosen band combinations was much higher for forest parameters such as $GAP_{5\text{-scale}}$, and LAI. Biomass values were calculated using a combination of stem density and tree height, and it performed overall better in the 5-Scale simulated spectra than either of these two inputs on their own. Plots of the average R^2 from spectral combinations of 5-Scale are found in Appendix 2 – Average R^2 from 5-Scale Spectral combinations. The maximum average R^2 for each forest parameter derived from either 5-scale or CHRIS imagery can be found in Figure 47.

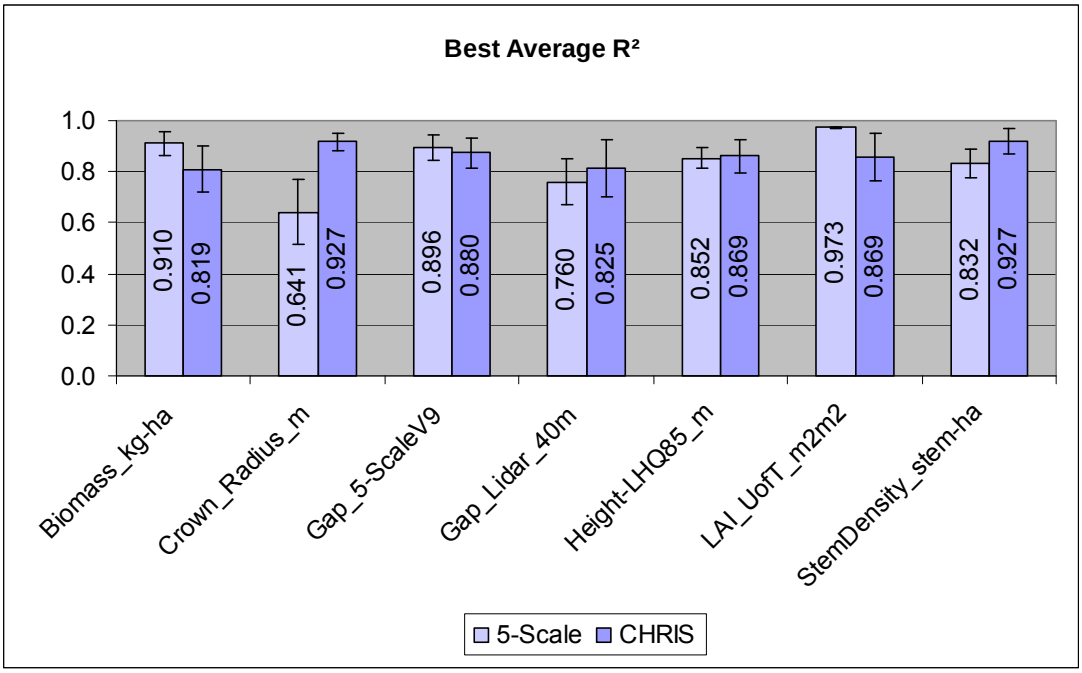

Figure 47. Maximum average R^2 and standard deviation derived using PLS from all 5-Scale spectra and CHRIS imagery.

It is interesting to note that the sum of the absolute value of all the coefficients calculated on normalized spectra was lower for forest parameters that have higher average R^2 (Figure 48). The better the relationship of the whole spectra to the dependent variable, the more all bands contributed, and less from a single band.

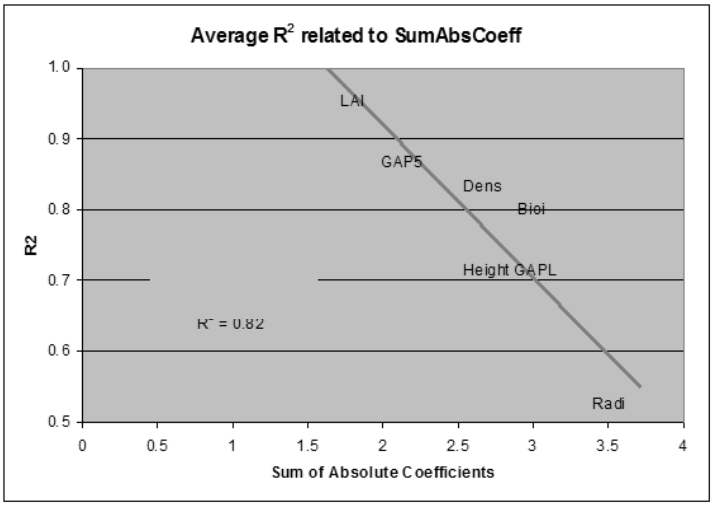

Figure 48. There is a negative correspondence between PLS predictive R^2 and sum of the absolute coefficients.

Spectral stacks from all the images acquired at the various angles resulted in an extended spectral signature. This extended signature was compared for the different forest plots to see if there were unique characteristics that distinguished the forest types.

The spectral coefficients were evaluated to identify which portion of the spectra (view angle and wavelengths) contributed the most towards the PLS prediction. This process was possible as the PLS process normalizes the spectra, making the absolute values of the coefficients from any band comparable. The dependent variable was calculated by summing up the coefficients multiplied by the transformed input spectra. Therefore the higher the values of the coefficients, the more changes in that portion of the spectra are related to the dependent variable. The change in spectra brightness or shape is measured depending on what transformation has been applied. Changes in raw spectra imply that the change in reflectance or brightness are related to changes in the dependent variables, while a change in a 1^{st} derivative relate to the change is slope of the spectra and change in 2^{nd} derivative relates the spectral rate of change of slope. The transformations used to provide the best PLS R^2 are listed in Table 8.

Figure 49 shows the coefficients resulting from calculating Biomass using PLS on the 5-Scale spectra. The dominant contributing bands are labelled. These coefficients are illustrated in another manner by a means of a Visual Python script (see Appendix 3 – Visual Python Code for Coefficient Viewing) that produces ellipsoids sized according to their relative contribution, positioned by acquisition date (MZA = X), view angle (FZA = Y) and wavelength (Lambda = Z) as seen in Figure 50. Illustrating the results in this manner allows for the viewing of the relative position of the contributing coefficients in the above 3 Dimensions in an interactive 3D environment.

Table 8. Selected spectral transformation used in PLS. (rs = reflectance spectrum and as = absorbance spectrum).

Parameter	Transformation 5-Scale	Transformation CHRIS
Biomass (kg-ha)	2nd derivative rs (2 points-left)	1st derivative as (2 points-left)
Crown Radius (m)	1st derivative as (3 points-quadratic)	2nd derivative rs (2 points-middle)
Gap 5-Scale	2nd derivative rs (2 points-left)	2nd derivative as (2 points-left)
Gap LIDAR 40m	2nd derivative rs (2 points-left)	2nd derivative as (2 points-middle)
Height LHQ85 (m)	2nd derivative as (2 points-middle)	2nd derivative rs (2 points-middle)
LAI UofT (m^2m^2)	1st derivative rs (2 points-left)	2nd derivative rs (2 points-left)
Stem Density (stem/ha)	2nd derivative rs (2 points-left)	2nd derivative rs (3 points-quadratic fit)

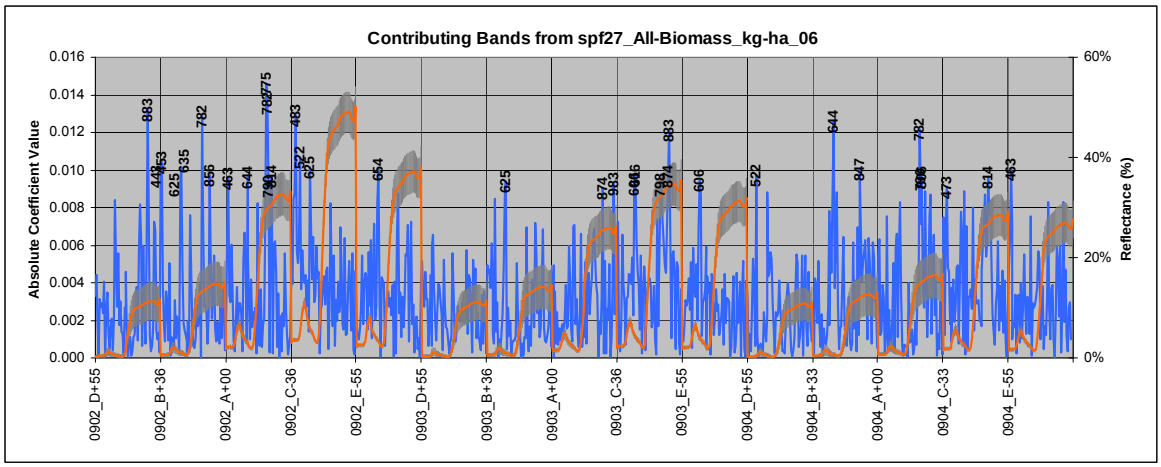

Figure 49. Contributing bands using ALL bands as input for Biomass 2nd Derivative of the reflectance Spectra. Absolute coefficient values plotted in blue with top 30% contributing wavelengths labelled. X-Axis shows all angles from each of the three days. Normal pre-transformed spectra in orange with error bars plotted for reference purposes.

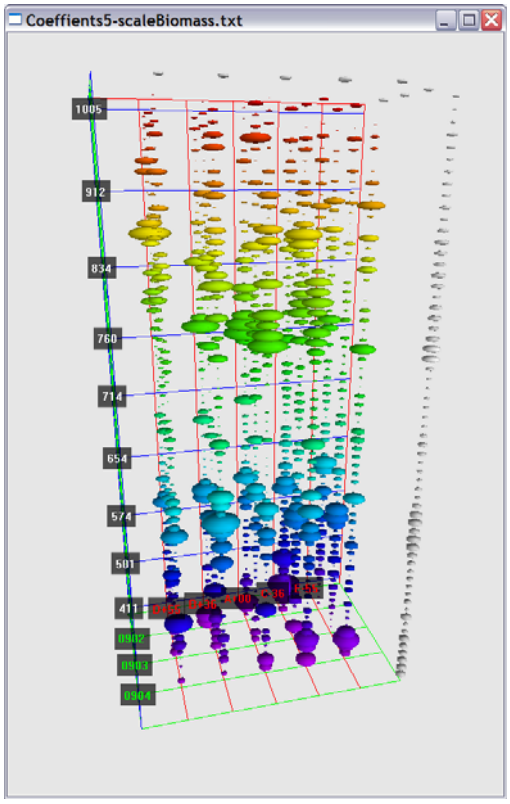

Figure 50. Coefficients from PLS regression relating Biomass from 5-Scale spectra shown using the Visual Python Script. Colours vary by wavelength, the floor holds 15 triplet CHRIS locations. Outside gray are average coefficients. Running the script in Python allows for 3D visualization

A complete illustration of all coefficients viewed from four angles is shown in Appendix 4 – Visual Python Figures for Coefficient Viewing. The PLS coefficients for forest parameters from both 5-Scale and CHRIS are illustrated as "beads" for all angles and wavelengths. The sizes of the beads are relative to the contributions the individual coefficient contributed to the prediction of the dependent variable. The location of each bead relates to the angle (FZA) and day (MZA) and wavelength. For 1st derivative transformations, the coefficient contribution relates to the slope of the spectra, while 2nd derivative transformations relate to the change is slope centered on the wavelength.

For each dependent variable the "best" results were analyzed (see Figure 47). Analysis of the CHRIS data included only two dates of imagery, resulting in 10 of the 15 spectra included in the 5-Scale data as input into the PLS analysis. A comparison of the location of the coefficients resulting in using the full set of the 5-Scale spectra and the 10 spectra subset captured by the CHRIS reveals that the contributing coefficients remain in the same locations. An example (Figure 51) show the consistency of the coefficient locations from the PLS of the height parameter using all 5-Scale derived spectra and the CHRIS 2-date subset.

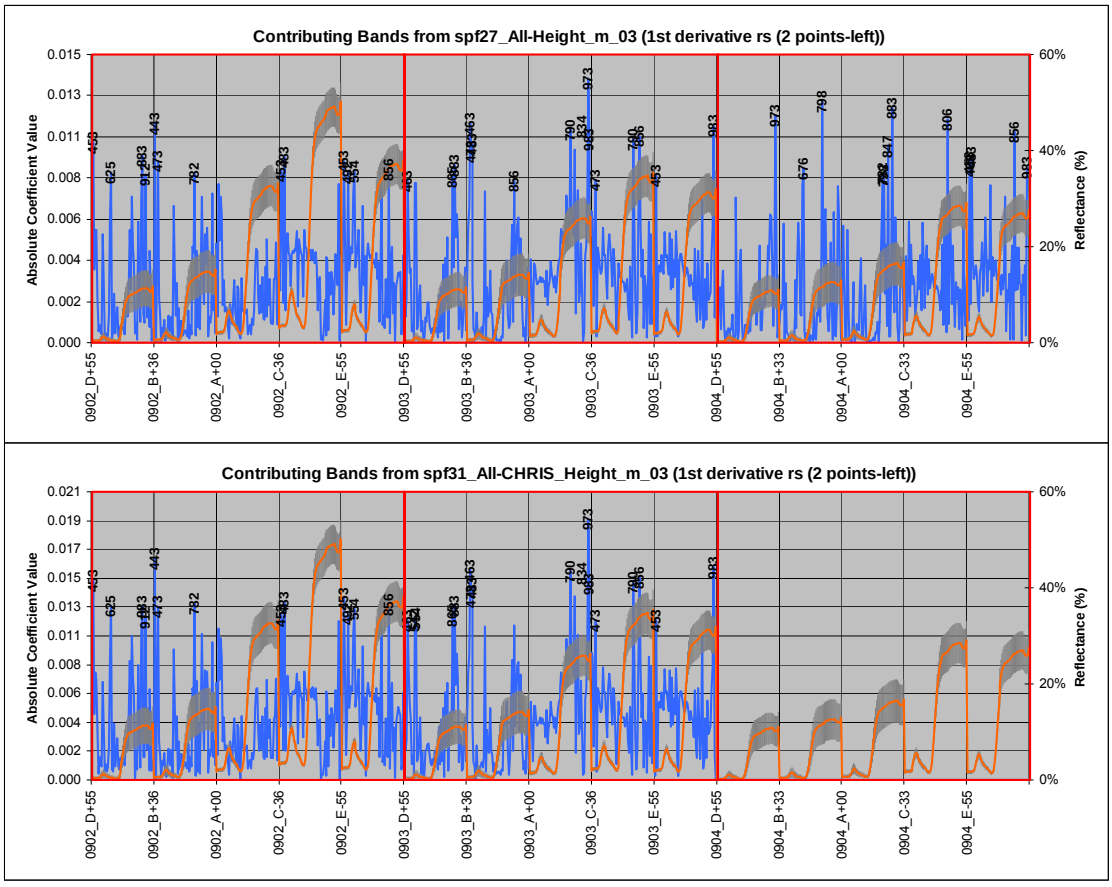

Figure 51. Location of PLS absolute coefficients from 5-Scale derived height using as input, all spectra and the CHRIS two-date subset. Dominant coefficients locations remain the same showing that using an input subset results in stable coefficients.

5.12. Forest Parameter PLS Findings

The following section summarizes the findings of the PLS analysis for each forest parameter (dependent variables). This analysis consisted of a description of the forest parameter comparing results when using the CHRIS spectra and the 5-Scale spectra as input. Comparisons included the R^2 results of the PLS process as well as the location of the dominant coefficients relative to spectral position and view angle. See Figure 14 when there are references to FZA (angle) and Day number (MZA). The location of the dominant coefficients described the area from within the spectral signature and which view angles contributed to calculating the PLS regression results. The coefficients were based on normalized spectra; their values were multiplied by the transformed spectra, which in turn were summed up to predict the dependent variable. Please reference Appendix 4 – Visual Python Figures for Coefficient Viewing for multiple views of the 3D coefficient distributions. The location of these coefficients may relate back to the physics of light interaction with foliage and the canopy structure being measured.

5.12.1. Height

The height of each plot was measured as the 85% percentile from the LIDAR data. The reflection of light from a canopy that is tall versus from one that is shorter most likely will vary due to other parameter's that correlate to height, such as age and structure. Shorter stands are younger and more likely will have a high stem density and be more even aged, resulting in less crown closure. Taller stands more likely have structure related to older stands, with less stem density, more gap and varied ages of trees and have a secondary growth; resulting in more shadows. As seen in Figure 47, the height parameter has an R^2 of 0.852 from 5-Scale and 0.869 from the CHRIS spectra.

PLS results for height from 5-Scale were based on a 2nd derivative of the reflectance spectra using 2-points left. The largest cluster of coefficients was in a region just after the red edge, (768-806 nm) at FZA -55 as well as in the region just after the green peak (564-625 nm) on the first day (MZA = 20º) (near the hot spot). The same angle also had a small cluster in the red edge (714-720 nm) in Day 2 (MZA = -2). The green peak of FZA -36º for Day 2 also contained a small but broad cluster over the green peak (632-669 nm). There were a few other individual coefficients throughout, but most of the contribution came from the first day (MZA = 20º) and Day 2 (MZA = -2) in the FZA of -36º and -55º from the infrared, red edge and green peak spectral regions.

PLS results for height from CHRIS had a concentration of coefficient clusters in Day 2 in the green peak and red edge regions for the three FZAs of: +36º, Nadir and -36º. From Day 1 FZA of +55º there was a cluster located the red region (543-574 nm) and in the infrared there were two clusters, one at 858-874 nm and another at 931 nm. For FZA

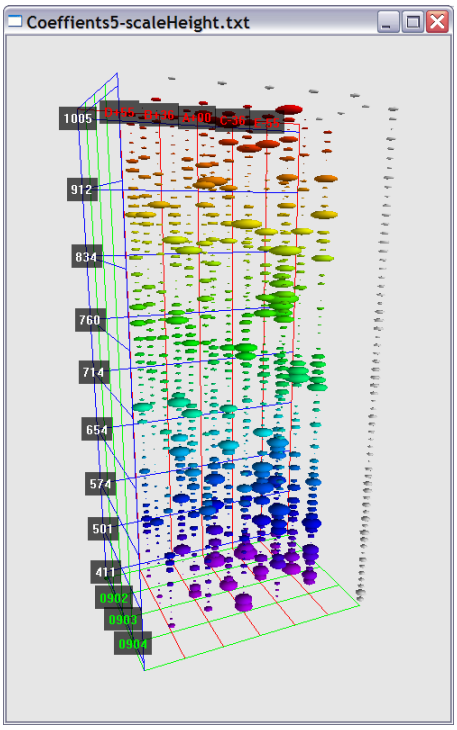

Figure 52. PLS Coefficient distribution from 5-Scale spectra and Height.

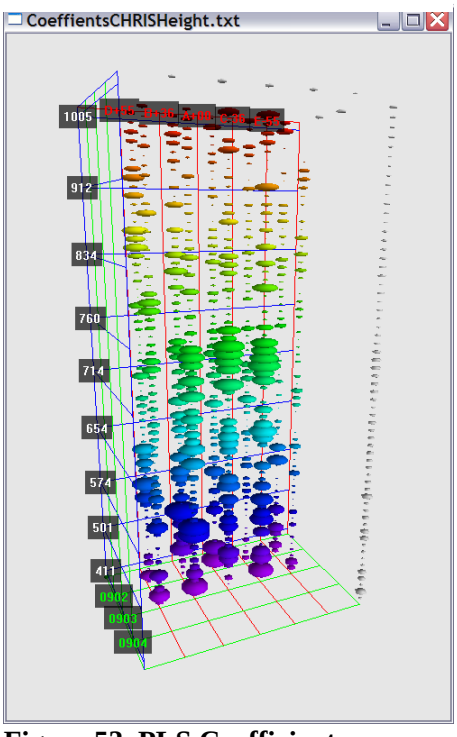

Figure 53. PLS Coefficient distribution from CHRIS spectra and Height.

+36º there were clusters all through the visible region and a couple of smaller ones in the red edge and near infrared. The nadir image of day 1 had significant coefficient contributions in the blue region (453-473 nm) and smaller individual ones into the red edges. The CHRIS PLS results were created mainly in the visible red edge of mid three FZAs of Day 2, with additional contributions from the visible areas of the three first FZAs (+55, +36 and nadir) of Day 1.

5.12.2. Stem Density

The stem density was estimated by the LIDAR Tree Top and adjusted after visual inspection of high resolution imagery. Variations in stem density has affected reflectance of multi angle light off the canopy as higher density usually is related to younger stands and therefore the canopy would likely have been more even and have less gaps producing less shadows. Lower stem density means there was an increase in the distance between trees, which could be due to older stands containing bigger trees that would have larger crown radii or open stands producing more opportunity for light to reflect from the ground instead of only within and on the canopy. As seen in Figure 47, the stem density parameter has an R^2 of 0.832 from 5-Scale and 0.927 from the CHRIS spectra.

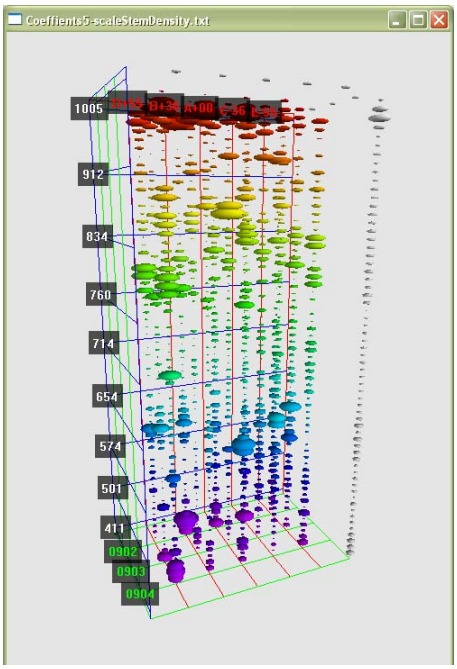

Figure 54. PLS Coefficient distribution from 5-Scale spectra and Stem Density.

Stem density PLS results from 5-Scale were based on the 2nd derivative 2 points left reflectance spectra. The largest cluster of coefficients was located from the Day 2 nadir in the infrared region (874-947 nm). There were a concentrated collection of clusters located near the end of the infrared bands (874-1005 nm) for the FZA +55 and FZA +36 from all three days including FZA +00 for Day 3. Any coefficient located at the end of an individual spectra (1005 nm), was caused by looking into the beginning of the next spectra (410 nm) as the 2nd derivative 2 points left has a width of three bands (see Table 1). If the spectra were concatenated in a different order, these coefficients may not occur in the same place. There are a few other clusters of coefficients as well: FZA +55 on Day 3 has several larger coefficients located in the red-edge and through the infrared region (714, 782- -892 nm), Day 1 FZA +55 has a cluster of coefficients continuing from 1005 nm to FZA +36 463 nm, plus there are a few other individual larger clusters in the red 616-654 nm in some of the other columns. For 5-scale PLS of stem density, most of the coefficients are located in the infrared region (874-947 nm) looking into the shadows of the forest canopy.

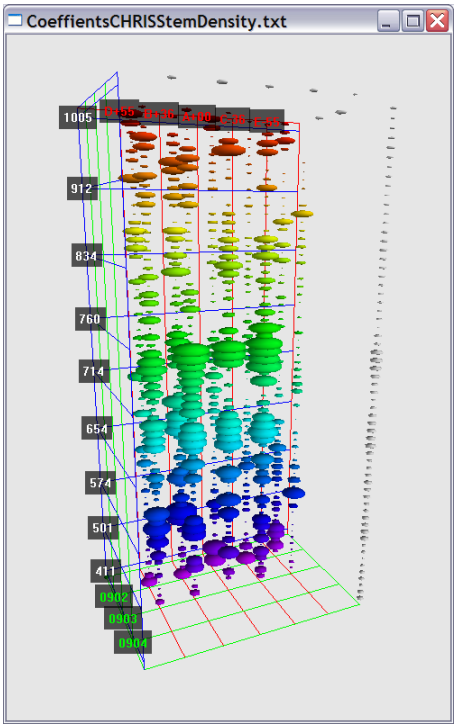

Figure 55. PLS Coefficient distribution from CHRIS spectra and Stem Density.

In the PLS analysis of CHRIS spectra for stem density a very strong set of coefficients clustered through the top of the red edge (733-746 nm) for all FZAs of Day 2 (MZA +2) except FZA -55. A cluster located in the same regions only occurred at

FZA +36 in Day 1. This two day pattern was repeated in the beginning of the red edge (644- 684 nm). FZA +36 in Day 1 and Day 2 also contains a large cluster in the green peak (532-542 nm). There were a few other clusters scattered in the near infrared region. The main contribution of stem density in the PLS analysis came from Day 2 (MZA 2º) and FZA +36 at the start and end of the red edge region.

5.12.3. Crown Radius

Crown radius was calculated by averaging the radius of drawn circles around a sample of trees seen in high resolution imagery for each plot. Larger crowns, associated with larger and therefore older stands, would have greater shadowing in the canopy structure. Smaller crown sizes would be from younger stands and therefore more likely be even aged with possibly higher density and less shadows. The dependent variable crown radius is related to stand height and density, and should be predicted with the PLS regression. The best PLS regression results from 5-Scale input absorbance spectra (1st derivative (3 points-quadratic)) was only 0.641. However, using the CHRIS reflectance spectra (2nd derivative (2 points-middle)) the best PLS results had an R^2 of 0.927 (see Table 8).

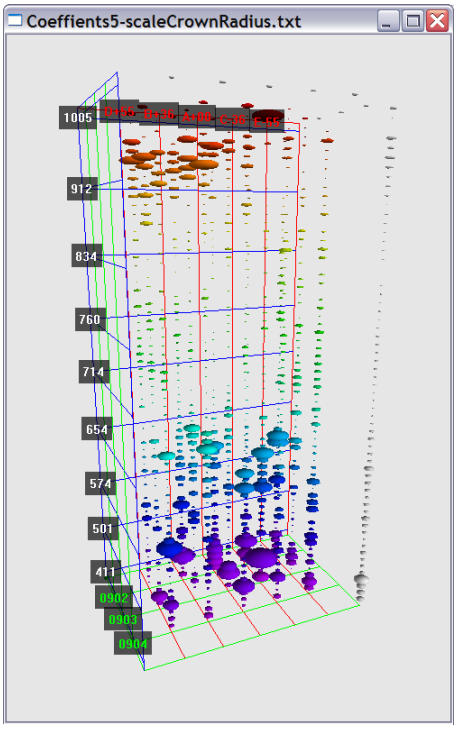

Figure 56. PLS Coefficient from 5-Scale spectra and Crown Radius.

The poorer performance of the PLS using 5-Scale spectra as input has produced a coefficient map that seemed to have a void of contributing coefficients from the red edge to infrared region (684-902 nm). The largest coefficient clusters appeared in the blue region (453-473 nm) for Day 2 FZA +36 and nadir, Day 1 FZA +36 to FZA -36 and Day 3 nadir and FZA -36. There are some scattered clusters in the visible region; notable ones were found on Day 3 FZA +55 and the green peak (554 nm) and another in Day 1 FZA -55 at the red region (625-635 nm). After the void in the red edge and into the infrared region, there were a few scattered clusters in the remainder of the infrared region (930-962 nm) mostly in the FZA +55 to nadir view angles of all three days.

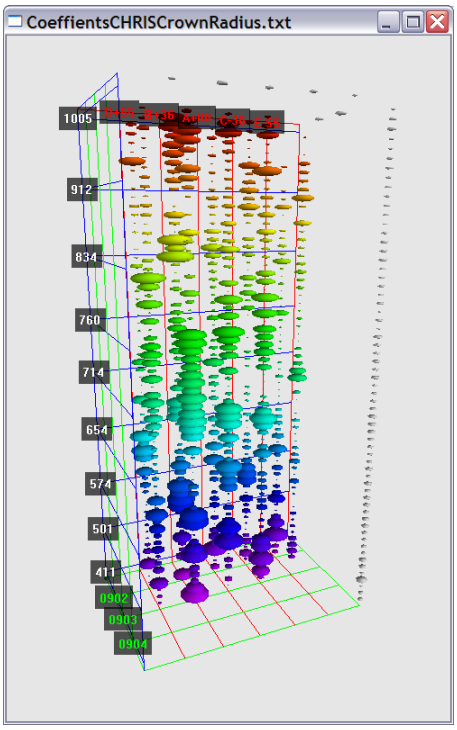

Figure 57. PLS Coefficient from CHRIS spectra and Crown Radius.

In the PLS analysis of CHRIS spectra for crown radius gave a very strong set of coefficients along FZA +36 on Day 2 throughout the whole red-edge (654-746 nm). Nadir and FZA -36 on Day 2 have clusters that were located at the beginnings and ends of the red-edge (654-665 nm and 746-775 nm). FZA +36 for both Day 1 and Day 2 had clusters of coefficients in the green peak (532-554 nm). There were three large coefficients in the green peak for nadir and FZA -55 for Day 1 and FZA -36 for Day 2 (554 nm).

A large cluster was located in FZA +36 of Day 1 in the infrared region (814-847 nm) and at the end of the infrared region (947-1005 nm). There were other scattered large coefficients near the end of the infrared region as well.

5.12.4. Biomass

Biomass for each plot has been calculated as a function of height and stem density (see Equation 7.). Larger biomass values per plot would mean more forests, most likely due to more mature, taller forest, thereby providing a more shadowed canopy that would have more variability in light when viewed from different angles. PLS results using 5-Scale spectra as input produced an R^2 value of 0.910 using 2nd derivative (2 points left) of the reflectance spectra and with CHRIS input spectra the R^2 is 0.819 using 1st derivative (2 points left) of the absorbance spectra (see Table 8).

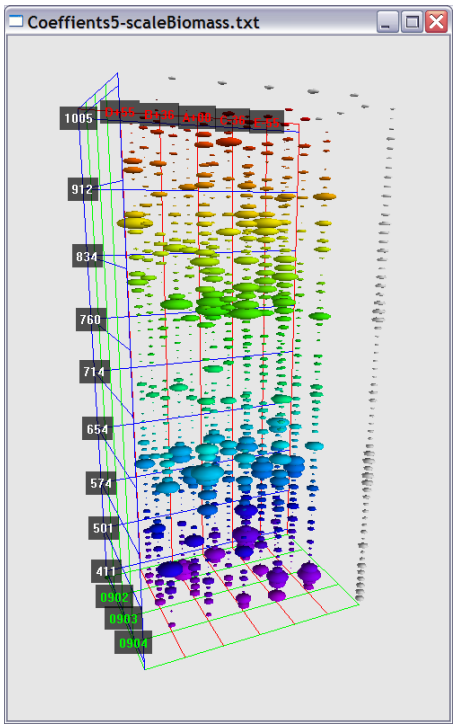

Figure 58. PLS Coefficient from 5-Scale spectra and Biomass

The distribution of coefficients from the PLS results for Biomass with 5-Scale spectral inputs had very little contribution in the red edge region (654-750 nm) in all angles and days. There were large contributions in the infrared regions, especially from FZA -36 in Day 2 (782-847 nm) and in Day 1 nadir and FZA +36 in the beginning of the infrared region (775-782 nm). On Day 3 nadir there was a large cluster in the near infrared as well (782-803 nm). There were several other larger individual coefficients spread through the infrared region. There was also a scattering of larger coefficients in the green peak

region (584-644 nm) and to a lesser extent in the blue region (443-463 nm), especially in Day 1 FZA +36, nadir and FZA -36.

Using CHRIS absorbance spectra transformed to a 2nd derivative (2 points left) as input into PLS produced lower R^2 values than when the 5-Scale spectra was used as input, and there are less coefficients "beads" that can be seen in Figure 59. Most of the larger clumps and individual coefficients were throughout the visible portion, notably in the blue regions of Day 1 FZA +55 (443-553 nm), FZA -55 (493-616 nm) and Day 2 FZA +55 (606 nm), and FZA +36 (463-511 nm). The strongest coefficient in the infrared region was located at 973 nm.

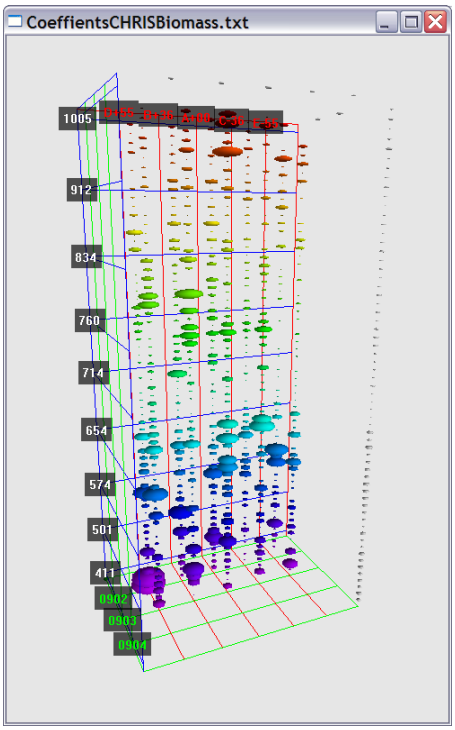

Figure 59. PLS Coefficient from CHRIS spectra and Biomass

5.12.5. Gap Fraction from 5-Scale

Canopy gap fraction was estimated by simply summing up the ground shadow and sunlight components for the nadir view of the 5-Scale model run. This nadir estimate of gap was generated by the 5-Scale model from the input average stand parameters such as height, crown radius, stem density and LAI (see Table 6). $GAP_{5\text{-Scale}}$, was a product of all input forest parameters which made it a good over-all indicator of the relations of forest parameters to spectra within the context of the 5-Scale model.

PLS results using 5-Scale spectra as input produced R^2 value of 0.896 using 2nd derivative (2 points left) of the reflectance and with CHRIS input spectra the R^2 is 0.880 using 2nd derivative (2 points left) of the absorbance spectra (see Table 8). The CHRIS results did relatively well considering that the spectra are produced from viewing the real plots and the 5-Scale gap fraction are calculated from the model combining all the average input plot parameters.

Clusters of coefficients were distributed throughout the infrared (798-962 nm), blue and some in the red regions of the spectra. There were very few larger sized coefficients within the red edge. The biggest cluster was found on Day 1 at FZA -36 and FZA -55 in the infrared region of (775-814 nm). There were other clusters neighbouring this area in Day 2. Day 3 had a large cluster at FZA -36 at in the infrared (865-922 nm) and at nadir (892-922 nm). FZA +36 of Day 3 had several clusters of coefficients throughout the infrared region. The blue region had some large clusters the largest was on Day 3 FZA +36 (443-

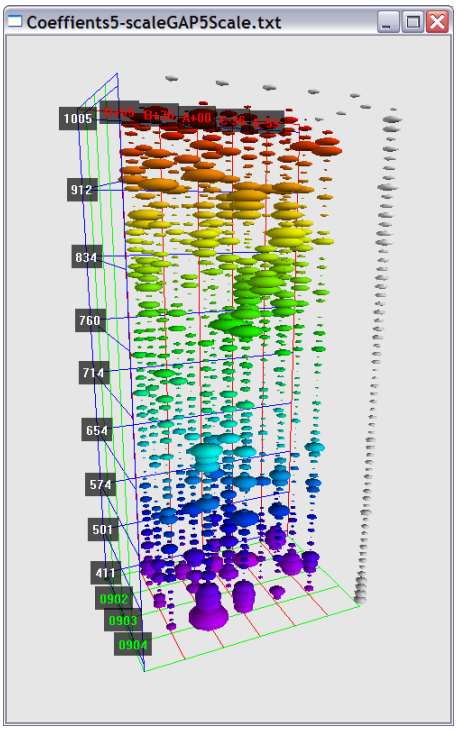

Figure 60. PLS Coefficient from 5-Scale spectra and $GAP_{5\text{-Scale}}$

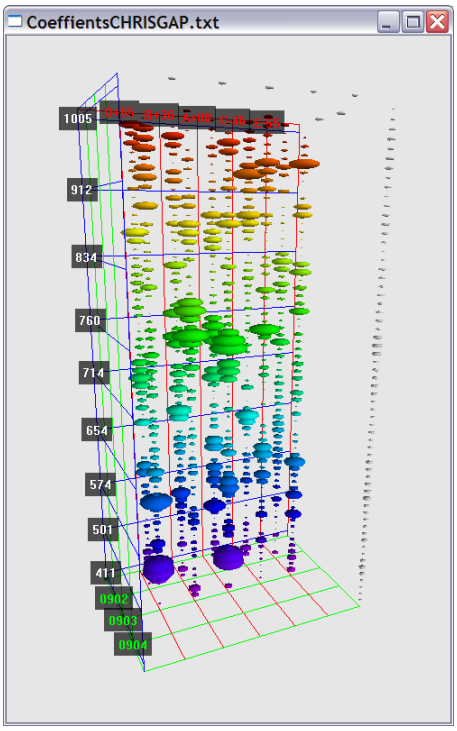

Figure 61. PLS Coefficient from CHRIS spectra and $Gap_{5\text{-Scale}}$

473 nm).

The CHRIS spectra was also used as input into the PLS to correlate 5-Scale generated gap fraction measurements. The largest correlations were found on Day 1 and Day 2 from FZA +36 to FZA -36 in the red edge region, an area void of coefficients when 5-Scale generated spectra were used to calculate PLS. Day 2 nadir had a cluster from 720-750 nm, FZA +36 had one from 753-790 nm, FZA-36 had one large coefficient at 760 nm. Day 1 nadir had clusters from 720-768 nm and FZA +36 had a cluster from 746-775 nm. The infrared region had clusters of coefficients throughout the 912-992 nm region, especially Day 1 FZA -36 at 947-962 nm. The blue region had a couple of clustered coefficients at Day 2 Nadir 482-492 nm, FZA +55 482-501 nm.

5.12.6. Gap Fraction from $LIDAR_{40m}$

The LIDAR biometric gap fraction (GAP_{LIDAR}) was calculated as the percentage of LIDAR hits that make it through the canopy and reach the ground within a 40m cell. The CHRIS spectra were a direct measurement of these plots where as the 5-Scale spectra were a measurement of spectra derived from the plot parameters. The CHRIS spectra input into PLS for GAP_{LIDAR} produced slightly better R^2 results (0.825) compared to using the 5-Scale input spectra (0.760) as PLS (See Figure 47).

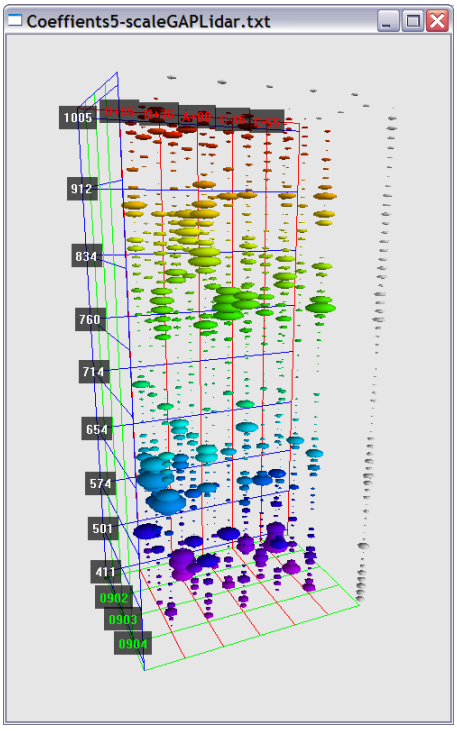

Figure 62. PLS Coefficient from 5-Scale spectra and Gap_{LIDAR}

The 5-Scale spectra were transformed using a 2^{nd} derivative (2 points-left) of the reflectance

spectra. There is an area void of large coefficients in the red edge (676-760 nm) for all days and FZAs. There are a few major clusters of PLS coefficients in the infrared region, some on the FZA +55 side in the red region and in the blue region of Day 1. The largest cluster of PLS coefficients was found in the centre: Day 2 Nadir from in the infrared region (760-798 nm) followed by two further into the infrared region (834-902 nm) at FZA +36 for Day 2 and Day 3. The red region (593-634 nm) had two large clusters found in FZA +36 of Day 2 and Day 3. In the beginning of Green region (522 nm) there were several larger isolated coefficients in Day 1 FZA +55, FZA +36 for Days 2 and 3 and Nadir on Day 2. The Blue region had two clusters in the spectral range of 453-473 nm for Day 1 FZA +55 and FZA -36.

The 5-Scale spectra were transformed in a 2nd derivative (2 points-left) of the absorbance spectra. The coefficients were scattered throughout the spectral and spatial domain, most were within the FZA +36 to FZA -36 region. There were two clusters in the center's (Day 2 Nadir) red to edge region (665-760 nm). A similar but smaller cluster can be seen in Day 1 FZA +36. The top of red edge had two clusters from 753-775 nm in Day 1 Nadir and Day 2 FZA +36. Day 1 FZA +36 had a large cluster in the infrared from 883-847 nm. The visible had a few larger individual coefficients scattered throughout; namely, Day 2 FZA -36 (564 and 584 nm).

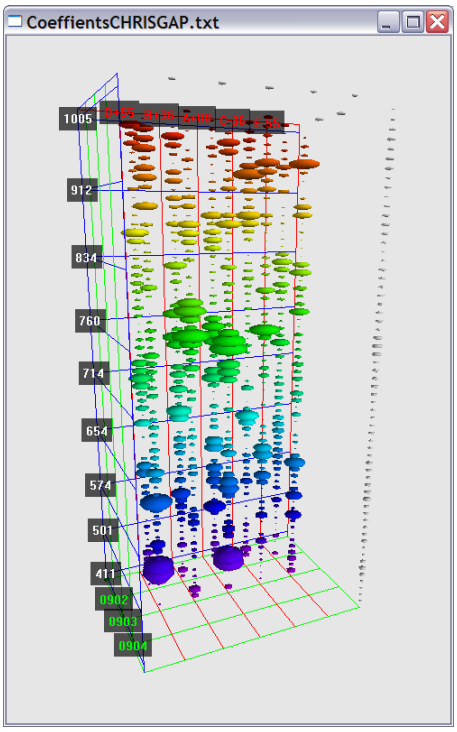

Figure 63. PLS Coefficient from CHRIS spectra and Gap$_{LIDAR}$

5.12.7. LAI

Leaf Area Index (LAI) is a measure of the area of the leaf's upper surface within a canopy relative to the area of the ground. LAI differs from the gap fraction measurement in that gap fraction measures the area of the ground exposed to the sky. 5-Scale uses the LAI parameter to derive the predicted spectra, which was evident in the orderliness of results.

The LAI measurements where made with the Li-COR 2000 during the summer of 2002 by UVic and processed by U of T with the intent of using these measurements with the 5-Scale RTM model. The highest R^2 results of all the PLS analysis was from the 5-Scale spectra and the LAI forest parameter (0.973), while using the CHRIS data the PLS produced an R^2 value of 0.869.

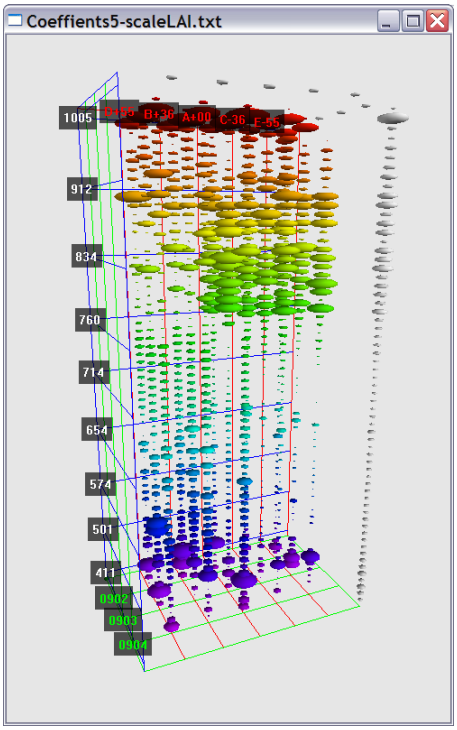

Figure 64. PLS Coefficient from 5-Scale spectra and LAI

The 5-Scale spectra were transformed using 1st derivative (2 points left) of the reflectance spectra. There was a very orderly distribution of the coefficients. There was a cube of clusters from Nadir to FZA -55 from Days 1 to 3 and from 760-912 nm. Every column had a large coefficient at the end (994 nm) which linked into the beginning of the next column in the concatenated spectra. There were also a few larger coefficients scattered in the visible region.

The CHRIS reflectance spectra were transformed using a 2nd derivative (2-point left) as input into the PLS regression for LAI. There were a few clusters from this PLS that were in the red edge, infrared and visible ranges. The main clusters could be found on Day 2 in the FZA +36 red edge (702-720 nm) and Day 1 Nadir (702-714 nm). In the infrared region there were some clusters located at 768-790 nm in Day 1 FZA -36, 782-798 nm in Day 2 FZA -36 760-782 nm in Day 1 FZA +36. Day 1 had consistent larger coefficients from FZA +36 to FZA -55 for 883-892 nm while the cluster at FZA -55 continued from 883- 922 nm. There were several large coefficients scattered in the end of the CHRIS infrared region (931-1005 nm). The notable clusters located in the visible region were located at 453-473 nm at Nadir of Day 2 and 542-554 nm at Day 1 FZA -36.

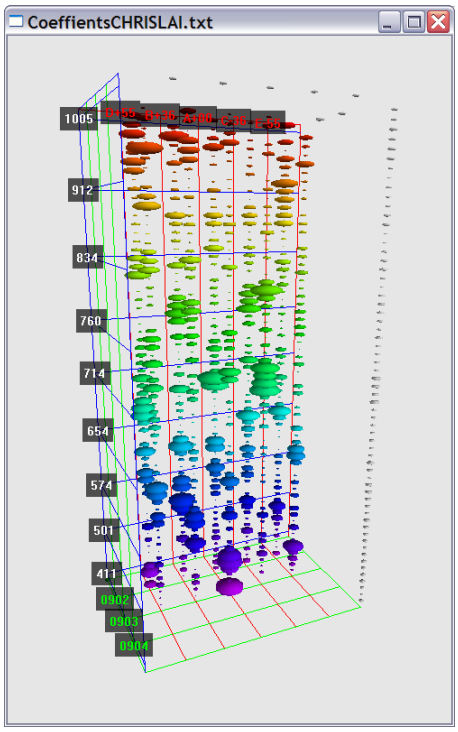

Figure 65. PLS Coefficient from CHRIS spectra and LAI

5.13. PLS Summary

The performance of using single CHRIS scene spectral as input into the PLS held consistent with the location of the relatively large coefficients in a PLS that had input all the spectra in sequence as was found in section “5.11 PLS Results” (page 83). For example gap fraction from LIDAR analysis using 5-Scale found most contributions were from angles of FZA +55 and FZA +36 could be seen in the large clusters of coefficients located in this region (see Figure 62).

Regions of contribution to the PLS correlation analysis, as described by the clusters of larger coefficients, are related to interaction of light, the BRDF and spectral regions. The vast majority of contributions for all dependent variables were mostly from FZA +36, nadir region to FZA -36 (see Table 9) which showed that the imagery nearer to nadir was the most important perspective to provide forest information. FZA +36 and FZA -36 had more dominant coefficient clusters than only the nadir which showed that slightly off nadir imagery provided more forest information than only the nadir view. There are many fewer incidences of coefficient contributions coming from the extreme angles (FZA +55 and FZA -55) for any of the three Days (MZA +20 to MZA -20).

The parameter biomass was a function of the two parameters height and stem density. Biomass from 5-Scale (*5B*) does not have coefficients located near the 5-Scale stem density (*5SD*) or 5-Scale height (5H) as expected. The same is true for CHRIS Biomass (*CB*) except at Day 2 FZA +36, where all three (CHRIS biomass, stem density (CSD) and height (CH)) have strong coefficients. These biomass examples showed that the coefficient locations from similar forest structural parameters do not always appear in the same locations.

As LAI and gap fraction are related parameters, a measure of light coming through the canopy, there was good co-location of 5-Scale LAI (5L) and 5-Scale $GAP_{5\text{-Scale}}$ (5G5). This was also true from the CHRIS prediction of GAP_{LIDAR} (CGL) and LAI (CL). This showed that there could also be some stability of coefficient locations on similar forest parameters.

Table 9. Angular location of dominant PLS coefficient clusters.

	FZA +55	FZA +36	FZA +00	FZA -36	FZA -55
Day 1 (MZA +20)	*5SD* *CB* 5GL	*CSD* 5CR CCR CL CG5 CGL	*5B* CCR 5L CL CG5 CGL	*5B* 5CR CCR 5L CL 5G5 CG5 CGL	5H *CB* 5L CL 5G5
Day 2 (MZA -02)	*5SD* *CSD* *CB* 5GL	CH *5SD* *CSD* *CB* 5CR CCR CL CG5 5GL	CH *CSD* 5CR 5L CG5 5GL CGL	5H CH *CSD* *5B* CCR 5L 5G5 CG5 5GL CGL	5H 5L 5G5
Day 3 (MZA -20)	*5SD* 5GL	5G5 5GL	*5B*	5CR 5G5 5GL	

Legend	5-Scale	CHRIS		5-Scale	CHRIS
Height	5H	CH	**Crown Radius**	5CR	CCR
Stem Density	*5SD*	*CSD*	**LAI**	5L	CL
Biomass	*5B*	*CB*	**$GAP_{5\text{-}Scale}$**	5G5	CG5
			GAP_{LIDAR}	5GL	CGL

Chapter 6. Summary

6.1. Overview

This thesis investigated the influence of various forest attributes on the spectral reflectance over time and view direction. Multi-Angle, Multi-Date, Hyperspectral imagery of forests has been used to provide estimates of these canopy characteristics.

The Compact High Resolution Imaging Spectrometer (CHRIS) aboard the ESA PROBA satellite provided a unique viewing opportunity of a forested region. The programmable hyperspectral sensor imaged the same ground five times during a single overpass. Images acquired during different days provide views from different cross track angles.

The data acquired from this sensor provided another dimension in hyperspectral analysis, multi-temporal, spectrodirectional imagery acquired at a high resolution for specific targets. This thesis has investigated the multi-temporal and multi-angle aspects in forest species and density classification (see Chapter 2 Multi-Temporal, Multi-Angle Evaluation with CHRIS of Forests). Various methods were developed to calibrate the imagery (see Chapter 3 CHRIS Acquisition Field Calibration Method) and to process these data sets (see Chapter 4 Image Processing Methods). Hyperspectral imagery acquired from a range of angles surrounding the target was used as input into PLS to evaluate forest parameters (see Chapter 5 Spectral Processing Methods). Extraction from the multi angle views was possible from concurrent multiple overpasses of CHRIS and simulations from the 5-Scale Radiative Transfer Model.

The reflection of light from a forest canopy is influenced by the illumination and viewing geometry as well as the stand characteristics. The stand variables investigated

include the structural parameters (stand properties such as height, density, crown closure, LAI, Biomass) and spectral properties (Species).

6.2. Methodological Developments

Data acquired from the CHRIS sensor provided many challenges to the early adopters to deal with issues related to: multi-angle image registration that had variable pixel sizes, noise reduction, dropped pixels, variable atmospheric conditions to correct and unique ground calibration methods. New methods were developed and other established methods were adapted to deal with these issues.

6.2.1. Noise Reduction

The striping of Level 1 CHRIS data was dramatically reduced as a result of the noise correction using an algorithm that is now available to the public, as it has been incorporated into ESA's BEAM software (BEAM is an open-source toolbox and development platform for viewing, analysing and processing of remote sensing raster data). Horizontal noise was found to be not evenly distributed, of the 795 bad lines found in the five dates of Level 4 CHRIS data used for the classification evaluation , 78% were found in bands 13-18 (742 nm-792 nm) and 69% in the backward looking FZA's (-36º and -55º) (Goodenough et al. 2005b). The MNF reveals that there remains residual striping even after the removal of random horizontal and constant vertical striping.

6.2.2. Geocorrection / Orthorectification

Two methods of correcting the images were utilized to align the multiple CHRIS images from the various angles and dates of acquisition, the Rational Function Model (RFM) (see Chapter 2 Multi-Temporal, Multi-Angle Evaluation with CHRIS of Forests) and a physical satellite model (see Chapter 3 Image Processing Methods).

RFM allows for the correction of imagery in higher topographic relief areas using only ground control points (GCPs) and a digital elevation model (DEM). Approximately 50 GCPs were required to make the correction over the watershed area, resulting in an average RMS positional error of 0.95 pixels. The greater the FZA angles, the higher the RMS, nadir images had an error of only 0.71, FZA ±36º was 0.95 and FZA ±55º had an RMS error of 1.1 pixels (Goodenough et al. 2005b). The images acquired at higher FZAs also had elongated pixels, as the distance from the sensor to the ground increased. The resulting elongated pixels were 2/3 wider in the X direction.

Implementing the physical satellite model orthorectification process required the use of PCI's generic satellite model, CHRIS input parameters, GCPs and a DEM. The orbital model and sensor information were gathered from various sources including CHRIS header files, TLE and various journal papers. The resulting corrections from the orbital model were not as well aligned as expected (RMS error of over two pixels) so further correction was required to bring all the images into alignment (Dyk et al. 2006).

Due to the pointing error of the PROBA sensor, only a small subset of the study area was imaged at all angles on all days. For both the 2004 and 2006 CHRIS data sets there was an adequate area to perform the required analysis, but this limitation can be trouble some if one was to consider analysis of a larger area (i.e. greater than the 13 x 10 km).

6.2.3. Ground Calibration

A new method was required to collect spectral calibration data in the field with the intent of calibrating multi-angle CHRIS data to nadir normalized reflectance. The method was a modification of existing procedures wherein calibration measurements were made of a homogenous ground target during the data acquisition. These data were then used to

match the satellite imagery of the same target; any variations between these two were applied as a correction to the whole image. It was necessary to modify this method that would account for multi-angle data acquisition. A series of spectral measurements were made at the same angles as the satellite using a simple Goniometric System (Dyk et al. 2006). The spectra from these angles were then compared to the nadir measurement in order to determine a series of simple ratios. The spectra from the calibration walks made at nadir were then multiplied by these ratios to give the calibration spectra for each angle.

A series of quality control methods were developed to ensure that the multiple spectra collected for each reading had no anomalous readings. The Spectral Difference Angle was computed for each spectra compared to the average from the reading. Any accidental shadowing or other bad readings were identified and removed from the sample. The variance of the spectra was also recorded. As many readings go into a spectral sample, the range of values gives a sense of the "thickness" of the resulting spectra. When comparisons of various spectra are made, the variance gives a sense of how separate the spectra are. The equations to combine two spectra from the same population were derived, allowing the input to be the combined count, mean and standard deviation. These algorithms can be implemented in an image processing system to calculate the average spectral reflectance, count and standard deviation, by adding one reading at a time.

6.2.4. Atmospheric Correction

The CHRIS imagery was required to be atmospherically corrected to ground reflectance in order to be directly compared to modeled reflectance from 5-Scale. The MODE 4 dataset was not atmospherically corrected as there was a lack of water vapour absorption bands available in this Chlorophyll band set. It was only possible to correct

the one date's nadir image using FLAASH (Goodenough et al. 2005b). The correction was very reasonable as it produced similar results to a Hyperion image for which ground calibration data was collected. Since the species classification process used an MNF transformation and training sites in a supervised classification process, having the data in ground reflectance was not essential to evaluate the CHRIS data for forest species classification.

The atmospheric correction package ATCOR was selected to perform the atmospheric and topographic corrections of the September 2006 CHRIS data set. The software is based on pre-runs of MODTRAN 4 radiative transfer code and was designed to handle the CHRIS bands sets, the various sensor angles and topographic relief. Preparation of the data for atmospheric correction required many steps of preprocessing. A DEM with matching resolution to the imagery was required to be generated to produce slope, aspect, a sky-view and cast shadow data sets. Input parameters required included visibility, sensor and sun geometry, selection of appropriate aerosols and ground spectra over a known target. Despite all the effort to account for the rugged terrain in the atmospheric correction process, a high number of erroneous values were produced. It was necessary to run the model in flat terrain mode in order to get acceptable results.

6.3. Forest Species Classification

The CHRIS nadir images acquired over a growing season have been used improve the accuracies of forest species recognition and stand densities compared to a single nadir view only. Multi-angle data for CHRIS analysis of forest species also produces higher accuracy and is easier to obtain than multi-date (see Multi-Temporal, Multi-Angle Evaluation with CHRIS of Forests).

The analyses were performed on five dates of imagery over the GVWD from April through October 2004. An MNF transform was performed on each of the 72-layer stacks of four FZA for each date (FZA -55 was excluded from each date), each 18 bands (CHRIS Mode 4) and on the 90 band nadir stack. Input into the supervised classification were the first eight eigen bands derived from the 72 layer and 90 layer stacks and first five eigen channels of the nadir images. The aggregated average accuracy of only single-date nadir images was on average 80.3%. A fused data stack of all these nadir images produced an accuracy of 90.2%, a significant 10% improvement, demonstrating the importance of multi-temporal data for forest species classification (Goodenough et al. 2005b). Multi-angle images from each overpass were also used to as input stacks and compared to the classification results of the overpass's nadir only image. Multiple views of the target area improved the discrimination of stands with different densities. Over the five dates average overall classification accuracies improved a significant 8% in the aggregated results.

6.4. Forest attributes using PLS

5-Scale, a Radiative transfer model, and CHRIS data have been compared as inputs into Partial Least Squares (PLS), a full-spectrum analytical method that offers relations between forest stand parameters and the resulting spectra. The areas (view angle and spectral regions) where the dominant predictive coefficients are located, highlight within the multi-angle spectra, the location of the major contributions to the final estimate of the various forest parameters. This prediction was possible as the results of the PLS process which was set to use three latent factors. The result is a series of predictive coefficients that when multiplied by a transformed input spectra, gives an estimate of the

dependent variable. The spectra were transformed using a 1st, 2nd, or no derivative of either the reflectance or absorbance spectra. Three derivative methods were used, two-points left, two-points middle or 3-points quadratic fit. Other outputs of the automated PLS process are an estimate of the average R^2, an error estimate resulting from multiple runs of the PLS that withhold a number of input spectra to be used as checks. The seven dependent forest variables tested with the PLS process were height; stem density, crown radius, biomass, gap fraction (from LIDAR and 5-Scale) and LAI.

Appendix 2 – Average R^2 from 5-Scale Spectral combinations, compared how the dependent variables performed (using R^2) in PLS with various subsets of input from the modelled 5-Scale spectra and all spectral transformations. The spectral subsets included individual spectra (all wavelengths from a single image), and combinations, of angles, days and other groupings. The original reflectance and absorbance spectra consistently performed more poorly than the derivative spectra in the PLS analysis.

LAI estimates were extremely good no matter what subset of spectra was used (see **Figure**) showing the importance of LAI in the spectral prediction in 5-Scale. Gap fraction from 5-Scale performance was relatively stable across all angles. There were consistently better results from using a derivative spectral input compared to the reflectance and absorbance as inputs. For biomass, the R^2 results varied when using spectra simulated from single CHRIS images as input. FZA +55 to Nadir on Day 2 and FZA +55 from Day 3 all performed relatively poorer than other single images. The height parameter also had lower R^2 values on individual images, especially from the FZA +55 angles. The gap fraction values estimates using LIDAR parameters performed especially poorly in the original (non-derivative) spectra. Most contributions were from angles of FZA +55 and

FZA +36. Stem density had the lowest R^2 from the FZA +55 and most contributions from the 2nd derivative transformations.

The vast majority of regions of contributions for all dependent variables in PLS were mostly from FZA +36, nadir region to FZA -36 which showed that the imagery nearer to nadir is the most important perspective to provide forest information. FZA +36 and FZA -36 have more dominant coefficient clusters than only the nadir which shows that off nadir imagery can provide more forest information than the nadir view. There are many fewer incidences of coefficient contributions coming from the extreme angles (FZA +55 and FZA -55) for any of the three Days (MZA +20 to MZA -20).

6.5. Uncertainties

This project relied on input data that have various levels of accuracy. Not knowing precisely this variability for all inputs, results in the final product have an unknown level of uncertainty. Our confidence in the final product is influenced by the uncertainty contributions of the input and our attempts to minimize them.

Observations collected in the field always have some level of uncertainty. To minimize errors, collection procedures are followed including repeat measurements. For example the spectral field measurements were a collection of many individual readings from the field spectrometer. These measurements were averaged to produce a representative spectra for the spectral walk and calibration spectra that measures the reflectance of the grassy target at various angles. By combining the spectra, the variability of the measured targets was tracked by calculating the standard deviation of the spectra (at each wavelength). This was graphically represented in the spectral graphs such as Figure 26 allowing for the spectral “thickness” to be visualized.

The atmospheric correction model used the assumption that the terrain was flat. Although it would have been better to account for topography, this assumption was needed in order to be able to process the imagery to correct to ground reflectance.

The 5-Scale model also has assumptions about the forest canopy that are not an exact representation of reality; however, it is suitable to simulate canopy reflectance at various view and sun angles. The trees are all the same height and width and the background assumes an isotropic reflectance. It was necessary to adjust the models results by creating a background reflectance that was "pre-mixed" with salal and a 2nd level canopy in order to minimize the uncertainty of the modelled results.

6.6. Conclusion

There are many steps in processing complex data sets that include multi-angle hyperspectral imagery. Extra efforts were made to provide the best estimates by orthorectifying with an orbital model and producing an atmospheric correction using a DEM. In the end, reliable results were produced with more basic approaches. Performing detailed field work that mimicked the incoming data provided a better understanding of the data sets produced by the CHRIS sensor.

Having multi-angles and/or multi-date hyperspectral image improves the accuracy of forest species identification.

Both the CHRIS and 5-Scale spectra were able to provide inputs with the forest plot parameters into the PLS regression model. PLS provided a prediction tool to compare an unknown spectrum with a dependent forest parameter, as well as insights into the location of the contributions of the spectra, in both the spectral and angular domain. Recommendations for sensor characteristics for the various forest parameters evaluated

are 1) hyperspectral as the input spectra requires some type of derivative transformation, 2) multiple near nadir view angles as many of the coefficients clusters were located in the CHRIS's ±36° and nadir view angles.

CHRIS data of the GVWD has produced good model outputs to estimate forest structural parameters: Biomass (82%), Gap fraction (83%), LAI (87%), Crown Radius (93%), Height (87%) and Stem Density (93%)

6.7. Future Work

There were many exploration opportunities of the rich data sets available for and produced by this study. Not all of the datasets were fully examined in a comprehensive study due mainly to the exponential nature of the combinations and permutations which would never let this study end. For example, inputs spectra analyzed using the PLS model was restricted to complete inputs of all bands from all angles available from both 5-Scale outputs and processed CHRIS acquisitions. It was determined that processing subsets of these data in PLS highlighted the same regions of the spectra that contributed to the dependent forest parameter. However, the complete set of spectral transformations could be further explored to determine the optimum parameter. This could be accomplished by concatenating spectra from all angles and all transformation for each plot into the PLS model. Further study could also attempt to produce a map product of each forest parameter explored by applying for every forest pixel in an image either an inverse of the 5-scale model or the prediction from PLS. The methods developed in this study are also applicable to other forested areas to help determine the stability of the spectral locations affected by various forest parameters.

The methods developed here could be used to explore structural information from angular data in: other forest types, other geographic locations and other disciplines (such as agriculture). There is potential to apply these PLS coefficients to CHRIS data collected on similar forested areas to extend the forest structure predictability.

Bibliography

Alonso, L. and J. Moreno (2004). Quasi-Automatic Geometric Correction and Related Geometric Issues in the Exploitation of CHRIS/Proba Data. 2nd CHRIS/Proba Workshop, Frascati, Italy, ESA/ESRIN.

Asner, G. P. (2000). "Contributions of Multi-view Angle Remote Sensing to Land-surface and Biogeochemical Research." Remote Sensing Reviews **18**: 137-162.

Asner, G. P., B. H. Braswell, D. S. Schimel and C. A. Wessman (1998). "Ecological Research Needs from Multiangle Remote Sensing Data." Remote Sensing of Environment **63**(2): 155-165.

Bacour, C. and F.-M. Bron (2005). "Variability of biome reflectance directional signatures as seen by POLDER." Remote Sensing of Environment **98**(1): 80-95.

Barnsley, M. J., D. Allison and P. Lewis (1997). "On the information content of multiple view angle (MVA) images." International Journal of Remote Sensing **18**(9): 1937-1960.

Barnsley, M. J., J. J. Settle, M. A. Cutter, D. R. Lobb and F. Teston (2004). "The PROBA/CHRIS mission: a low-cost smallsat for hyperspectral multiangle observations of the Earth surface and atmosphere." IEEE Transactions on Geoscience and Remote Sensing **42**(7): 1512-1520.

Beddows, D. (2002). Levels-Of-Growing-Stock Cooperative Study in Douglas-fir: Report No. 16 – Sayward Forest and Shawnigan Lake. Information Report BC-X-393. Victoria, BC, Pacific Forestry Centre.

Bhogal, P., D. G. Goodenough, F. Gougeon, N. Daley, A. Nera and O. Niemann (1998). Fusion Of AIRSAR And MEIS Data For Estimating Forest Parameters. IGARSS'98, Seattle, WA. vol.3: 1314 - 1317

Brix, H. (1993). Fertilization and Thinning Effect on a Douglas-fir Ecosystem at Shawnigan Lake: A Synthesis of Project Results. FRDA Report. C.-B. C. P. A. o. F. R. D. F. II. Victoria, BC, Pacific Forestry Centre.

Bruegge, C. J., N. L. Chrien, R. R. Ando, D. J. Diner, W. A. Abdou, M. C. Helmlinger, S. H. Pilorz and K. J. Thome (2002). "Early validation of the Multi-angle Imaging SpectroRadiometer (MISR) radiometric scale." Geoscience and Remote Sensing, IEEE Transactions on **40**(7): 1477-1492.

CFS, C. F. S. (2006). The State of Canada's Forests 2005 - 2006. N. R. Canada, Government of Canada.

Chen, J. M. and J. Cihlar (1997). "A hotspot function in a simple bidirectional reflectance model for satellite applications." Journal of Geophysical Research **102**(25): 907-913.

Chen, J. M. and S. G. Leblanc (1997). "A four-scale bidirectional reflectance model based on canopy architecture." Geoscience and Remote Sensing, IEEE Transactions on **35**(5): 1316-1337.

Chen, J. M., S. G. Leblanc, J. R. Miller, J. Freemantle, S. E. Loechel, C. L. Walthall, K. A. Innanen and H. P. White (1999). "Compact Airborne Spectrographic Imager (CASI) used for mapping biophysical parameters of boreal forests " Journal of geophysical research **104**(D22): 27945-27958.

Chen, J. M., J. Liu, S. G. Leblanc, R. Lacaze and J.-L. Roujean (2003). "Multi-angular optical remote sensing for assessing vegetation structure and carbon absorption." Remote Sensing of Environment **84**(4): 516-525.

Cheng, P. (2007). "Orthorectifying CHRIS data using Orthoengine Generic Image", PCI Geomatics Inc, Per comm.. A. Dyk. Victoria.

Coops, N. C., M. L. Smith, M. E. Martin and S. V. Ollinger (2003). "Prediction of eucalypt foliage nitrogen content from satellite-derived hyperspectral data." Geoscience and Remote Sensing, IEEE Transactions on **41**(6): 1338.

Curran, P. J. (1989). "Remote Sensing of Foliar Chemistry." Remote Sensing of Environment **30**: 271-278.

Curran, P. J., J. L. Dungan and D. L. Peterson (2001). "Estimating the foliar biochemical concentration of leaves with refectance spectrometry." Remote Sensing of Environment **76**: 349-359.

Cutter, M. A. (2002). CHRIS Image Data Information**:** 3.

Cutter, M. A. (2005). CHRIS Data Format**:** 31.

Dawson, T. P., P. J. Curran, P. R. J. North and S. E. Plummer (1999). "The Propagation of Foliar Biochemical Absorption Features in Forest Canopy Reflectance: A Theoretical Analysis." Remote Sensing of Environment **67**: 147–159.

Dawson, T. P., P. J. Curran and S. E. Plummer (1998). "LIBERTY—Modeling the Effects of Leaf Biochemical Concentration on Reflectance Spectra " Remote Sensing of Environment **65**: 50-60.

Diner, D. J., G. P. Asner, R. Davies, Y. Knyazikhin, J. P. Muller, A. W. Nolin, B. Pinty, C. B. Schaaf and J. Stroeve (1999). "New directions in Earth observing: scientific application of multi-angle remote sensing." Bulletin of the American Meteorological Society **80**(11): 2209– 2228.

Diner, D. J., J. C. Beckert, G. W. Bothwell and J. I. Rodriguez (2002). "Performance of the MISR instrument during its first 20 months in Earth orbit." Geoscience and Remote Sensing, IEEE Transactions on **40**(7): 1449-1466.

Dyk, A., D. Goodenough, J. Li, K. Niemann, A. Guan, H. Chen and J. Duong (2006). Multi-Temporal, Multi-Angle Evaluation with CHRIS of Coastal Forests. IGARSS'06, Denver, CO. 108 – 111.

Dyk, A., D. G. Goodenough, A. S. Bhogal, J. Pearlman and J. Love (2002). Geometric correction and validation of Hyperion and ALI data for EVEOSD. IGARSS'02, Toronto, Canada. **1**: 579 - 583

Gao, F., C. B. Schaaf, A. H. Strahler, Y. Jin and X. Li (2003). "Detecting vegetation structure using a kernel-based BRDF model." Remote Sensing of Environment **86**: 198-205.

García, J. C., C. Cuñat and J. Moreno (2006). Improvements In The Removal Of Vertical Striping In Chris/Proba Images. 4th CHRIS Proba workshop, Session 1: CHRIS Image Processing & Validation. M. Cutter and L. Guanter. ESRIN, Frascati - Italy.

Garcia, J. C. and J.Moreno (2004). Removal of Noises in CHRIS/PROBA Images: Application to the Sparc Campaign Data. 2nd CHRIS/PROBA Workshop 2004. Frascati, Italy.

Gastellu-Etchegorry, J. P. and V. Bruniquel-Pinel (2001). "A modeling approach to assess the robustness of spectrometric predictive equation for canopy chemistry." Remote Sensing of Environment **76**(1): 1-15.

Gerstl, S. A. W. (1996). Angular signatures, and a space-borne measurement concept.

Getzin, S., C. Dean, F. He, J. A. Trofymow, K. Wiegand and T. Wiegand (2006). "Spatial patterns and competition of tree species in a Douglas-fir chronosequence on Vancouver Island." Ecography **29**: 671-682.

Goel, N. S. and R. L. Thompson (2000). "A snapshot of Canopy Reflectance Models and a Universal Model for the Radiation Regime." Remote Sensing Reviews **18**: 197-206.

Goodenough, D. G., A. Dyk, K. O. Niemann, J. S. Pearlman, H. Chen, T. Han, M. Murdock, and C. West (2003). "Processing Hyperion and ALI for Forest Classification." IEEE Transactions on Geoscience and Remote Sensing. **41**(6): 1321 - 1331.

Goodenough, D. G., D. Charlebois, P. Bhogal, M. Heyd, S. Matwin, O. Niemann and F. Portigal (1995). Knowledge-Based Imaging Spectrometer Analysis and GIS for Forestry. IGARSS'95, Florence, Italy. **1**: 464 - 467

Goodenough, D. G., A. Dyk, T. Han and H. Chen (2005a). HUDFA/HUDFEMA Project Reports. C. F. S. Natural Resources Canada.

Goodenough, D. G., A. Dyk, T. Han, H. Chen, T. Gates and K. O. Niemann (2005b). Multi-temporal evaluation with CHRIS of coastal forests, IGARSS'05, Seoul, Korea. **5**: 3557 – 3560.

Goodenough, D. G., T. Han and A. Dyk (2005c). Hyperspectral Forest Products. Workshop on Resource and Environmental Hyperspectral Monitoring Products, Victoria BC.

Goodenough, D. G., A. Dyk and K. O. Niemann (2006). "Evaluation and Validation of CHRIS for National Forests (EVC) Project." 4th ESA CHRIS PROBA Workshop 2006, Frascati, Italy.

Government of Canada (2005). A Plan for Honouring our Kyoto Commitment. Moving Forward on Climate Change. Climate Change Canada.

Guanter, L., L. Alonso and J. Moreno (2005). "A method for the surface reflectance retrieval from PROBA/CHRIS data over land: application to ESA SPARC campaigns." Geoscience and Remote Sensing, IEEE Transactions on **43**(12): 2908-2917.

Jacquemoud, S. and F. Baret (1990). "PROSPECT: A model of leaf optical properties spectra." Remote Sensing of Environment **34**(2): 75-91.

Johnson, G. (2005). Growth Model Runoff II, Weyerhaeuser Company.

Kayitakire, F. and P. Defourny (2004). Forest Type Discrimination Using Multi-Angle Hyperspectral Data. Second Chris Proba Workshop, Frascati, Italy, ESA.

Kemp, W. (1991). Organic Spectroscopy. London, Macmillan.

Kneubühler, M., B. Koetz, R. Richter, M. Schaepman and K. Itten (2005). Geometric And Radiometric Pre-Processing Of Chris/Proba Data Over Mountainous Terrain. Third CHRIS/Proba Workshop, ESRIN, Frascati, Italy, ESTEC.

Lacaze, R., J. M. Chen, J.-L. Roujean and S. G. Leblanc (2002). "Retrieval of vegetation clumping index using hot spot signatures measured by POLDER instrument." Remote Sensing of Environment **79**(1): 84-95.

Leblanc, S. G., P. Bicheron, J. M. Chen, M. Leroy and J. Cihlar (1999). "Investigation of directional reflectance in boreal forests with an improved four-scale model and airborne POLDER data." Geoscience and Remote Sensing, IEEE Transactions on **37**(3): 1396-1414.

Leblanc, S. G., J. M. Chen, H. P. White, R. Latifovic, R. Fernandes, J. L. Roujean and R. Lacaze (2002). Mapping leaf area index heterogeneity over Canada using directional reflectance and anisotropy canopy reflectance models.

Lewis, P. (1999). "Three-dimensional plant modelling for remote sensing simulation studies using the Botanical Plant Modelling System." Agronomie - Agriculture and Environment **19**: 185-210.

Li, X., A. H. Strahler and C. E. Woodcock (1995). "A hybrid geometric optical-radiative transfer approach for modeling albedo and directional reflectance of discontinuous canopies." Geoscience and Remote Sensing, IEEE Transactions on **33**(2): 466-480.

Lim, K. S. and P. M. Treitz (2004). Estimation of Aboveground Forest Biomass Using Airborne Scanning Discrete Return LIDAR in Douglas-fir. ISPRS working group VIII/2 'Laser-Scanners for Forest and Landscape Assessment', Freiburg, Germany, International Society of Photogrammetry and Remote Sensing.

Loos, R. and O. Niemann (2006). Identification of Individual Trees And Canopy Shapes using LIDAR Data for Fire Management. IGARSS'06, Denver, Colorado, IEEE Geoscience and Remote Sensing Society.

Mackinney, G. (1941). "Absorption of light by chlorophyll solutions." Journal of Biology Chemistry **140**: 315-322.

Magnussen, Steen (2006), "Calculating Variance Equation", Natural Resources Canada, *Per Comm*, November 21, 2006

Martin, M. E., S. D. Newman, J. D. Aber and R. G. Congalton (1998). "Determining Forest Species Composition Using High Spectral Resolution Remote Sensing Data." Remote Sensing of Environment **65**: 249–254.

Melamed, M. T. (1963). "Optical properties of powders. Part I. Optical absorption coefficients and the absolute value of the diffuse reflectance. ." Journal of Applied Physics **34**: 560-570.

Naesset, E. (2004). Estimation of Above- and Below-Ground Biomass in Boreal Forest Ecosystems. SPRS working group VIII/2 'Laser-Scanners for Forest and Landscape Assessment', Freiburg, Germany, International Society of Photogrammetry and Remote Sensing.

Niemann, K. O. (1995). "Remote Sensing of Forest Stand Age Using Airborne Spectrometer Data." Photogrammetric Engineering and Remote Sensing **91**(9): 1119-1127.

Niemann, K. O., R. Loos, D. G. Goodenough and A. Dyk (2005). Integration of LiDAR-based metrics with AVIRIS hyperspectral data: An exploration of the effects of canopy structure on canopy reflectance. 26th Canadian Remote Sensing Symposium, Toronto. June 14-16, 2005 CD Proceedings.

Nolin, A. W. (2004). "Towards retrieval of forest cover density over snow from the Multi-angle Imaging SpectroRadiometer (MISR)." Hydrological Processes **18**: 3623–3636.

Pinty, B., N. Gobron, J.-L. Widlowski, S. A. W. Gerstl, M. M. Verstraete, M. Antunes, C. Bacour, F. Gascon, J.-P. Gastellu, N. Goel, S. Jacquemoud, P. North, W. Qin and R. Thompson (2001). "Radiation transfer model intercomparison (RAMI) exercise." Journal Of Geophysical Research **106**(D11): 11937-11956.

Pinty, B., J.-L. Widlowski, M. Taberner, N. Gobron, M. M. Verstraete, M. Disney, F. Gascon, J.-P. Gastellu, L. Jiang, A. Kuusk, P. Lewis, X. Li, W. Ni-Meister, T. Nilson, P. North, W. Qin, L. Su, S. Tang, R. Thompson, W. Verhoef, H. Wang, J. Wang, G. Yan and H. Zang (2004). "Radiation Transfer Model Intercomparison (RAMI) exercise: Results from the second phase." Journal Of Geophysical Research **109**(D06210): 1-19.

Research Systems Inc. (2004, September). "FLAASH User's Guide." Version 4.1.

Riaño, D., E. Meierc, B. Allgower, E. Chuvieco and S. L. Ustin (2003). "Modeling airborne laser scanning data for the spatial generation of critical forest parameters in fire behavior modeling." Remote Sensing of Environment **86**: 177-186.

Richter, R. (2007). Atmospheric / Topographic Correction for Satellite Imagery ATCOR-2/3 User Guide, Version 6.3, January 2007. R. S. D. C. DLR - German Aerospace Center. Wessling / Germany.

Schaepman, M. E., B. Koetz, G. Schaepman-Strub and K. I. Itten (2004). "Spectrodirectional remotes sensing for the improved estimation of biophysical and -chemical variables: two case studies." International Journal of Applied Earth Observation and Geoinformation **6**: 271-282.

Schlerf, M., C. Atzberger, M. Vohland, H. Buddenbaum, S. Seeling and J. Hill (2004). "Derivation Of Forest Leaf Area Index From Multi- And Hyperspectral Remote Sensing Data." European Association of Remote Sensing Laboratories **3**: 2004.

Settle, J. (2004). "On the dimensionality of multi-view hyperspectral measurements of vegetation." Remote Sensing of Environment **90**(2): 235-242.

Shenk, J. S. and M. O. Westerhaus (1991). "Population Structuring of Near Infrared Spectra and Modified Partial Least Squares Regression." Crop Science **31**(b): 1548-1555.

Simic, A., J. M. Chen and T. L. Noland (2010) "Retrieval of forest chlorophyll conent using canopy structure parameters derived from multi-angle data: the measurement concept of combining nadir byperspectal and off-nadir multipsectal data" International Journal of Femote Sensing (in press).

Skole, D. L. and J. Qi (2001). Optical remote Sensing For Monitoring Forest And Biomass Change In The Context Of The Kyoto Protocol. GCGEO Research Advances. East Lansing, Michigan, Michigan State University. RA01-01\w.

Smith, J. E., L. S. Heath and J. C. Jenkins (2003). Forest Volume-to-Biomass Models and Estimates of Mass for Live and Standing Dead Trees of U.S. Forests. USDA Forest Service, Northeastern Research Station. General Technical Report NE-298**:** 62.

Smith, M.-L. and M. E. Martin (2001). "A Plot-Based Method For Rapid Estimation Of Forest Canopy Chemistry." Canadian Journal for Remote Sensing **31**: 549-555.

Smith, M.-L., M. E. Martin, L. Plourde and S. V. Ollinger (2003). "Analysis of hyperspectral data for estimation of temperate forest canopy nitrogen concentration: comparison between an airborne (AVIRIS) and a spaceborne

(Hyperion) sensor." Geoscience and Remote Sensing, IEEE Transactions on **41**(6): 1332.

Smith, M.-L., S. V. Ollinger, M. E. Martin, J. D. Aber, R. A. Hallett and C. L. Goodale (2002). "Direct Estimation Of Above Ground Forest Productivity Through Hyperspectral Remote Sensing Of Canopy Nitrogen." Ecological Applications **12**(5): 1286-1302.

Song, A. (2005). Nonlinear Regression. J. Gour and A. Dyk. Victoria. *Per Comm.*

Temesgen, H., V. LeMay and S. J. Mitchell (2005). "Tree crown ratio models for multi-species and multi-layered stands of southeastern British Columbia." The Forestry Chronicle **81**(1): 133-141.

Ter-Mikaelian, M. T. and M. D. Korzukhin (1997). "Biomass equations for sixty five North American tree species." For. Ecolology and Managment **97**: 1-24.

Tobias, R. D. (1995). An Introduction to Partial Least Squares Regression, SAS Institute Inc., Cary, NC**:** 1-8.

Toutin, T. (2004). "Geometric processing of remote sensing images: models, algorithms and method." International Journal of Remote Sensing **25**(10): 1893-1924.

Toutin, T. and Y. Carbonneau (1992). "MOS and SEASAT image geometric corrections." IEEE Transactions on Geoscience and Remote Sensing **30**(3): 603-609.

Treitz, P. M. and P. J. Howarth (1999). "Hyperspectral remote sensing for estimating biophysical parameters of forest ecosystems." Progress in Physical Geography **23**(3): 359-390.

Wenge, N., L. Xiaowen, C. E. Woodcock, M. R. Caetano and A. H. Strahler (1999). "An analytical hybrid GORT model for bidirectional reflectance over discontinuous plant canopies." Geoscience and Remote Sensing, IEEE Transactions on **37**(2): 987-999.

White, H. P., J. R. Miller and J. M. Chen (2001). "Four-Scale Linear Model for Anisotropic Reflectance (FLAIR), I. Model Description and Partial Validation." IEEE Trans. GeoSci. Remote Sens **39**(5): 1072-1083.

Wulder, M. (1998). "Optical remote-sensing techniques for the assessment of forest inventory and biophusical parameters." Progress in Physical Geography **22**(4): 449-476.

Zarco-Tejada, P. J. and S. L. Ustin (2001). Modeling canopy water content for carbon estimates from MODIS data at land EOS validation sites. IGARSS'01, Sydney, NSW. **1**: 342-344.

Appendix 1 - Running 5-Scale

To run the 5-scale model, a spread sheet was created with all the plot parameters listed in a column, one column for each plot (*5-Scaleinput.xls*). The batch file requires an input parameter file called sample.txt for each plot, so a separate text file is created for each plot by copy and pasting the parameter name column and the corresponding plot parameters into an appropriately named text file. The column is deleted and the copy and paste is repeated for the next plot. This produces 18 input text files named: "*Plot??in.txt*" where *??* represents the plot number. The batch file "*5-Scale_em.bat*" temporarily copies each of these files to "*sample.txt*" and then calls the 5-Scale command line executable file. All output destined for the screen is redirected to "*5-Scale-em_Out.txt*" and the output from each plot is stored in the appropriate text file with the following naming convention "*Plot??out.txt*".

After the batch files run for the current configuration of parameters, the input and output text files are copied into a new directory. The output file should be read through to validate that all runs were successful. An output like "`Simulation 4 of 15 (VZA= 40.50 PHI= -8.00 SZA= 47.40)`" illustrates a successful run, while "`BRDF may not be calculated correctly(PG at vza = 58.2 deg.)`" indicates the model did not execute successfully. The template spreadsheets "*5-ScaleOutput_V8_p1.xls*" and "*5-ScaleOutput_V8_p2.xls*" each contain plots of the output spectra. Using the "Refresh Data" option on the *Plot??Out* tabs (Cell A33), the 5-Scale output is ingested into the spreadsheet. Formulas link to this data to produce the graphs of shadow and sunlight portions of foliage and ground, as well as the spectral plots in the subsequent tabs.

Appendix 2 – Average R^2 from 5-Scale Spectral combinations

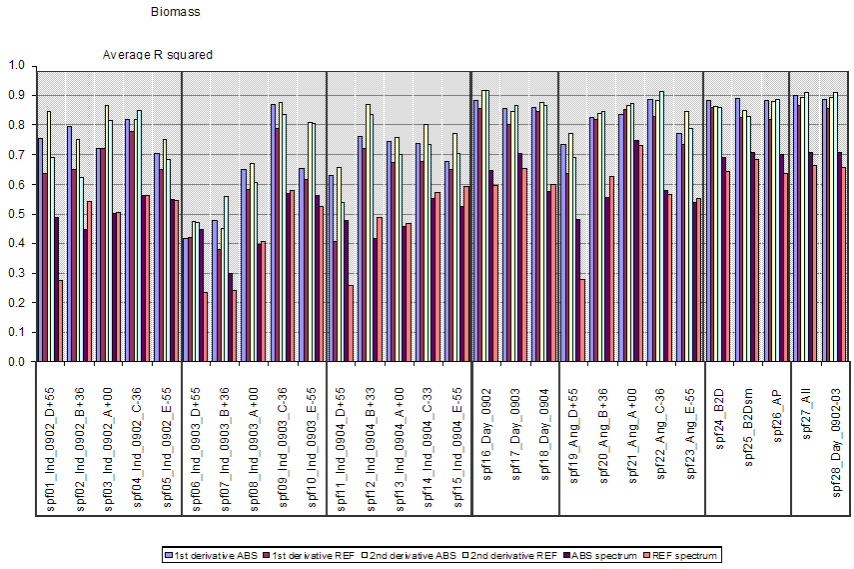

Figure A2-1. Average R^2 for Biomass from 5-Scale Spectral combinations.

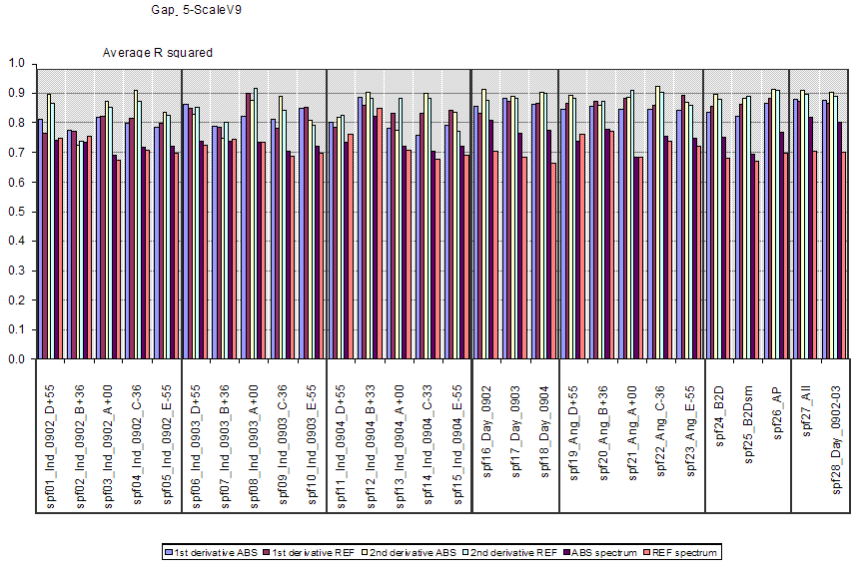

Figure A2-2. Average R^2 for GAP5-Scale Spectral combinations.

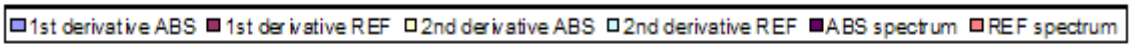

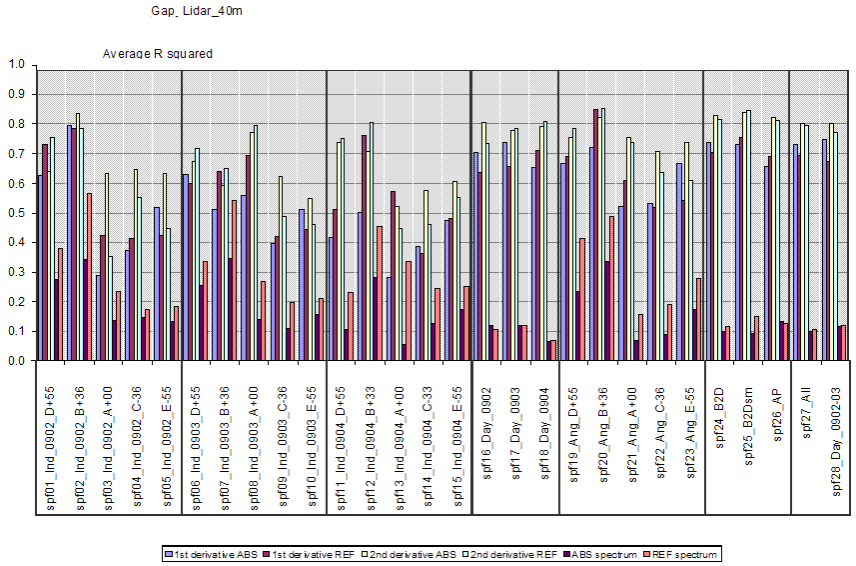

Figure A2-3. Average R^2 for GAPLIDAR from 5-Scale Spectral combinations.

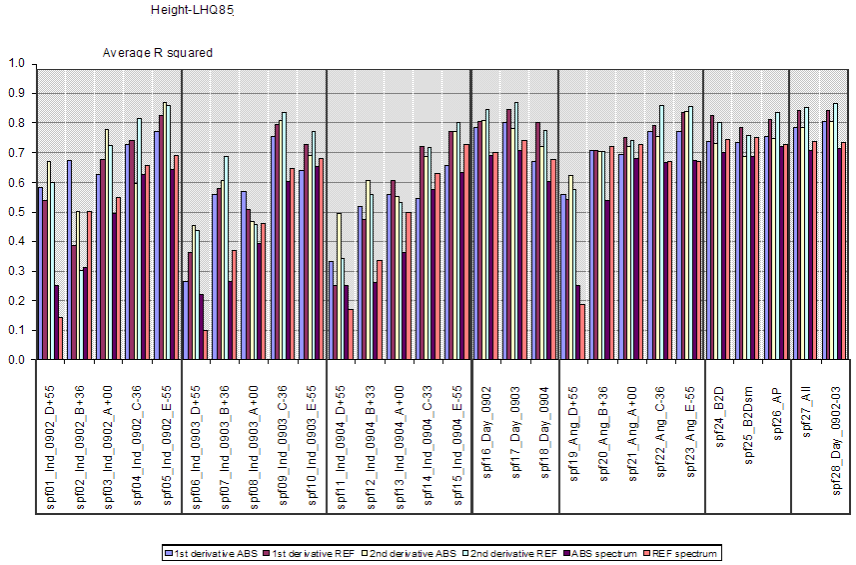

Figure A2-4. Average R^2 for Height from 5-Scale Spectral combinations.

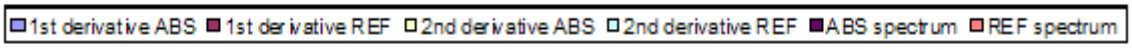

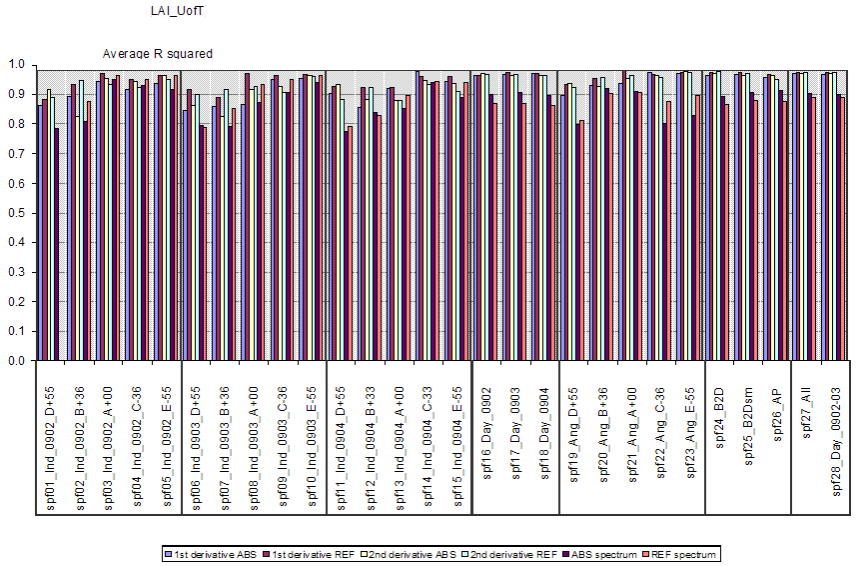

Figure A2-5. Average R^2 for LAI from 5-Scale Spectral combinations.

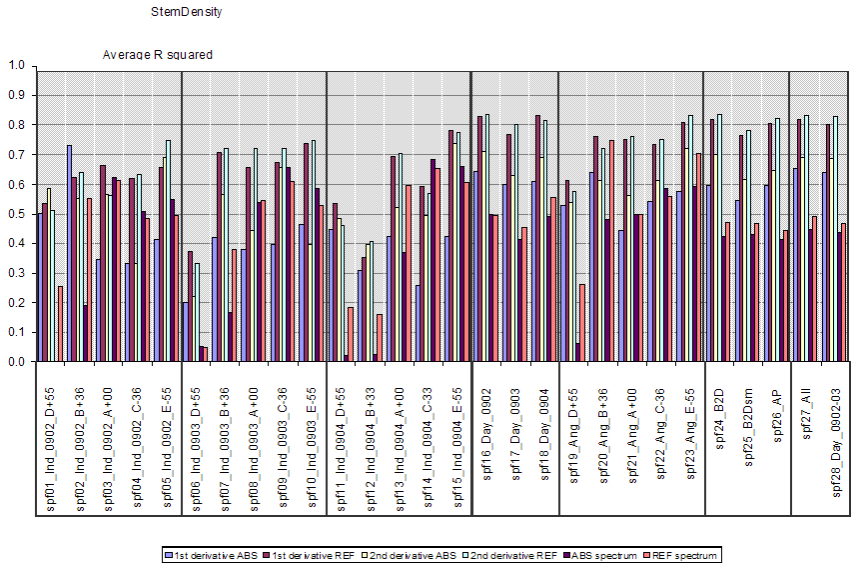

Figure A2-6. Average R2 for Stem Density from 5-Scale Spectral combinations.

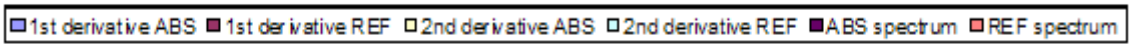

Appendix 3 – Visual Python Code for Coefficient Viewing

The following code was writing using Visual Python (VPython-Win-Py2.5-3.2.1) in order to visualize the PLS coefficients for all wavelengths and view angles.

```
#=============================================================================================
# coefficient3D.py
# ADyk 2009/06/14
# Visualize the output from hyperspectral_results v5.xls as stored in text files listed
# below
#
# Sample input Text File two column format (no headers):
# 0902_D+55_0411 0.139991017
# 0902_D+55_0443 0.195109399
# 0902_D+55_0453 0.197067002
# 0902_D+55_0463 0.013789181
# ...
# Where column 1 is key string of date(MMDD)_FZA_Lammbda
# and column 2 is the normaized absolute value of the PLS coefficient
#=============================================================================================

from visual.graph import * # import graphing features
from visual.text import *

#=============================================================================================
# Uncomment required Coefficients source file pointer

filename = 'Coeffients5-scaleBiomass.txt'
#filename = 'Coeffients5-scaleCrownRadius.txt'
#filename = 'Coeffients5-scaleGAP5Scale.txt'
#filename = 'Coeffients5-scaleGAPLIDAR.txt'
#filename = 'Coeffients5-scaleHeight.txt'
#filename = 'Coeffients5-scaleLAI.txt'
#filename = 'Coeffients5-scaleStemDensity.txt'
#filename = 'CoeffientsCHRISBiomass.txt'
#filename = 'CoeffientsCHRISCrownRadius.txt'
#filename = 'CoeffientsCHRISGAP.txt'
#filename = 'CoeffientsCHRISGAPLIDAR.txt'
#filename = 'CoeffientsCHRISHeight.txt'
#filename = 'CoeffientsCHRISLAI.txt'
#filename = 'CoeffientsCHRISStemDensity.txt'

#=============================================================================================
# Define scaling and dimensions of 3D graph.
L = 30  # Number of Angles scaled by 6                X
H = 63  # Number of Bands in CHRIS                    Y
W = 20  # Number of Days data is acquired scaled by 10 Z
scaleL = 5
scaleH = 1
scaleW = 5
#mdays = 2
numdays = 3

#=============================================================================================
# Visualized the graph
scene = display(title=filename, width=400,
                height=800, center=(L/2,H/2,W/2),
                background=(0.9,0.9,0.9))

#=============================================================================================
# Generate a "box", with opacity or outlines
# graphbox = box(pos = (L/2,H/2,W/2), opacity = 0.15, height = H, length = L, width=W )
BackWall = curve(pos=[(0,0),(0,H),(L,H),(L,0),(0,0)], color=color.red)
SideWall = curve(pos=[(0,0,0),(0,0,W),(0,H,W),(0,H,0),(0,0,0)], color=color.blue)
Floor = curve(pos=[(0,0,0), (L,0,0),(L,0,W), (0,0,W), (0,0,0)], color=color.green)
```

```
#=============================================================================================
# make a dictionary for days, angles and bands
angle = { 'D+55' : 1, 'B+36' : 2, 'A+00' : 3, 'C-36' : 4, 'E-55' : 5, 'B+33' : 2, 'C-33':4}
band = {'0411' : 1, '0443' : 2, '0453' : 3, '0463' : 4, '0473' : 5, '0483' : 6,
        '0492' : 7, '0501' : 8, '0511' : 9, '0522' : 10, '0532' : 11, '0542' : 12,
        '0554' : 13, '0564' : 14, '0574' : 15, '0584' : 16, '0593' : 17, '0606' : 18,
        '0616' : 19, '0625' : 20, '0635' : 21, '0644' : 22, '0654' : 23, '0665' : 24,
        '0676' : 25, '0684' : 26, '0690' : 27, '0696' : 28, '0702' : 29, '0708' : 30,
        '0714' : 31, '0720' : 32, '0726' : 33, '0733' : 34, '0740' : 35, '0746' : 36,
        '0753' : 37, '0760' : 38, '0768' : 39, '0775' : 40, '0782' : 41, '0790' : 42,
        '0798' : 43, '0806' : 44, '0814' : 45, '0834' : 46, '0847' : 47, '0856' : 48,
        '0865' : 49, '0874' : 50, '0883' : 51, '0892' : 52, '0902' : 53, '0912' : 54,
        '0922' : 55, '0931' : 56, '0947' : 57, '0962' : 58, '0973' : 59, '0983' : 60,
        '0994' : 61, '1005' : 62}
day = { '0902' : 1, '0903' : 2, '0904' : 3}

#=============================================================================================
# Add Origin Ball and Labels
origin = sphere(pos = (0,0,0), color=color.green, radius = 0.35)
label(pos=(0,H*1/63,0), text='411', color=color.white, box =0)
curve(pos=[(L,H*1/63,0),(0,H*1/63,0),(0,H*1/63,W)], color=color.blue)
label(pos=(0,H*8/63,0), text='501', color=color.white, box =0)
curve(pos=[(L,H*8/63,0),(0,H*8/63,0),(0,H*8/63,W)], color=color.blue)
label(pos=(0,H*15/63,0), text='574', color=color.white, box =0)
curve(pos=[(L,H*15/63,0),(0,H*15/63,0),(0,H*15/63,W)], color=color.blue)
label(pos=(0,H*23/63,0), text='654', color=color.white, box =0)
curve(pos=[(L,H*23/63,0),(0,H*23/63,0),(0,H*23/63,W)], color=color.blue)
label(pos=(0,H*31/63,0), text='714', color=color.white, box =0)
curve(pos=[(L,H*31/63,0),(0,H*31/63,0),(0,H*31/63,W)], color=color.blue)
label(pos=(0,H*38/63,0), text='760', color=color.white, box =0)
curve(pos=[(L,H*38/63,0),(0,H*38/63,0),(0,H*38/63,W)], color=color.blue)
label(pos=(0,H*46/63,0), text='834', color=color.white, box =0)
curve(pos=[(L,H*46/63,0),(0,H*46/63,0),(0,H*46/63,W)], color=color.blue)
label(pos=(0,H*54/63,0), text='912', color=color.white, box =0)
curve(pos=[(L,H*54/63,0),(0,H*54/63,0),(0,H*54/63,W)], color=color.blue)
label(pos=(0,H*62/63,0), text='1005', color=color.white, box =0)
curve(pos=[(L,H*62/63,0),(0,H*62/63,0),(0,H*62/63,W)], color=color.blue)


label(pos=(L*1/6,0,0), text='D+55', color=color.red,  box =0)
curve(pos=[(L*1/6,H,0),(L*1/6,0,0),(L*1/6,0,W)], color=color.red)
label(pos=(L*2/6,0,0), text='B+36', color=color.red,  box =0)
curve(pos=[(L*2/6,H,0),(L*2/6,0,0),(L*2/6,0,W)], color=color.red)
label(pos=(L*3/6,0,0), text='A+00', color=color.red,  box =0)
curve(pos=[(L*3/6,H,0),(L*3/6,0,0),(L*3/6,0,W)], color=color.red)
label(pos=(L*4/6,0,0), text='C-36', color=color.red,  box =0)
curve(pos=[(L*4/6,H,0),(L*4/6,0,0),(L*4/6,0,W)], color=color.red)
label(pos=(L*5/6,0,0), text='E-55', color=color.red,  box =0)
curve(pos=[(L*5/6,H,0),(L*5/6,0,0),(L*5/6,0,W)], color=color.red)


label(pos=(0,0,W*1/4), text='0902', color=color.green, box =0)
curve(pos=[(0,H,W*1/4),(0,0,W*1/4),(L,0,W*1/4)], color=color.green)
label(pos=(0,0,W*2/4), text='0903', color=color.green, box =0)
curve(pos=[(0,H,W*2/4),(0,0,W*2/4),(L,0,W*2/4)], color=color.green)
label(pos=(0,0,W*3/4), text='0904', color=color.green, box =0)
curve(pos=[(0,H,W*3/4),(0,0,W*3/4),(L,0,W*3/4)], color=color.green)


#=============================================================================================
# Input file format is from the spreadsheet "hyperspectral_results CHRIS.xls" or similar
# 012345678901234567890
# 0902_D+55_0411 0.9332232

openfile = open(filename, 'r')

#=============================================================================================
# For each line in file, plot point based on day, angle, band and coefficient
i = 0
#sumsidesLHW = zeros([5,62,3], Float) # Initialize an array to sum
```

```
sumsidesL = zeros([6], Float)  # Initialize an array to sum Length Angle X
sumsidesH = zeros([63], Float) # Initialize an array to sum Height Bands Y
sumsidesW = zeros([4], Float)  # Initialize an array to sum Width  Days  Z

for line in openfile:
    i = band[line[10:14]]+15
    rgb = color.hsv_to_rgb(( 1-(float(i)/77),1,1))
    curangle = angle[line[5:9]]  # extracted position of angle value in dictionary)
    curband  = band[line[10:14]] # extracted position of band value in dictionary)
    curday   = day[line[0:4]]    # extracted position of day value in dictionary)
    curcoef  = float(line[14:])
    #print "%d %s) %s=%d, %s=%d, %s=%d, %f" %(i, line, line[5:9],curangle, line[10:14],
curband,line[0:4],curday, float(line[14:]))
#    point =
sphere(pos=(angle[line[5:9]]*scaleW,band[line[10:14]]*scaleH,day[line[0:4]]*scaleL),
radius=float(line[14:]), color = rgb)
    point = ellipsoid(pos=(curangle*scaleW, curband*scaleH, curday*scaleL),
                  length=curcoef*scaleL, height=curcoef*1.5,width=curcoef*scaleW,
                  color = rgb)

    sumsidesL[curangle] = sumsidesL[curangle] + curcoef
    sumsidesH[curband]  = sumsidesH[curband]  + curcoef
    sumsidesW[curday]   = sumsidesW[curday]   + curcoef

# Plot the average of angle, band, day
counter = 1
while counter < 6:
    curavangle = sumsidesL[counter]/(62*numdays)
    print "Sum Len[%d] = %f AVG = %f" %(counter, sumsidesL[counter], curavangle)
    ellipsoid(pos=(counter*scaleL, H, W),
              length = curavangle*scaleL,
              height = curavangle*1.5,
              width  = curavangle*scaleW)
    counter = counter + 1

counter = 1
while counter < 63:
    curavband = sumsidesH[counter]/(5*numdays)
    print "Sum Height[%d] = %f AVG = %f" %(counter, sumsidesH[counter], curavband)
    ellipsoid(pos=(L, counter*scaleH, W),
              length = curavband*scaleL,
              height = curavband*1.5,
              width  = curavband*scaleW)
    counter = counter + 1

counter = 1
while counter < 4:
    curavday = sumsidesW[counter]/(62*5)
    print "Sum Width[%d] = %f AVG = %f" %(counter, sumsidesW[counter], curavday)
    ellipsoid(pos=(L, H, counter*scaleW),
              length = curavday*scaleL,
              height = curavday*1.5,
              width  = curavday*scaleW)
    counter = counter + 1
```

Appendix 4 – Visual Python Figures for Coefficient Viewing

Coefficients from PLS regression relating dependent variable from either 5-Scale or CHRIS shown using the Visual Python Script. Colours vary by wavelength (Z Axis) and the floor (X and Y Axis) shows the 15 possible locations of the CHRIS triplet. Outside gray are average coefficients.

Coeffients5-scaleBiomass: 2nd derivative rs:(2 points-left)

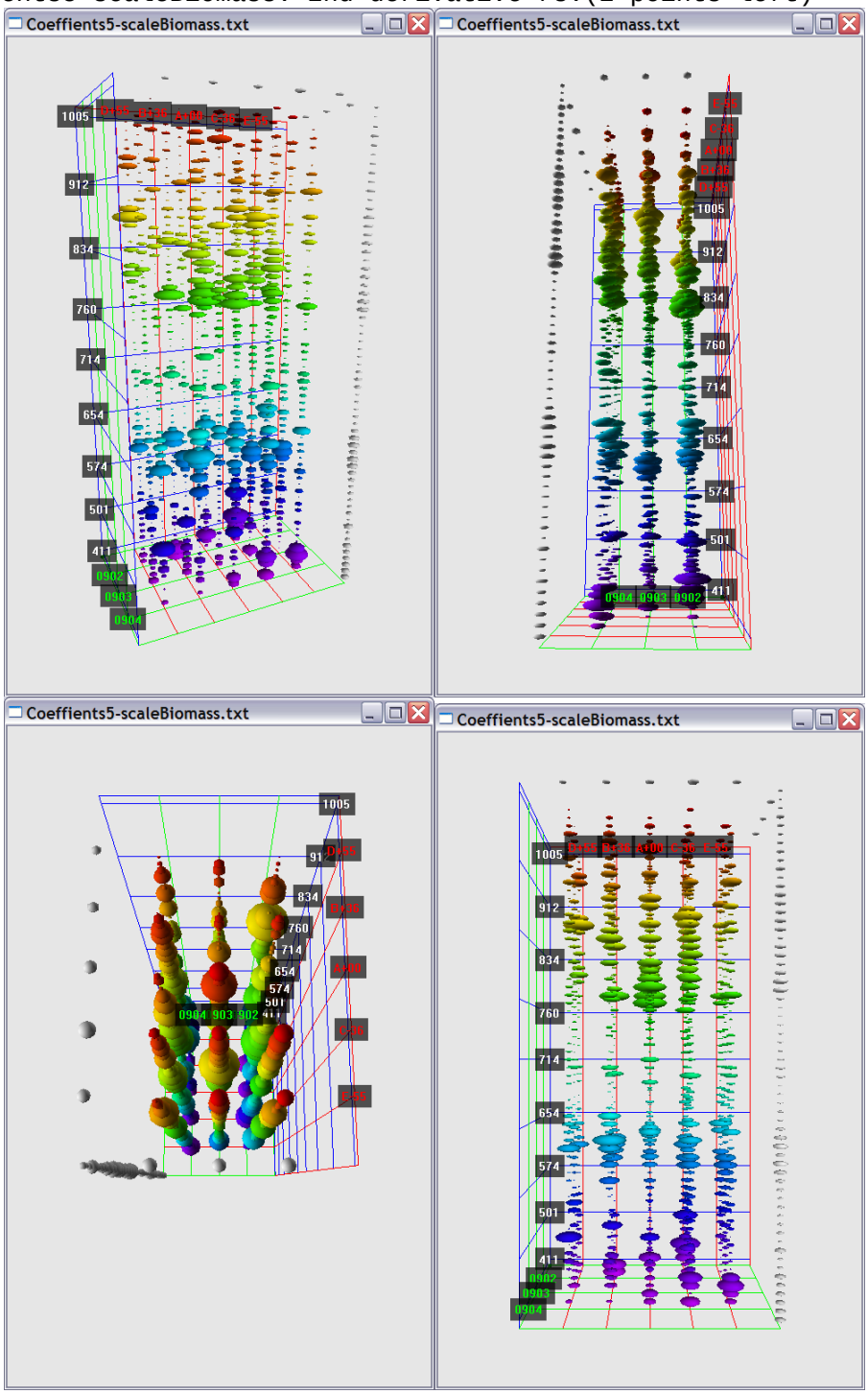

CoeffientsCHRISBiomass : 1st derivative as :(2 points-left)

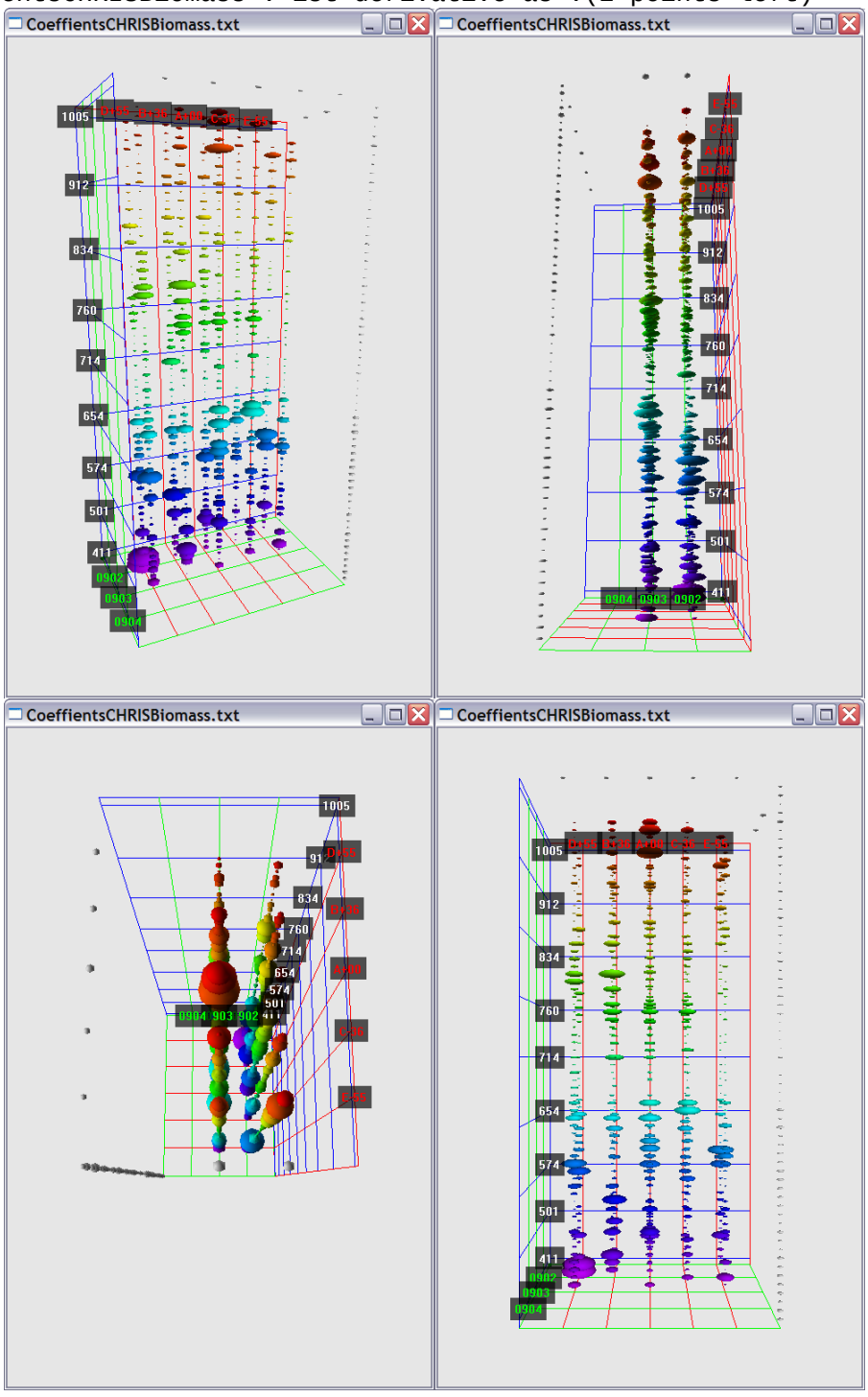

Coeffients5-scaleCrownRadius: 1st derivative as: (3 points-quadratic)

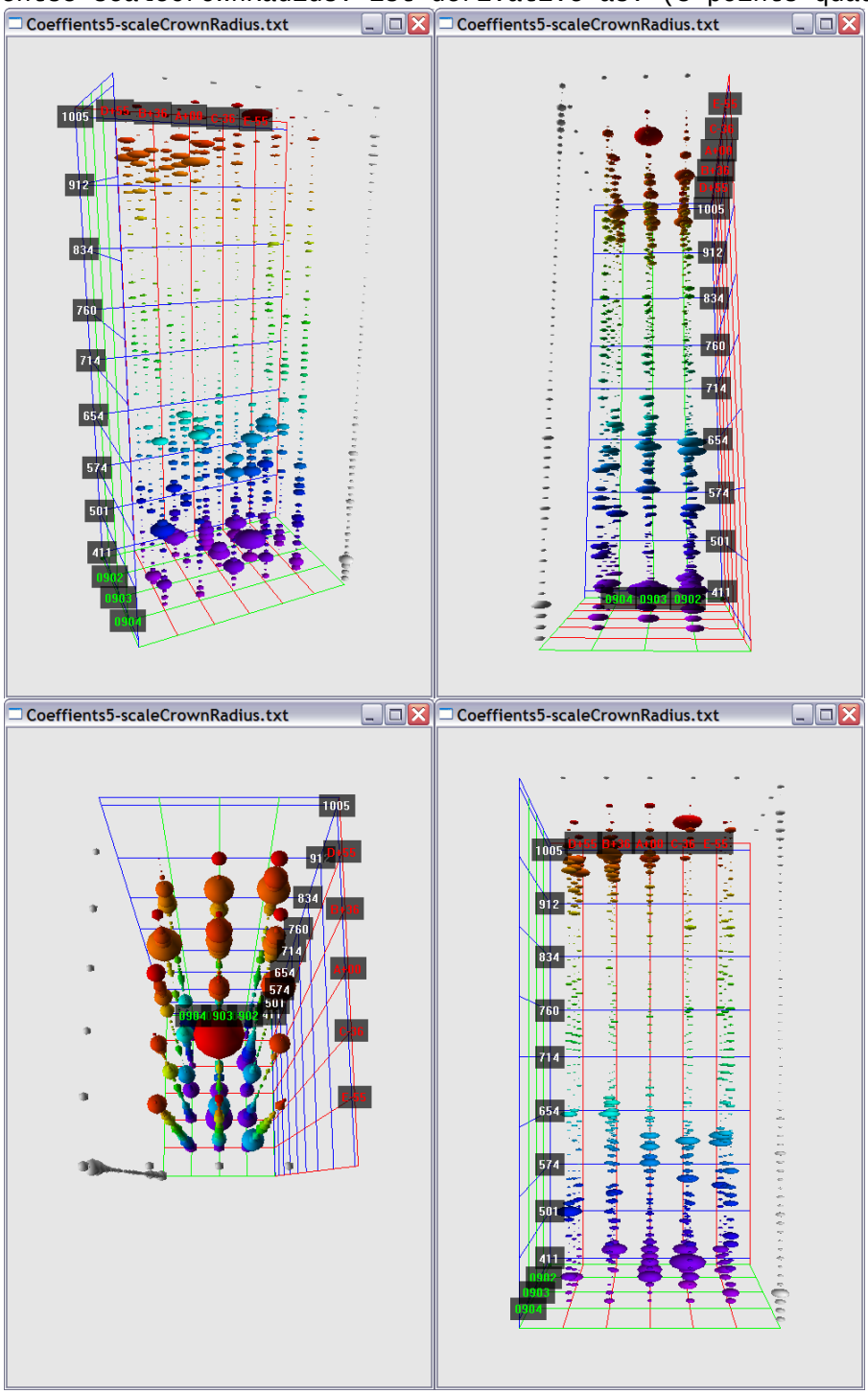

CoeffientsCHRISCrownRadius : 2nd derivative rs :(2 points-middle)

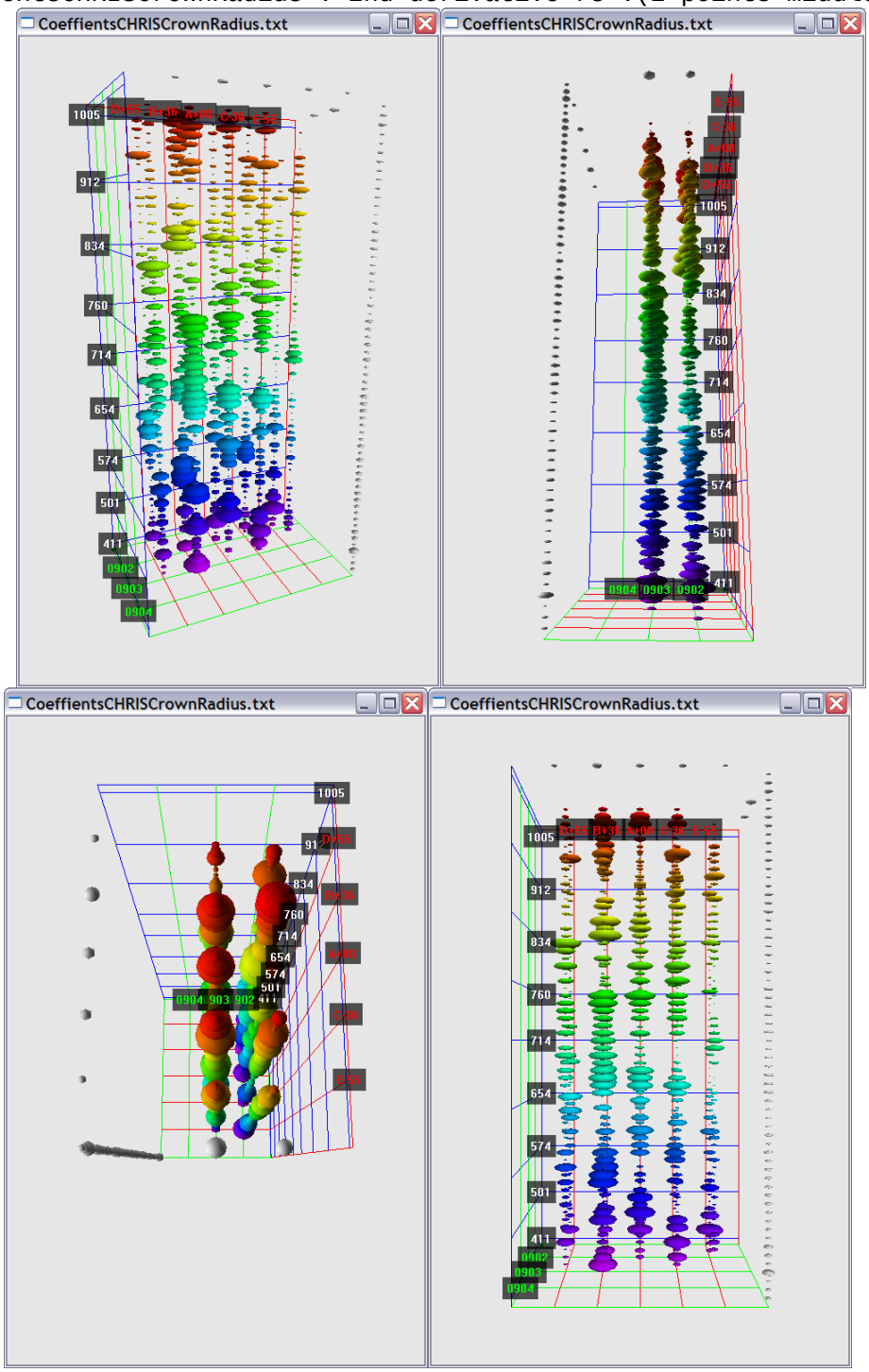

Coeffients5-scaleGAP5Scale : 2nd derivative rs :(2 points-left)

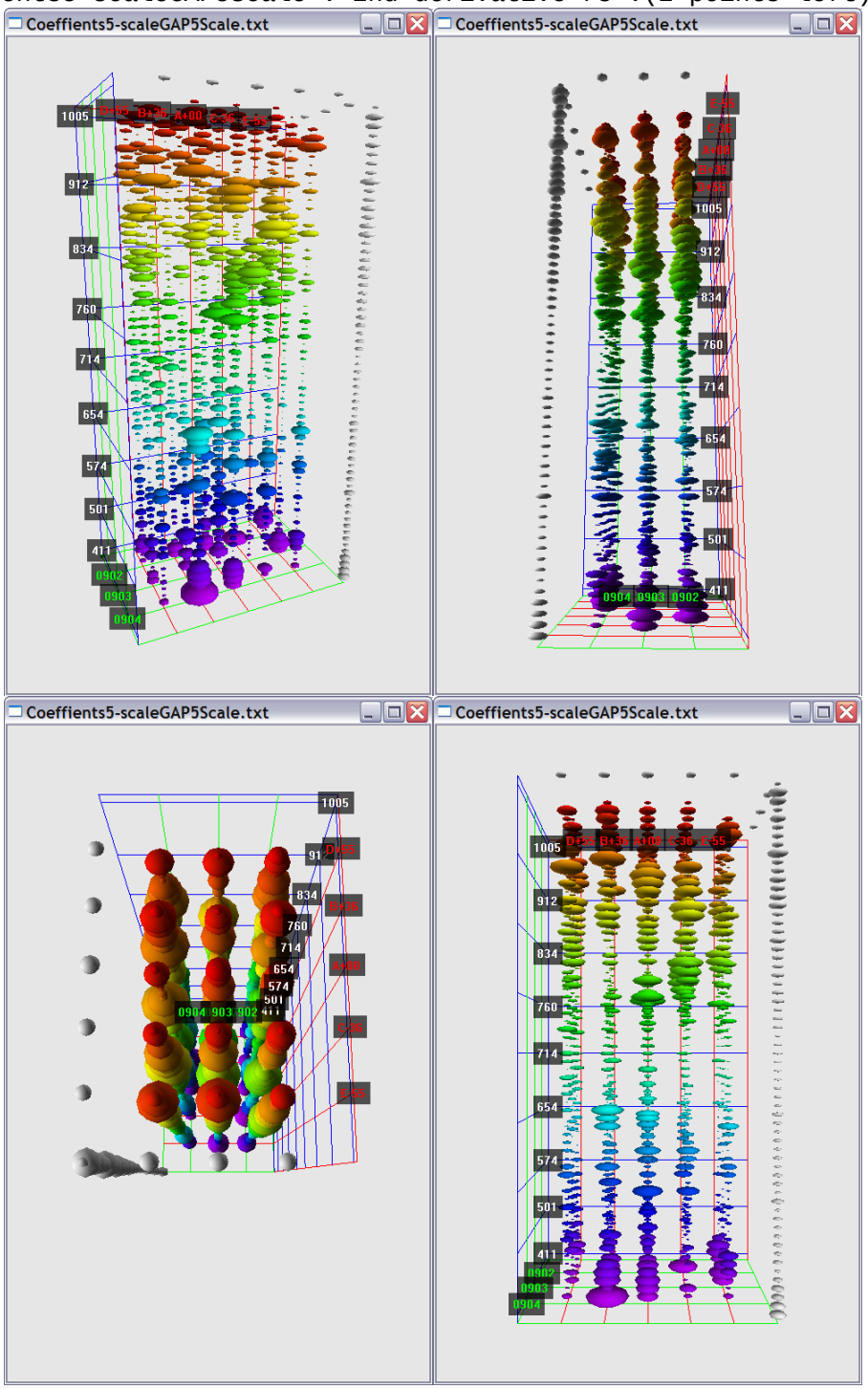

CoeffientsCHRISGAP.txt : 2nd derivative as : (2 points-left)

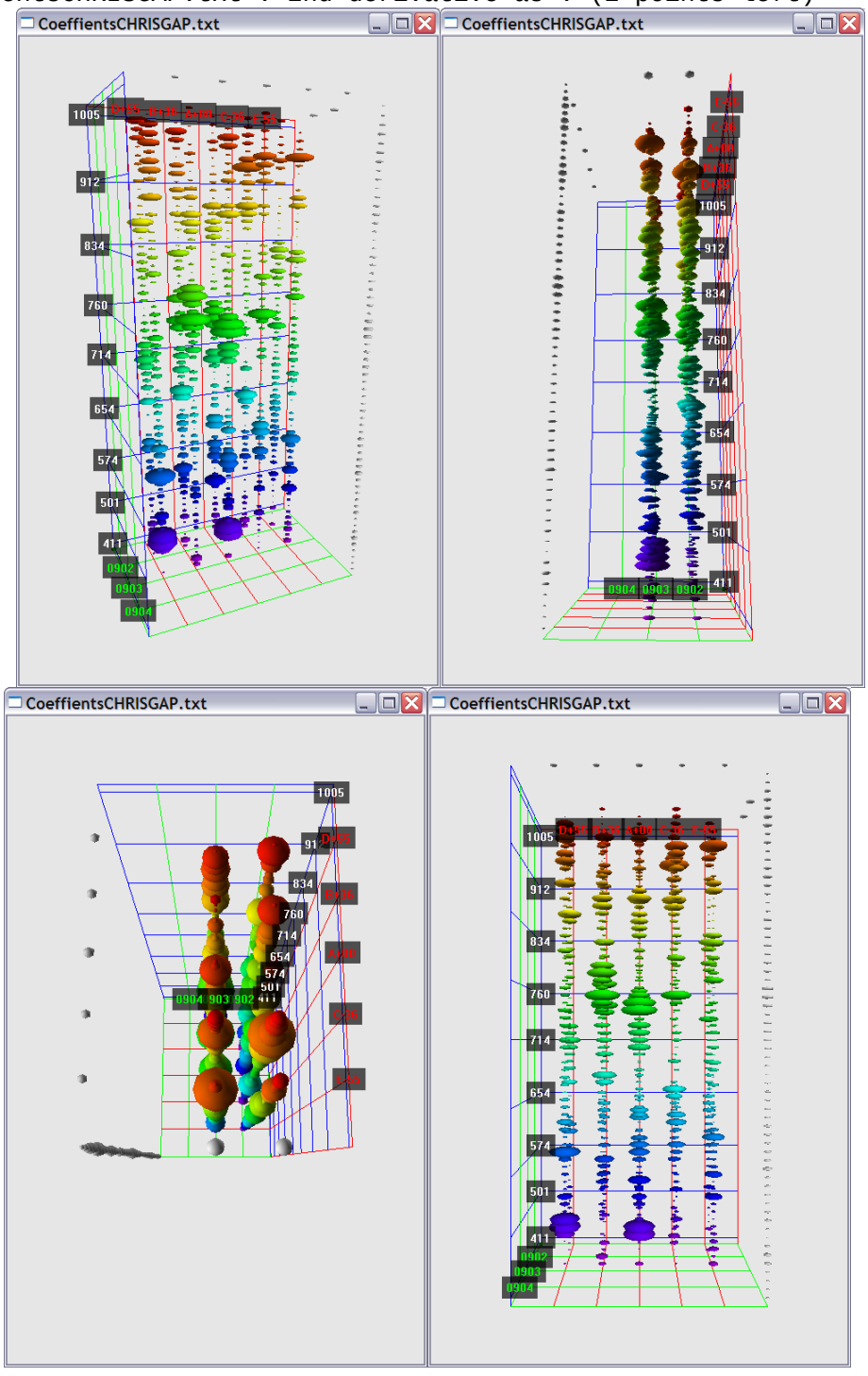

Coeffients5-scaleGAPLIDAR : 2nd derivative rs :(2 points-left)

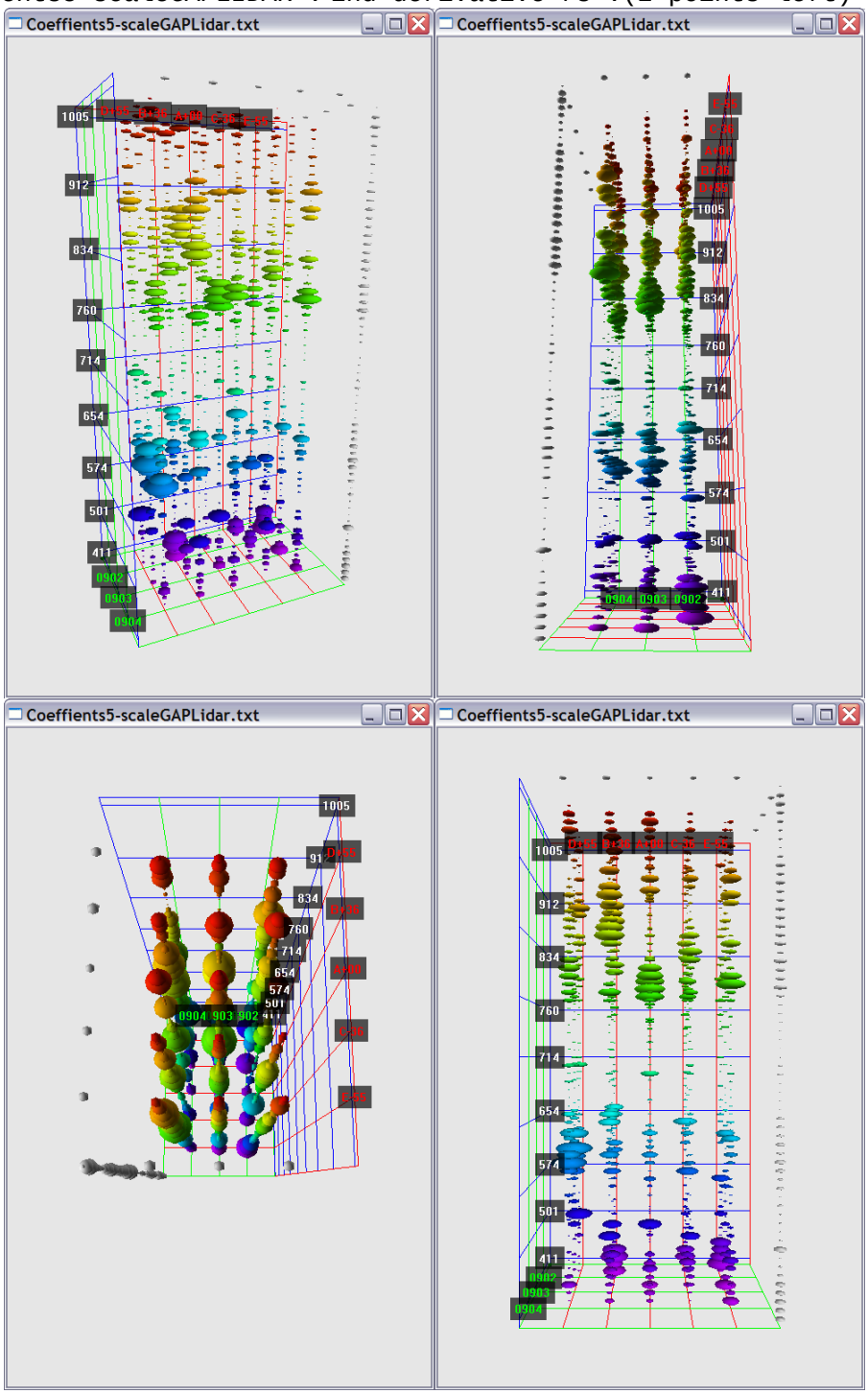

CoeffientsCHRISGAPLIDAR : 2nd derivative as :(2 points-middle)

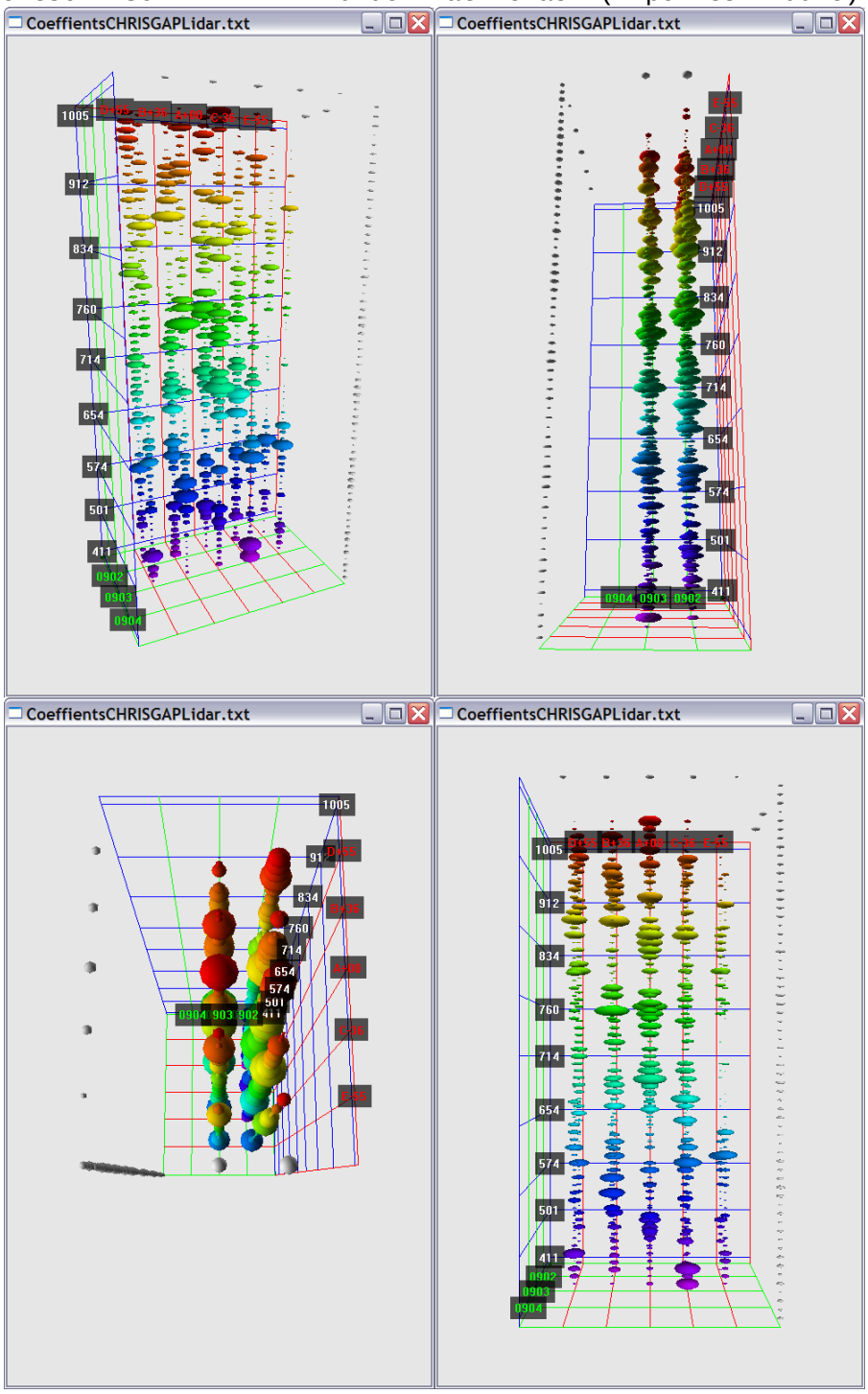

Coeffients5-scaleHeight.txt : 2nd derivative as :(2 points-middle)

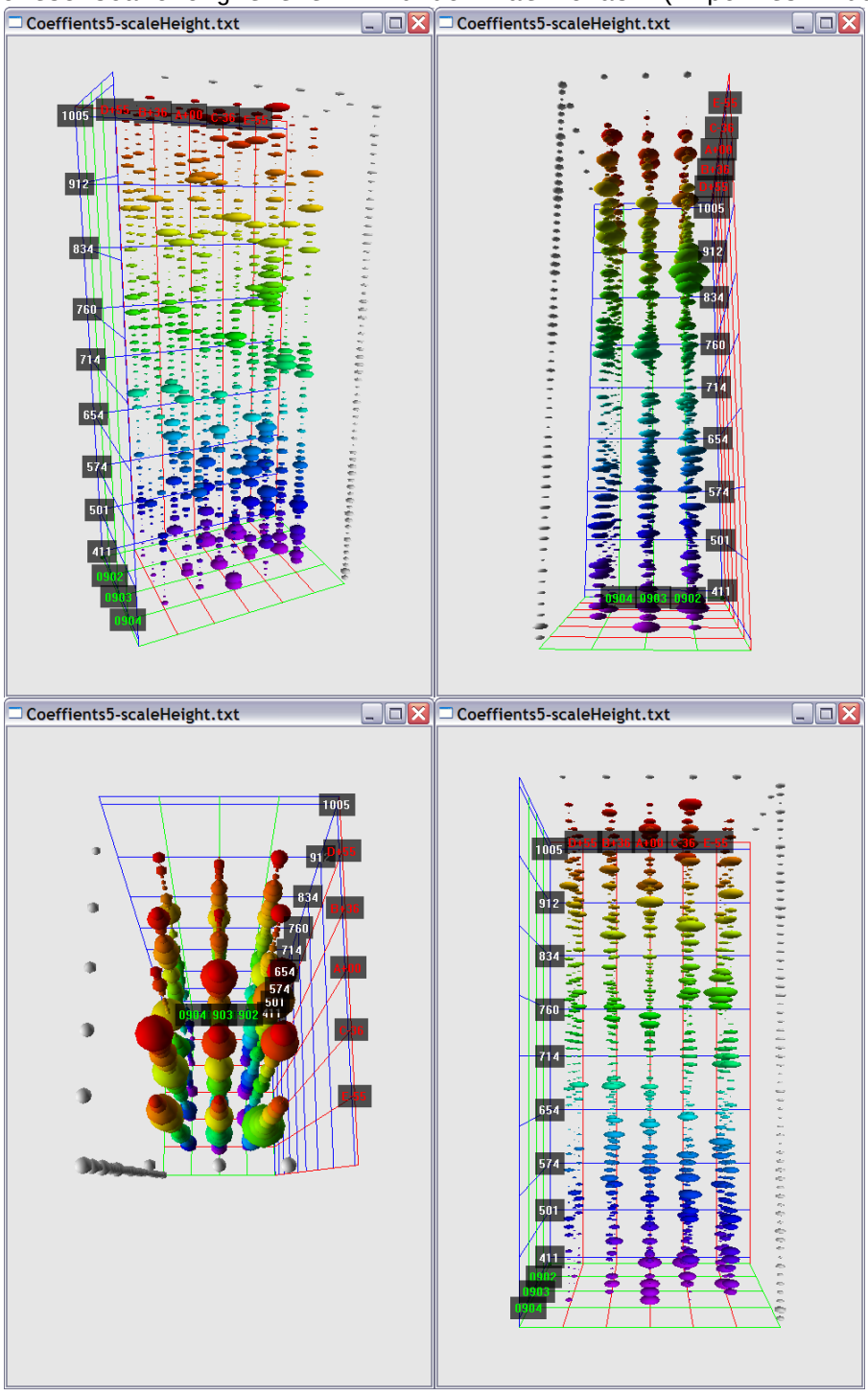

CoeffientsCHRISHeight : 2nd derivative rs :(2 points-middle)

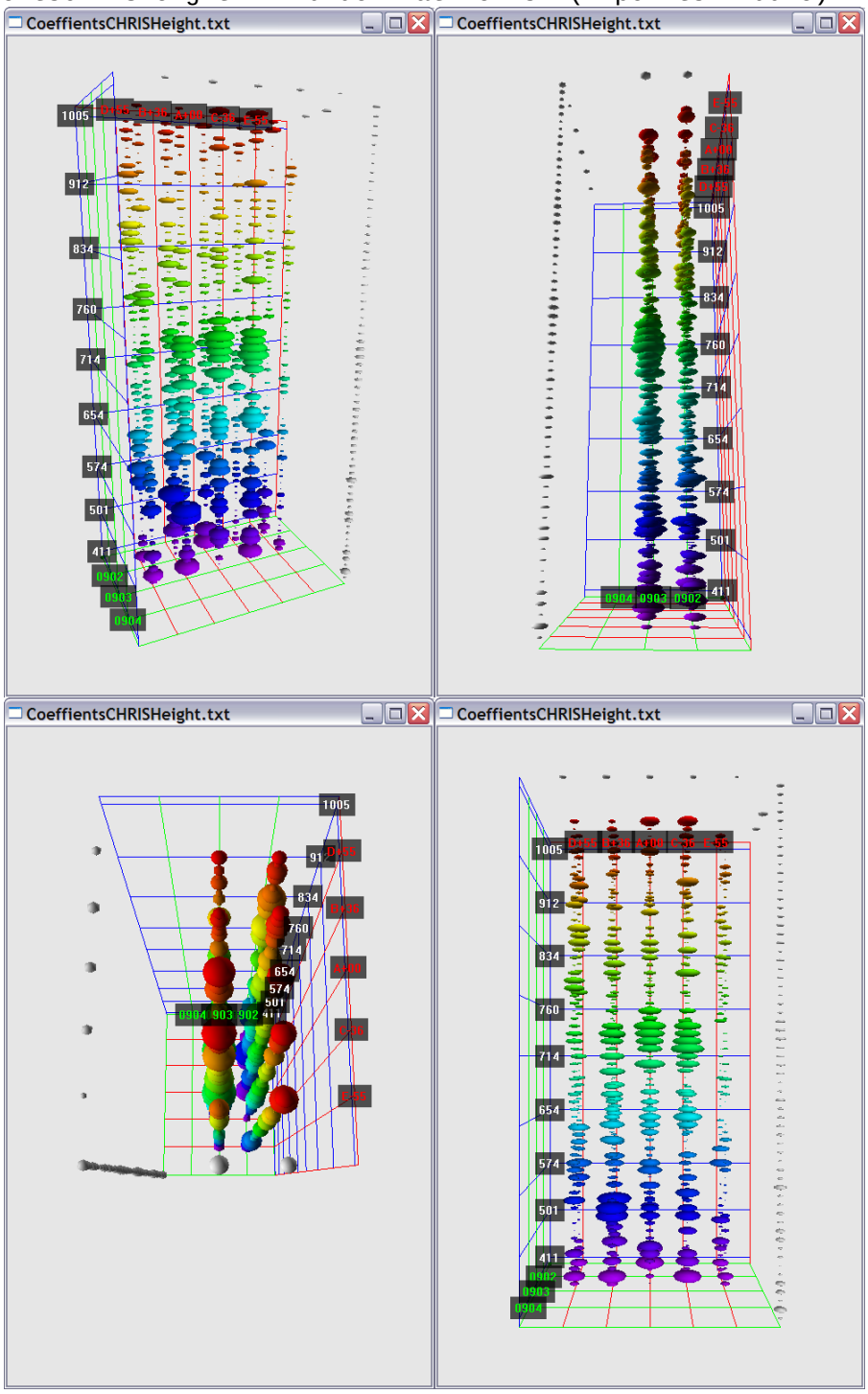

Coeffients5-scaleLAI : 1st derivative rs :(2 points-left)

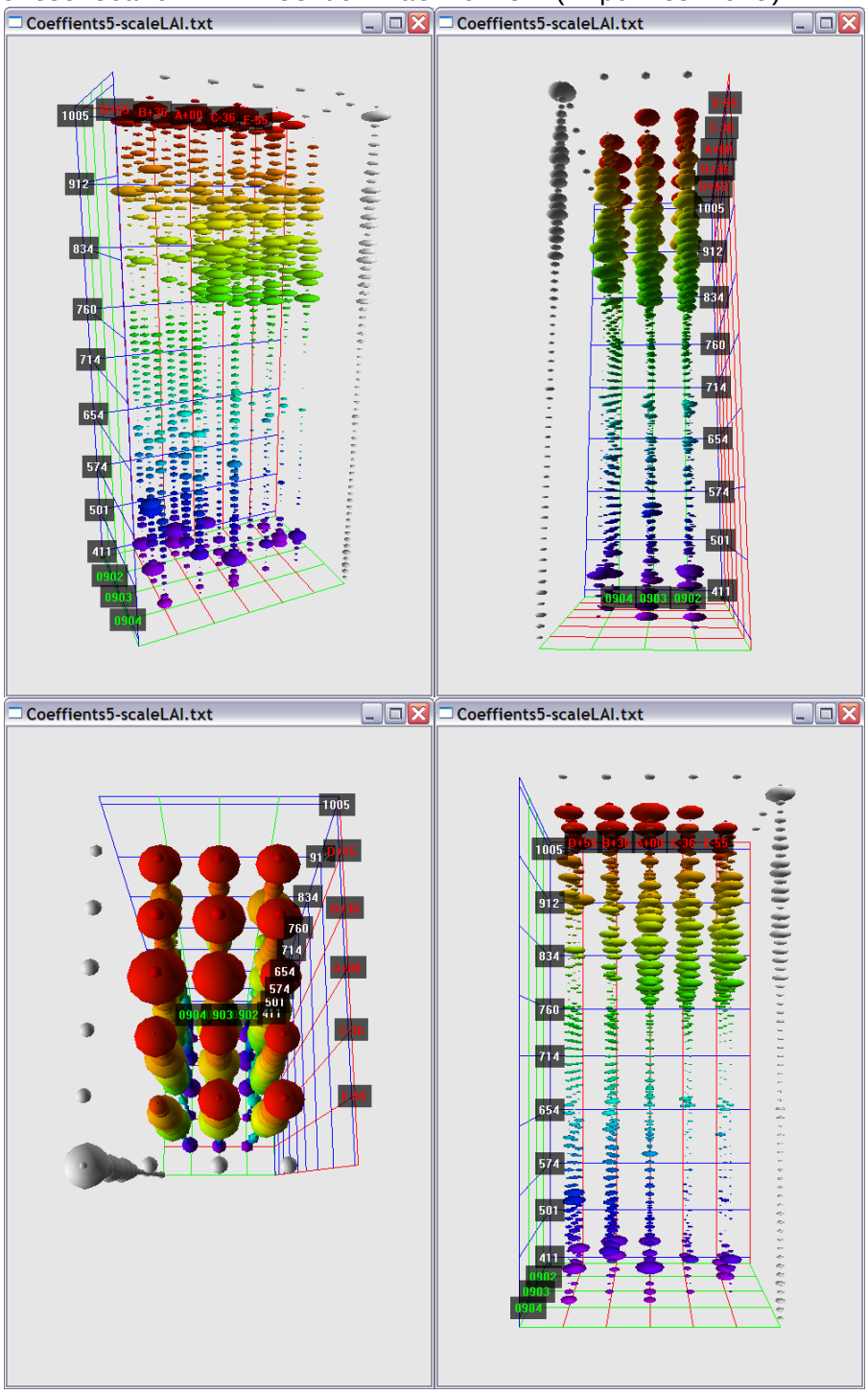

CoeffientsCHRISLAI.txt: 2nd derivative rs: (2 points-left)

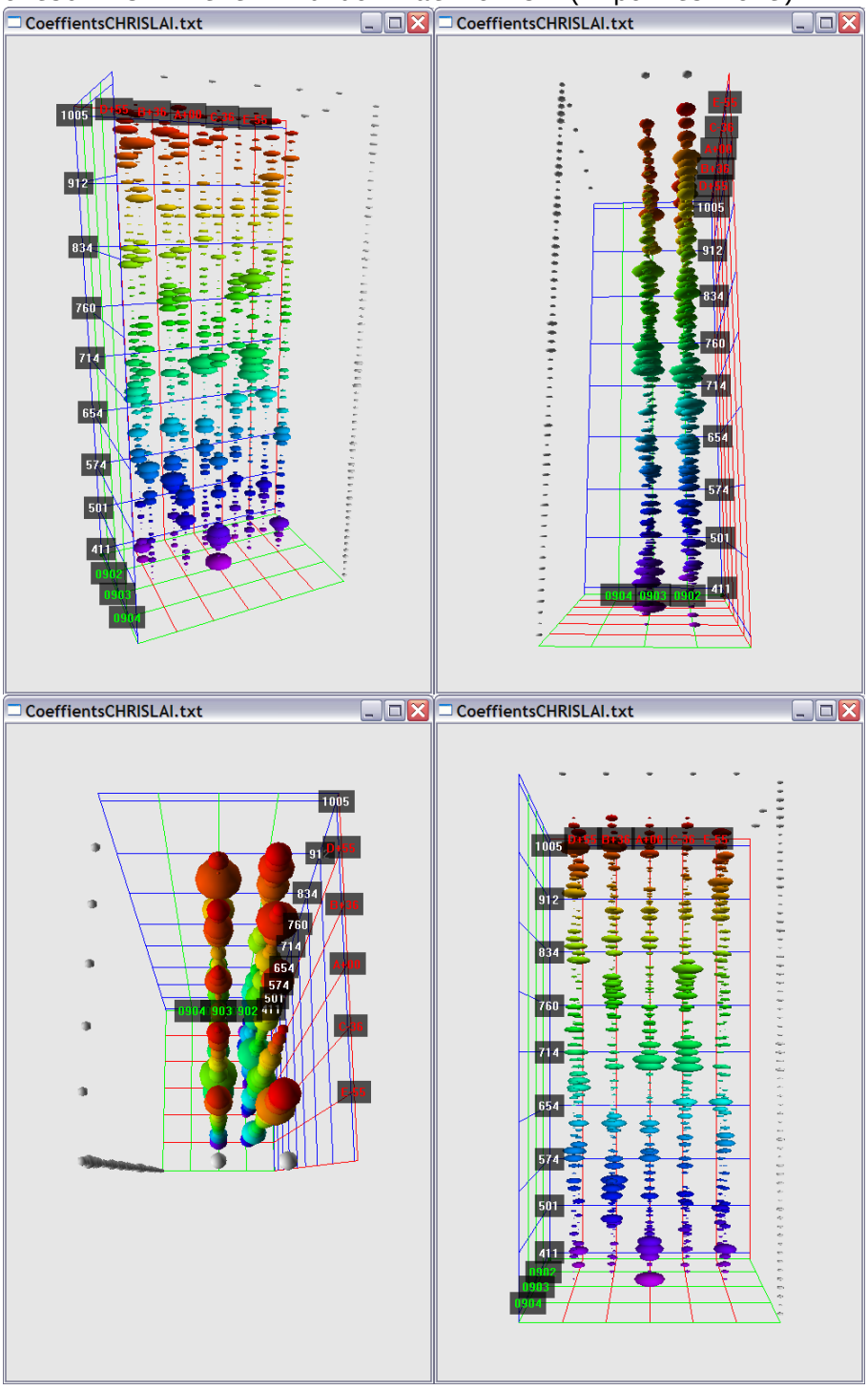

Coeffients5-scaleStemDensity : 2nd derivative rs :(2 points-left)

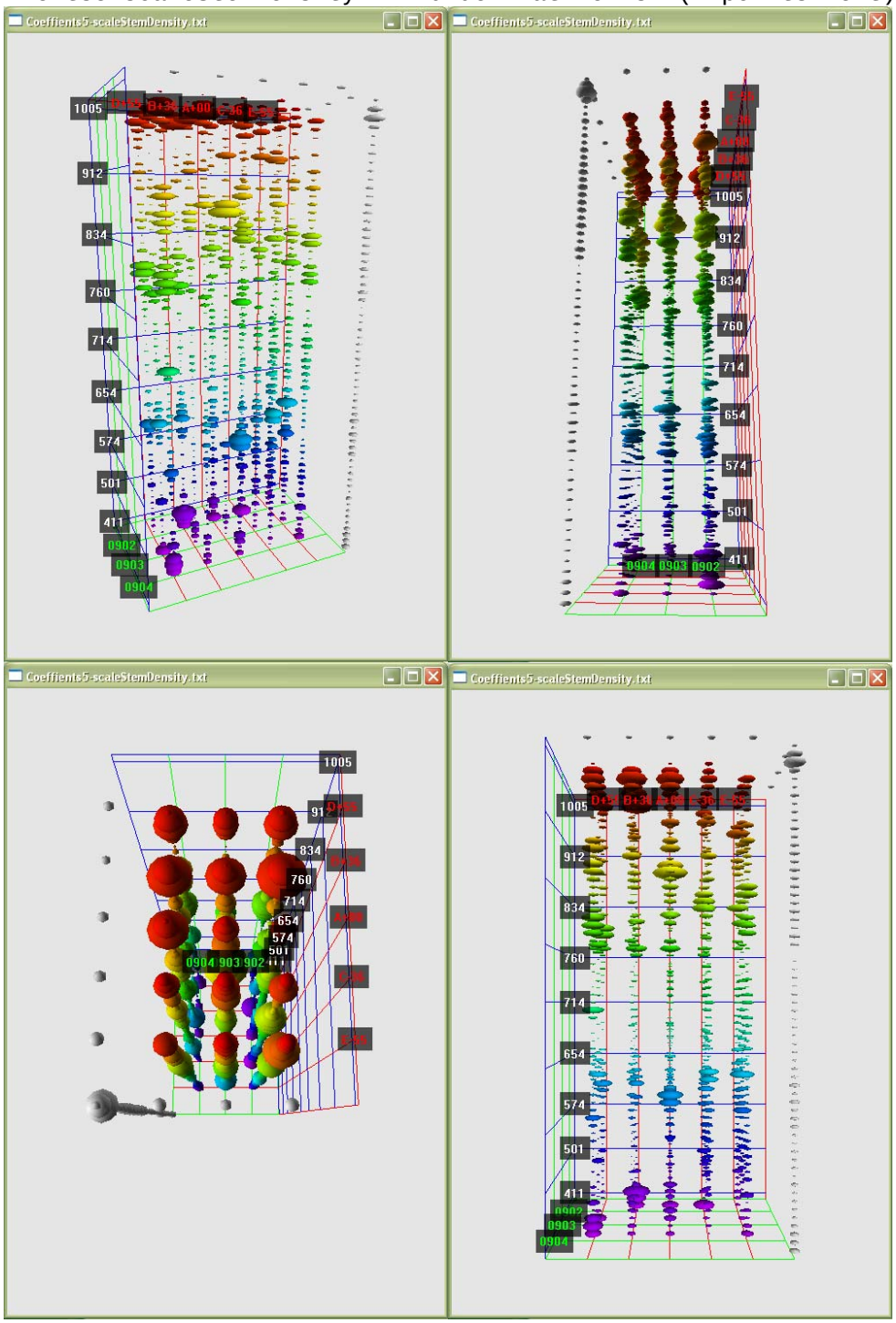

CoeffientsCHRISStemDensity: 2nd derivative rs:(3 points-quadratic fit)